XFEL.EU TR-2013-006

CONCEPTUAL DESIGN REPORT

Scientific Instrument Spectroscopy and Coherent Scattering (SCS)

November 2013

A. Scherz and O. Krupin

for the Scientific Instrument SCS (WP86) at European XFEL

with contributions from J. Buck, N. Gerasimova, G. Palmer, N. Poolton, and L. Samoylova

European X-Ray Free-Electron Laser Facility GmbH

Albert-Einstein-Ring 19

22761 Hamburg

Germany

Contents

List of Figures

List of Tables

1 Scope of the SCS instrument

This document reports on the present status of the conceptual design of the Spectroscopy and Coherent Scattering (SCS) scientific instrument at European XFEL. The SCS instrument is one of the six baseline instruments of the facility. It will cover a large range of scientific areas in the soft X-ray energy range of 0.25–3 keV, provide instrumentation that opens new scientific directions taking advantage of the unique European XFEL properties, and serve a broad scientific user community. As such, the SCS instrument aims to provide a diverse and complementary instrumental infrastructure with the baseline focus on solid-state systems.

This chapter gives an overview of the current conceptual design, external contributions, and interfaces to other work packages (WPs) at European XFEL as well as the scientific objectives and requirements.

1.1 Overview

This conceptual design report (CDR) for the SCS instrument has been developed over a six-month period with a very limited workforce. It describes the major SCS subsystems at different levels of detail. While the overall design of the SCS components is still conceptual, some parts, such as the X-ray refocusing system, are described in more detail because of their rather long lead times. Their technical design will have high priority during 2013, and the ordering will be initiated by the end of 2013. A technical design report (TDR) will be completed in spring 2014, including all SCS components, followed by the construction of the SCS end station, sample environment and detector interface in autumn 2014 which is estimated to take a year including performance tests. The construction of other subsystems and the overall installation phase is scheduled to begin in autumn 2015 and continue until the first beam is taken at the beginning of 2016.

The SCS instrument aims to provide a diverse platform for soft X-ray spectroscopy and coherent scattering techniques:

- Coherent X-ray diffraction imaging (CXDI)
- X-ray photon correlation spectroscopy (XPCS)
- Resonant elastic X-ray scattering (REXS)
- Resonant inelastic X-ray scattering (RIXS)
- Nonlinear X-ray spectroscopy (NLXS)
- Time- and angular-resolved photoelectron spectroscopy (tr-ARPES)

The goal is to set the stage for a class of experiments that have a major impact at the forefront of science, open new scientific directions, and stay highly competitive in the future when the SCS instrument becomes operational.

The main scientific objectives include:

- Understanding and controlling of complex materials
- Investigation of ultrafast magnetization processes on the nanoscale
- Real-time observation of chemical reactions at surfaces and in liquids
- Exploration of nonlinear X-ray spectroscopy techniques that are cornerstones at optical wavelengths

These objectives have been outlined in the TDR for the European XFEL [1].
More specific requirements have been reported by two working groups during an international workshop on the SCS instrument at Paul Scherrer Institute in Villigen, Switzerland [28; 54].

In terms of source properties, experimental geometries, and sample environment, these requirements are very different. They are discussed in Section 1.2, “Requirements”.

1.2 Requirements

1.2.1 Source

An overview of technique-based requirements is given in Table 1.1. The source requirements for the individual techniques are divided into coarse categories. (The source properties are discussed in detail in Chapter 2, "SASE3 photon beam properties").

Table 1.1: Overview of techniques and primary source requirements in the field of condensed-matter systems (fixed targets)

Technique	Photons per pulse	Peak intensity	Pulse duration	Repetition rate	Variable polarization
CXDI	High	High–medium	Short	Low[b]	Yes
XPCS	Medium	Medium	Variable	Medium–high	Optional
REXS	Medium[a]	Medium	Variable	High	Yes
RIXS	High[a]	Medium	Variable[b]	High	Yes
NLXS	High	High	Short, nearly transform limited	Medium–high	Yes
tr-ARPES	Low[a]	Low	Variable[b]	High	—

[a] Average photon flux requirement rather than photons per pulse.

[b] Fixed targets are considered here. The bottleneck is the positioning of samples between pulses.

We consider here fixed targets that cannot be easily replenished between X-ray pulses in contrast to liquid jets or particle injection schemes and, therefore, put additional constraints on the source parameters. The optimum number of photons per pulse depends on the experiment and samples. While, for CXDI, the number of incident photons ultimately determines the attainable image resolution and is in general maximized at the price of sample destruction in a singe shot [7; 42], the photon number per pulse is typically limited in order to avoid sample damage [53] or space charge effects (tr-ARPES) [19]. In particular, RIXS [2] and tr-ARPES will benefit from the high repetition rate of the source, and the key parameter is the average photon flux. The limitation of photons per pulse can be partially compensated and optimized by adjusting the X-ray beam size on the sample. This leads to the different peak intensity requirements for the various techniques. The

pulse duration further determines the peak intensities. Most of the techniques will require using the soft X-ray monochromator, which induces pulse stretching and caps the peak intensities. High peak intensities are important to drive nonlinear X-ray-matter interactions [33; 55; 37; 23], and NLXS will require short pulses. Here, the self-seeding soft X-ray scheme (see Section 2.3, “Soft X-ray self-seeding”) could provide a wavelength-controllable tool to generate femtosecond-short pulses near the transform limit. The self-seeding soft X-ray pulses are expected to have significant smaller bandwidth. Pump–probe spectroscopy experiments can potentially achieve higher temporal resolution by circumventing the monochromator. Finally, circular and linear polarization control of the source is one of the most important requirements for soft X-ray spectroscopy [48]. Essentially, all proposed techniques will take advantage of the proposed afterburner scheme that is described in Section 2.2, “Circular- and linear-polarization afterburner”.

1.2.2 Beam transport

The main optical components to deliver the X-ray beam to the sample are the soft X-ray monochromator, the X-ray beam split and delay (XBSD) line and the Kirkpatrick-Baez (KB) refocusing optics. Their requirements together with experimental geometry and detectors are listed in Table 1.2 on the next page. The technical design of the monochromator provides a high-resolution ($E/\Delta E \simeq 40\,000$), a medium-resolution ($E/\Delta E \simeq 10\,000$) and a pink-beam operation mode [45]. The time-resolved experiments that require the use of the monochromator will need to find a compromise between energy resolution and temporal resolution. Potential schemes to optimize these two parameters are discussed in Section 3.4, “Soft X-ray monochromator”.

The XBSD device allows for carrying out X-ray pump–probe experiments. The requirements for XPCS and NLXS are different in terms of bandwidth requirements, pulse lengths and intensities of the pump and probe beam. In case of XPCS, the device should provide equal pulse intensities in order to study order parameter fluctuations on ultrashort time scales in the sample, while longer timescales (> 220 ns) are accessible thanks to the high repetition rate of the source. In the case of NLXS, different intensities and bandwidths of the split pulses are potentially required for ultrafast nonlinear X-ray spectroscopy developments [35] as, for example, coherent X-ray Raman spectroscopy [50]. A conceptional design of the XBSD device that supports both experimental requirements is given in Section 3.6, “X-ray beam split and delay line”. The XBSD device may optionally serve sequential single-shot imaging [18] or two-colour X-ray pump–probe studies using the first and higher harmonics of the source.

Table 1.2: Overview of required beam transport components for the proposed techniques

Technique	Monochromator resolution	XBSD	Refocusing at sample	Scattering geometry	Detector
CXDI	Pink–medium	Optional	Tight–medium	Forward/ backward	2D array detector
XPCS	Pink–medium	Yes	Medium–tight	Forward/ backward	2D array detector
REXS	Medium	—	Medium	Backward	2D array detector
RIXS	Best–high	—	Large (horzontal), tight (vertical)	Backward	Spectrometer
NLXS	Medium–high (X-ray probe)	Yes	Tight	Forward	Spectrometer
tr-ARPES[a]	High	Optional	Large–medium	Photon-in/ electron-out	ARTOF

[a] Dedicated tr-ARPES experiment chamber

As discussed above, the proposed experiments have different requirements in terms of photon numbers and intensities per pulse. The KB refocusing optics will need to provide variable beam sizes at the sample position in order to make the best use of the high average photon flux without beam attenuation. In general, the beam size requirements range from 1 to 10 µm (tight focus) with nearly structureless wavefront properties for CXDI and NLXS. For time-resolved, pulse-averaged studies [17; 22], a beam size of 100 to 1000 µm (medium–large focus) is needed. The conceptual design of the KB mirrors with bent mechanism is described in Section 3.5, "KB refocusing optics". Finally, the different experimental geometries will require specific infrastructure and setups (see Chapter 5, "SCS hutch infrastructure and experiment setups"), as well as different detectors (see Chapter 6, "Detectors"), which are summarized in Table 1.2.

Table 1.3 on the next page summarizes the relevant controls for the sample environment. Temperature control over a range of 4–2000 K and magnetic fields up to several tens of Tesla poses particular challenges for the instrumentation and sample environment constraints in terms of sample manipulation and space

around the sample interaction point. Including the optical laser delivery and vacuum requirements, a flexible and modular sample environment is needed in order to find the optimum solution for the user experiment. For the optical laser pump, frequency up- and down-conversion schemes of the central optical laser system are required. An overview is given in Chapter 8, “Optical laser delivery”. Factors like radiation damage and sample degradation or destructive X-ray probe will require a fast sample exchange to minimize interruptions of the experiment. The details of the sample environment are discussed in Section 5.6, “Sample environment and delivery”.

Table 1.3: Overview of sample environment requirements related to the techniques

Technique	Temperature control	Magnetic fields	Optical laser	Nondestructive probe	Fast sample exchange
CXDI	Optional	Optional	Yes	—	Yes
XPCS	Yes	Optional	Optional	Yes	Yes
REXS	Yes	Optional	Yes	Yes	Yes
RIXS	Yes	Optional	Yes	Yes	Yes
NLXS	Yes	—	Optional	—	Yes
tr-ARPES	Yes	Optional	Yes	Yes	Yes

1.3 Interfaces to other work packages

The SCS instrument has several interfaces to and collaborations with WPs at European XFEL that significantly contribute to the technical realization, as listed in Table 1.4.

Table 1.4: Interfaces to other European XFEL work packages. (*Key:* SPB = Single Particles, Clusters, and Biomolecules, SQS = Small Quantum Systems, XGMD = X-ray gas monitor detector, XBPM = X-ray beam position monitor, PES = photoelectron spectroscopy, DSSC = Depleted P-Channel Field Effect Transistor (DEPFET) Sensor with Signal Compression, CCD = charge-coupled device, DAQ = data acquisition.)

Work package	Interface / collaboration	Component
73 – X-Ray Optics and Beam Transport	Interface	Soft X-ray monochromator, beam transport tunnel
73 – X-Ray Optics and Beam Transport	Collaboration	XBSD, KB (SCS responsibility)
74 – X-Ray Photon Diagnostics	Interface	XGMD, XBPM, PES
74 – X-Ray Photon Diagnostics	Collaboration	Timing diagnostics
79 – Sample Environment	Interface / collaboration	Cryogenic cooling, magnetic fields, load lock transfer
75 – Detector Development	Interface	DSSC, FastCCD detectors
76 – DAQ & Control Systems	interface	DAQ, controls
84 – Scientific Instrument SPB 85 – Scientific Instrument SQS 75 – Detector Development	Collaboration	Integration of detectors
72 – Simulation of Photon Fields	Collaboration	Development of accelerator-based techniques for nonlinear X-ray science

1.4 External contribution and user consortia

The broad scientific scope of the SCS instrument cannot be achieved without important contributions from the user community. At present, two large user consortia (UC) expressed their interest in providing key instrumentation to the SCS instruments.

The Heisenberg RIXS user consortium (hRIXS@xfel.eu, spokesperson: A. Föhlisch, Helmholtz-Zentrum Berlin / University of Potsdam, Germany) proposal has been approved by the European XFEL Scientific Advisory Committee (SAC) and Council. The project aims at the creation of a facility for time-, energy-, and momentum-resolved RIXS at the Heisenberg limit. The project's instrumental contribution encompasses a high-resolution RIXS spectrometer, a RIXS end station for solid targets and liquid-jet environments, and a high-resolution upgrade to the soft X-ray monochromator. The spectrometer will be integrated in the SCS experiment hutch.

The Photoelectron Spectroscopy UC (pes@xfel.eu, spokesperson: U. Karlsson, KTH Royal Institute of Technology, Sweden) is being reviewed for approval by the European XFEL SAC and Council in the second half of 2013. The project aims at establishing femtosecond time-resolved PES in the soft and hard X-ray energy range for studying bulk, surface, and in-flight nanoparticle electronic and magnetic dynamics. At present, instrumental contributions are a highly efficient ARTOF spectrometer that is compatible with the European XFEL repetition rate [34] and a PES end station. The location of the instrumentation is currently being discussed with the SCS group.

2 SASE3 photon beam properties

This chapter briefly describes the source properties of the SASE3 undulator for the soft X-ray beamlines at the European XFEL. The most relevant source properties are provided in parameterized form in order to determine boundary conditions for the X-ray optical layout of the SCS branch and to simulate the performance for the spectroscopy and coherent scattering techniques. These empirical source parameters have been used throughout the SCS conceptual design. Upgrades to SASE3 encompass an electromagnet-based afterburner and a soft X-ray self-seeding scheme [10]. The concept of the afterburner, which provides tunable circular and linear polarization, is described and, finally, an outline of the proposed soft X-ray self-seeding scheme is given.

2.1 SASE3

A comprehensive description of the beam properties at the European XFEL has been provided by Schneidmiller and Yurkov [41]. The most important source properties are more conveniently described by an empirical parameterization of the calculations in Ref. [41] for the SCS instrumentation simulations. Such a parameterization has been performed for the hard X-ray SASE1 and SASE2 sources in Ref. [46]. The SASE3 parameterization in this CDR follows the same steps.

2.1.1 SASE3 source parameterization

The source properties size, divergence, radiation pulse energy, and spectral bandwidth depend on the wavelength λ, the bunch charge c, and the electron energy (10.5, 14, and 17.5 GeV). The bunch charge and the radiation pulse duration have a linear relationship, as shown in Figure 2.1 on the next page.

The source size, pulse energy, and bandwidth (full width at half maximum, FWHM) are empirically given by

$$\begin{aligned} S_{\mathrm{FWHM}} &= s_1 \cdot \ln(s_2 \cdot \lambda[\mathrm{nm}]) \\ E_{\mathrm{pulse}} &= e_1 \cdot \ln(e_2 \cdot \lambda[\mathrm{nm}]) \\ (\Delta\omega/\omega)_{\mathrm{FWHM}} &= w_1 \cdot \ln(w_2 \cdot \lambda[\mathrm{nm}]) \end{aligned} \tag{2.1}$$

where the dependence of the coefficients on the bunch charge is modeled according to

$$\begin{aligned} s_1 &= s_{10} + s_{11} \cdot c[\text{nC}] \quad \text{and} \quad s_2 = s_{20} \cdot \exp(-s_{21} \cdot c[\text{nC}]) \\ e_1 &= e_{10} + e_{11} \cdot c[\text{nC}] \quad \text{and} \quad e_2 = e_{20} \cdot \exp(-e_{21} \cdot c[\text{nC}]) \\ w_1 &= w_{10} \approx \text{const.} \quad \text{and} \quad w_2 = w_{20} \cdot \exp(-w_{21} \cdot c[\text{nC}]) \end{aligned} \tag{2.2}$$

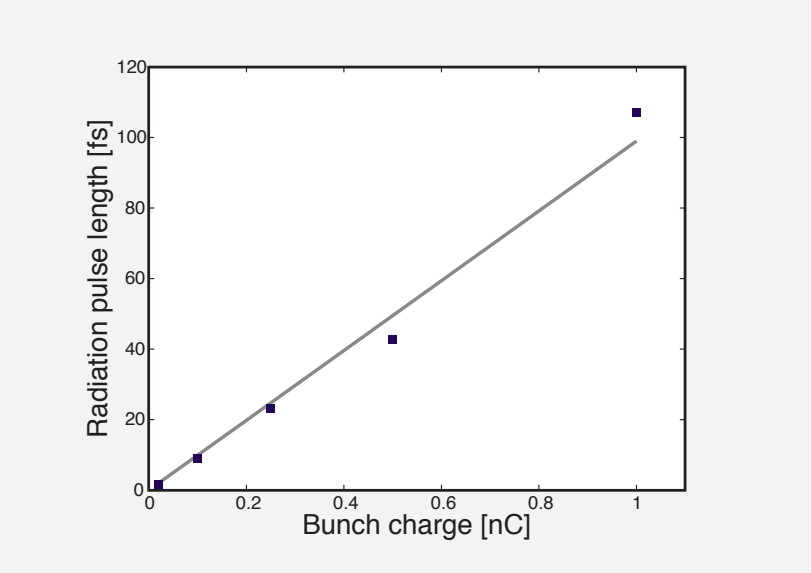

Figure 2.1: Radiation pulse length (FWHM) grows proportional to the bunch charge in the SASE saturation. The data points are calculations from [41].

The source divergence (FWHM) is fitted using

$$\delta\theta = \theta_0 + \theta_1 \cdot \lambda^{2/3} \tag{2.3}$$

where the dependence of the coefficients on the bunch charge is modeled according to

$$\theta_0 = \theta_{00} \approx \text{const.} \quad \text{and} \quad \theta_1 = \theta_{10} - \theta_{11} \cdot (c[\text{nC}])^{1/3} \tag{2.4}$$

The results are shown in Figure 2.2 on the facing page and Figure 2.3 on page 24 for 14 GeV electron energies. The coefficients for the different electron energies are listed in Appendix A, “SASE3 source parameterization”.

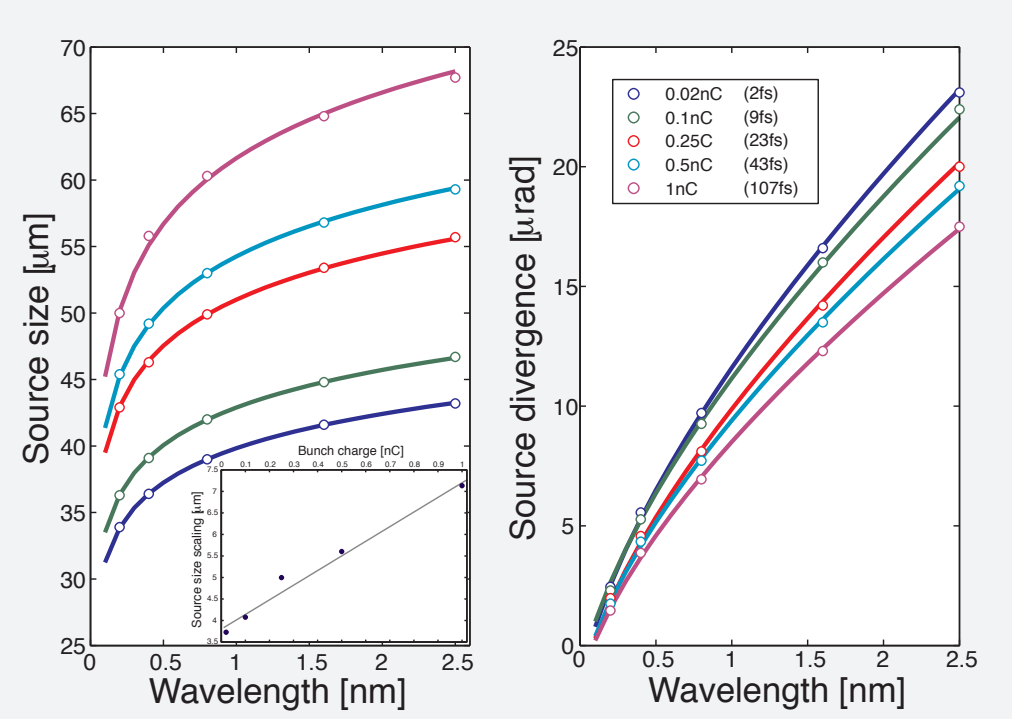

Figure 2.2: SASE3 baseline for 14 GeV electron energy: (left) source size and (right) angular divergence as a function of wavelength and bunch charge in the SASE saturation. The inset on the left shows the source size scaling with the bunch charge. The data points are calculations from [41], and the curves result from parameterization in terms of wavelength and bunch charge.

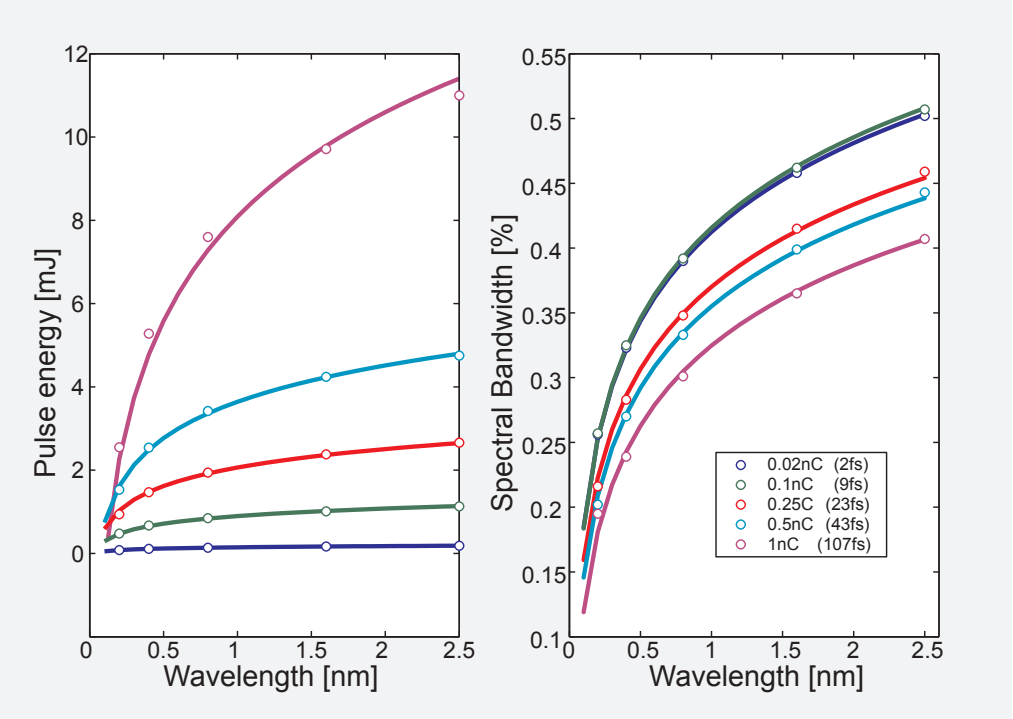

Figure 2.3: SASE3 baseline for 14 GeV electron energy: (left) pulse energy and (right) spectral bandwidth as a function of wavelength and bunch charge in the SASE saturation. The data points are calculations from [41], and the curves result from parameterization in terms of wavelength and bunch charge.

2.1.2 Source considerations for X-ray optics

The source divergence is the most important parameter for the layout of the beam transport system and, in particular, the optical length of mirrors. The source divergence is largest for the smallest photon energies and the shortest pulses (Figure 2.2 on the preceding page). Accordingly, the components of Chapter 3, "X-ray optical layout", have been optimized as much as possible to avoid mirror cutoffs at the lower end of the photon energies. The pulse energy increases with bunch charge (or longer pulse durations) and decreases with photon energy. This dependence puts constraints on the useful range of incident angles for the beamline mirrors at the lowest photon energies because of potential radiation damage issues. The impact of source parameters on the beam transport design has been reviewed in detail by the X-Ray Optics and Beam Transport group (WP73) and can be found in the group's CDR and TDR [46; 45], respectively.

2.1.3 Electron energy operation modes

Electron energies of 10.5, 14, and 17.5 GeV have been assumed for the calculation of the baseline European XFEL operation. The lowest photon energies achievable in SASE3 are then ~ 250, 500 and 800 eV, respectively. Figure 2.4 and Figure 2.5 on the following page show the expected SASE3 brilliance, peak power, photons per pulse, and photon flux for the different operation modes and pulse durations. The different electron energies have, in general, a rather small influence on the SASE3 performance, and optimum operation parameters will depend on the type of experiment. The SASE3 self-seeding upgrade is currently investigated for the 10.5 GeV mode. Operating at higher than 10.5 GeV electron energies is feasible but ultimately limited by the magnetic fields in the electron chicane (see Section 2.3, "Soft X-ray self-seeding").

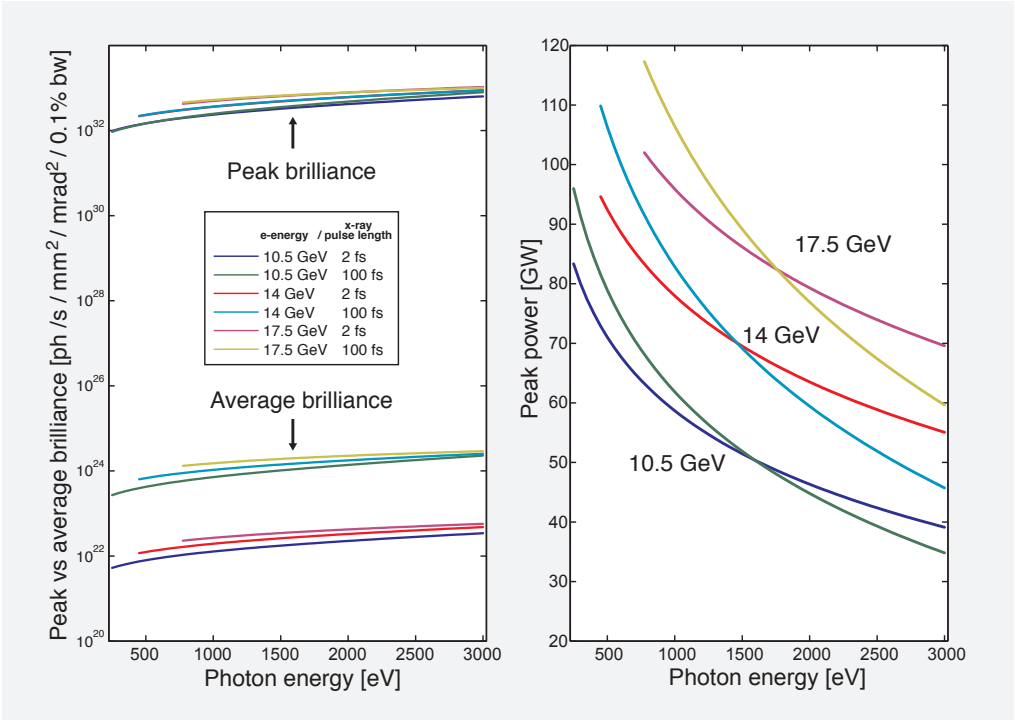

Figure 2.4: SASE3 characteristics: (left) peak and average brilliance and (right) peak power as a function of photon energy for baseline electron energies and X-ray pulse duration or bunch charge, respectively.

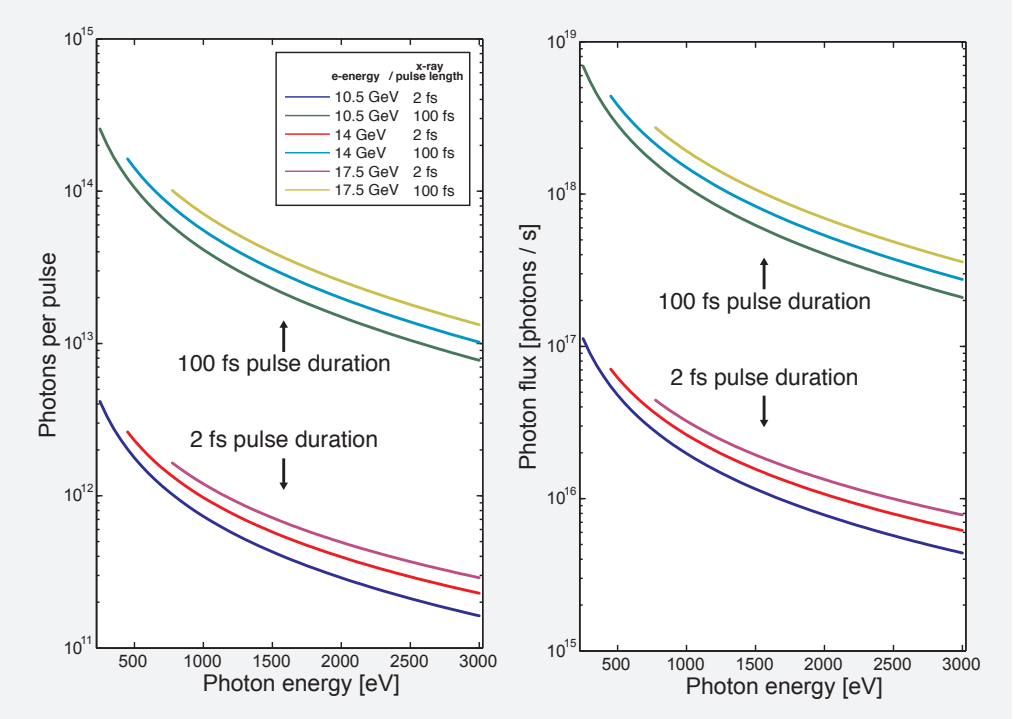

Figure 2.5: SASE3 characteristics: (left) number of photons per pulse and (right) photon flux as a function of photon energy for baseline electron energies and X-ray pulse duration or bunch charge, respectively.

2.2 Circular- and linear-polarization afterburner

An afterburner upgrade of the SASE3 source is based on a user consortium proposal by the Budker Institute of Nuclear Physics (BINP) in Novosibirsk, Russia. The proposed afterburner is a set of electromagnetic undulators that will be installed downstream of the SASE3 undulators (see Figure 2.6). The afterburner generates coherent radiation of variable linear and circular polarization from the SASE3 microbunched electron beams and is capable of running in the European XFEL burst mode. Using electromagnetic undulators, the polarization can be switched between consecutive pulse trains (10 Hz), as illustrated in (c) in Figure 2.6. A full polarization control at SASE3, which is a standard tool at synchrotron facilities, will enable important spectroscopy studies of electronic and magnetic structures and their excitations.

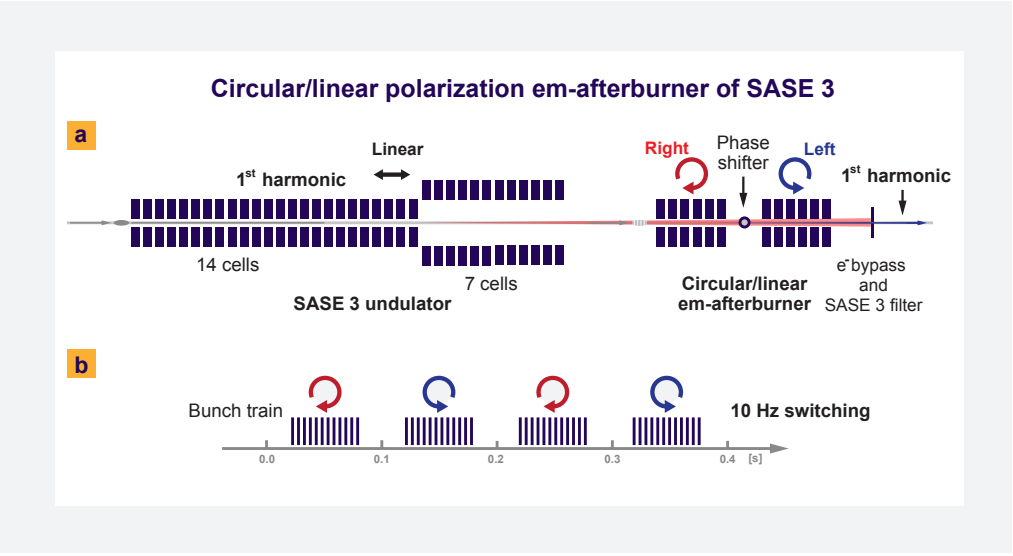

Figure 2.6: Concept of generating circular polarization at SASE3 using an afterburner: Two-thirds of the SASE3 undulator is used to generate the electron microbunching for the afterburner without going into saturation. One-third of the undulators is used as a drift section (open gap) for the microbunches before they enter the short afterburner. SASE3 radiation is spatially removed from the afterburner radiation by slits (b) fast switching mode of circular or linear polarization.

The afterburner source parameters are similar to SASE3. The feasibility studies include the scheme of separating the afterburner and SASE3 coherent radiation [15]. This scheme is shown in Figure 2.6: Two-thirds of the SASE3 undulator is used to generate the electron microbunching for the afterburner without going into saturation. One-third of the undulators is used as a drift section (open gap) for the

microbunches before they enter the short afterburner. An aperture of 0.1 mm in diameter behind the afterburner is used to suppress the SASE3 radiation from the circular afterburner radiation, because the beam size of the SASE3 background is, after 47 m of propagation distance, 30 times larger than the one of the afterburner at the aperture location. Therefore, the radiation behind the aperture contains more than 99% afterburner radiation. Note that, in addition, the afterburner radiation is 10 times more intense than the non-saturated SASE3 radiation, which makes this spatial filtering method even more effective. Finally, a magnetic chicane lets the electron beam bypass the aperture.

2.3 Soft X-ray self-seeding

The longitudinal coherence of self-amplified spontaneous emission (SASE) radiation can be enhanced in self-seeding schemes producing free-electron laser (FEL) radiation of much narrower bandwidth and nearly transform-limited pulses. The advantage of self-seeding schemes over the use of beamline monochromators (intensity loss) is the expected increase in X-ray intensities compared to SASE, see [16] and references therein. At soft X-ray energies, the scheme is based on a variable line spacing (VLS) grating monochromator [43] that is installed between the SASE3 undulators segments, as illustrated in Figure 2.7.

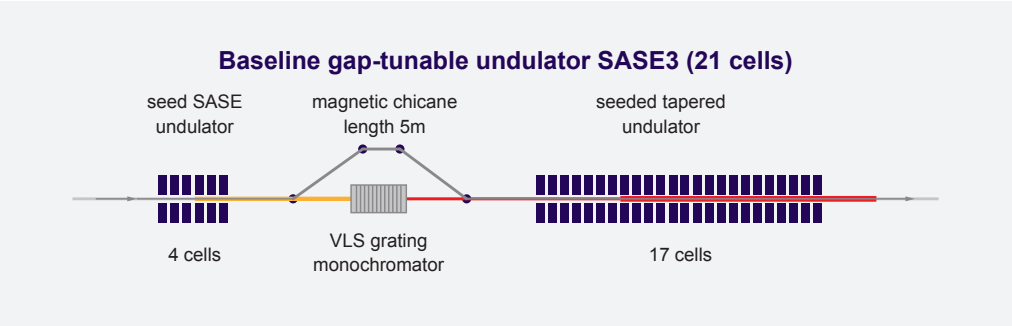

Figure 2.7: Proposed self-seeding scheme for the European XFEL baseline SASE3 undulator for generating nearly transform-limited soft X-ray pulses. The design exploits a VLS-based monochromator [43] combined with an undulator tapering technique. The scheme is currently investigated for 10.5 GeV electron energies to produce X-ray pulses in the range of 250–1000 eV at TW power level. Operating at higher than 10.5 GeV electron energies is feasible but ultimately limited by the magnetic fields in the electron chicane. The figure is taken from [16].

A case study of the soft X-ray self-seeding performance at the European XFEL showed that 10 fs pulses of ~ 700 meV bandwidth (1200 resolving power) can be

produced at 1.5 nm wavelength (826 eV) [16]. In addition, by exploiting tapering in the gap-tunable SASE3 undulators, more soft X-ray FEL power can be extracted, i.e. an eightfold increase compared to the SASE3 saturation level was simulated.

The soft X-ray self-seeding is fully compatible with the circular- and linear-polarization afterburner. The SASE3 and SCS beam transport system considers this upgrade as an integral component in the operations. Employing soft X-ray self-seeding at the SCS instrument is discussed in Section 3.4, “Soft X-ray monochromator”, and Section 3.6, “X-ray beam split and delay line”.

3 X-ray optical layout

This chapter describes the main components of the SCS-related beamline optics. The X-ray optical components that are located in the SASE3 tunnel have been conceptually and technically designed by the X-Ray Optics and Beam Transport group (WP73). The details can be found in [45] and will be briefly reviewed in this CDR. In particular, the specifications of the the soft X-ray monochromator will be discussed. The KB refocusing optics and the X-ray beam split and delay (XBSD) line, which are the responsibility of the SCS group, are then described in more detail.

3.1 Component overview

In Figure 3.1 on the next page, the schematic layout of the SASE3 photon beam transport system is shown as presented in Ref. [45]. The first upstream element is a combination of horizontal offset (M1) and adaptive (M2) mirrors for removing spontaneous radiation and providing the option of an intermediate horizontal focus to limit the horizontal beam size in the experiment hutch (Figure 3.3 on page 34). The second element is the soft X-ray monochromator consisting of the pre-mirrors M3a and M3b, which focus the zeroth order of the grating (G1, G2, and M4) onto the vertical exit slit. The dispersing element is a variable line spacing (VLS) grating. The VLS parameter is chosen such that the first order of the grating is also focused onto the vertical exit slit. The exit slit is placed 99 m away from the gratings in order to reduce the demagnification factor of the source point and to mitigate damage. The horizontal distribution mirrors M5 and M6 transport the beam to the SCS and the currently open branch of the SASE3 experiment area, respectively.

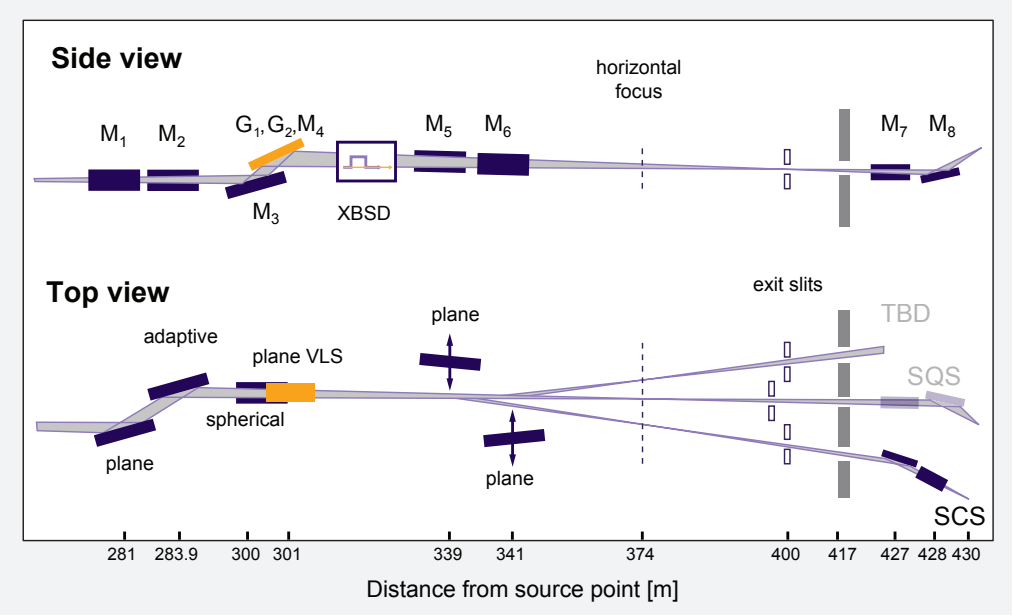

Figure 3.1: Schematic layout of the X-ray optical beam transport system from SASE3 to SCS, SQS, and the open port (adapted from the X-Ray Optics and Beam Transport TDR [45])

The proposed XBSD would be located between the gratings and the distribution mirrors and has been added to the technical layout of the tunnel beam transport. This device would therefore serve all three branches, i.e. SQS, SCS, and the open port. Finally, the beam is delivered to the SCS hutch where the KB bent refocusing optics provide variable beam sizes at the sample interaction point. The distances of the X-ray optics to the SASE3 source point are listed in Table 3.1 on the next page.

Table 3.1: X-ray optical layout of the SASE3/SCS beamline and source distances of the optical elements

Optical element	Type	Plane	Distance [m]
SRC	Source	–	0.0
M1	Offset	Hor	281.0
M2	Adaptive	Hor	283.9
ENT	Entrance slit	Ver	298.5
M3a,b	Mono pre-mirrors	Ver	299.4, 300.4
G1	VLS 50 l/mm	Ver	301.0
G2	VLS 150 l/mm	Ver	301.0
M4	Flat mirror	Ver	301.0
XBSD	Split & delay	Hor/ver	305–325
M5	Distribution	Hor	339.0
IFH	Intermediate focus	Hor	374.0
EX	Exit slit	Ver	400.0
M7	Elliptical KB	Hor	426.5
M8	Elliptical KB	Ver	427.8
SAM	Sample	—	429.8

3.2 Offset mirrors and higher-harmonic suppression

The baseline coating for all reflecting mirrors is boron carbide (B_4C), which currently shows the best properties based on damage experiments. Figure 3.2 on the facing page shows the transmission of the offset mirrors M1 and M2 as a function of mirror incident angles. For incident angles of $\theta \leq 9$ mrad, an overall high transmission is achieved over the baseline photon energy range of 0.25–3 keV except for the carbon K edge resonance. Note that optical constants from the webpage of the Center for X-Ray Optics (CXRO) at Lawrence Berkeley National Laboratory in Berkeley, California, have been used for the calculation in Figure 3.2 on the next page, and that the resonant enhancement at the K edge is missing. The transmission is expected to sharply drop at ~ 280 eV. A study of the B_4C optical constants is under way in the X-Ray Optics and Beam Transport group in order to quantify the intensity drop in the vicinity of the carbon K edge. Since the overall layout of the beam transport is

optimized for photon energies up to 3 keV, the offset mirrors can be used to suppress the SASE3 third harmonic by going up to $\theta = 20$ mrad when operating at lower photon energies, as shown in Figure 3.2.

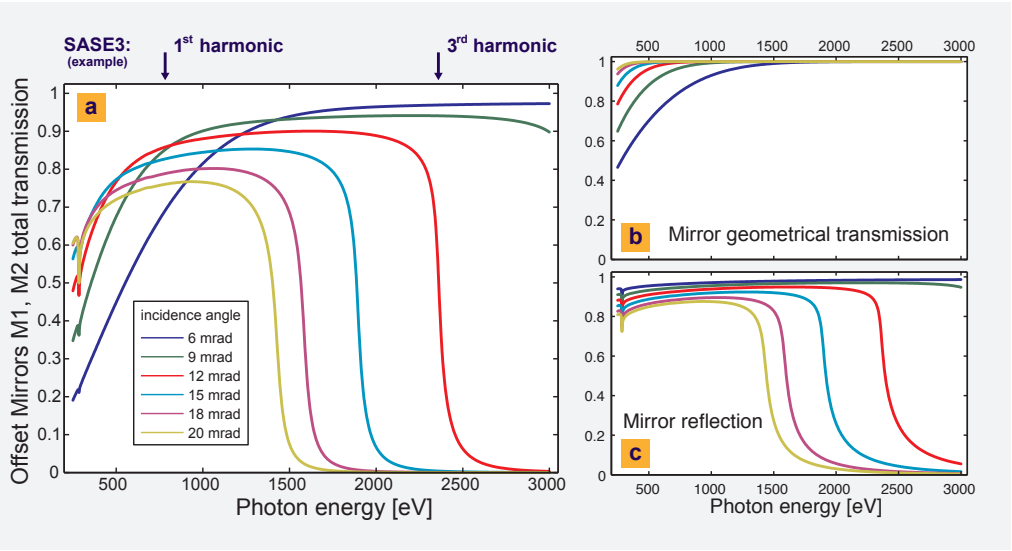

Figure 3.2: Principle of higher-harmonic suppression using the M1 and M2 offset mirrors: (a) M1 × M2 total transmission as a function of photon energy and X-ray incident angle (6–20 mrad). The total transmission is given by the geometrical transmission and the reflectivity. (b) Mirror geometrical cutoff given by the mirror aperture. (c) Mirror reflectivity for the same set of X-ray incident angles. Mirror parameters for this calculation: 800 mm optical length and B_4C coating (50 nm). SASE3 parameter: 14 GeV and 0.25 nC.

3.3 Beam size versus mirror apertures

The 4σ beam size in the horizontal and vertical direction is shown as a function of photon energies along the SCS branch in Figure 3.3 on the next page. Since the beam divergence changes with the bunch charge, data for 2 fs and 100 fs pulse durations are included for comparison. High transmission with insignificant beam cutoffs by the mirror apertures can be achieved. At higher photon energies (> 1.5 keV), the overall beam size is smaller and the mirrors' incident angles are below < 11 mrad. At lower photon energies, the overall beam size is larger and the incident angle is adjusted up to 20 mrad in order to reduce mirror cutoffs. The pre-mirror M3 as well as the gratings G1, G2, and M4 have a limited optical length that leads to some beam intensity loss below 500 eV. The respective offsets in the beam path are omitted in Figure 3.3 on the following page and can be found in the X-Ray Optics and Beam Transport TDR [45]. The change in the optical axis when switching between

SASE3 and intermediate source points ranges between 10–30 mm in the SCS experiment hutch and will be considered in the TDR of the SCS beamline.

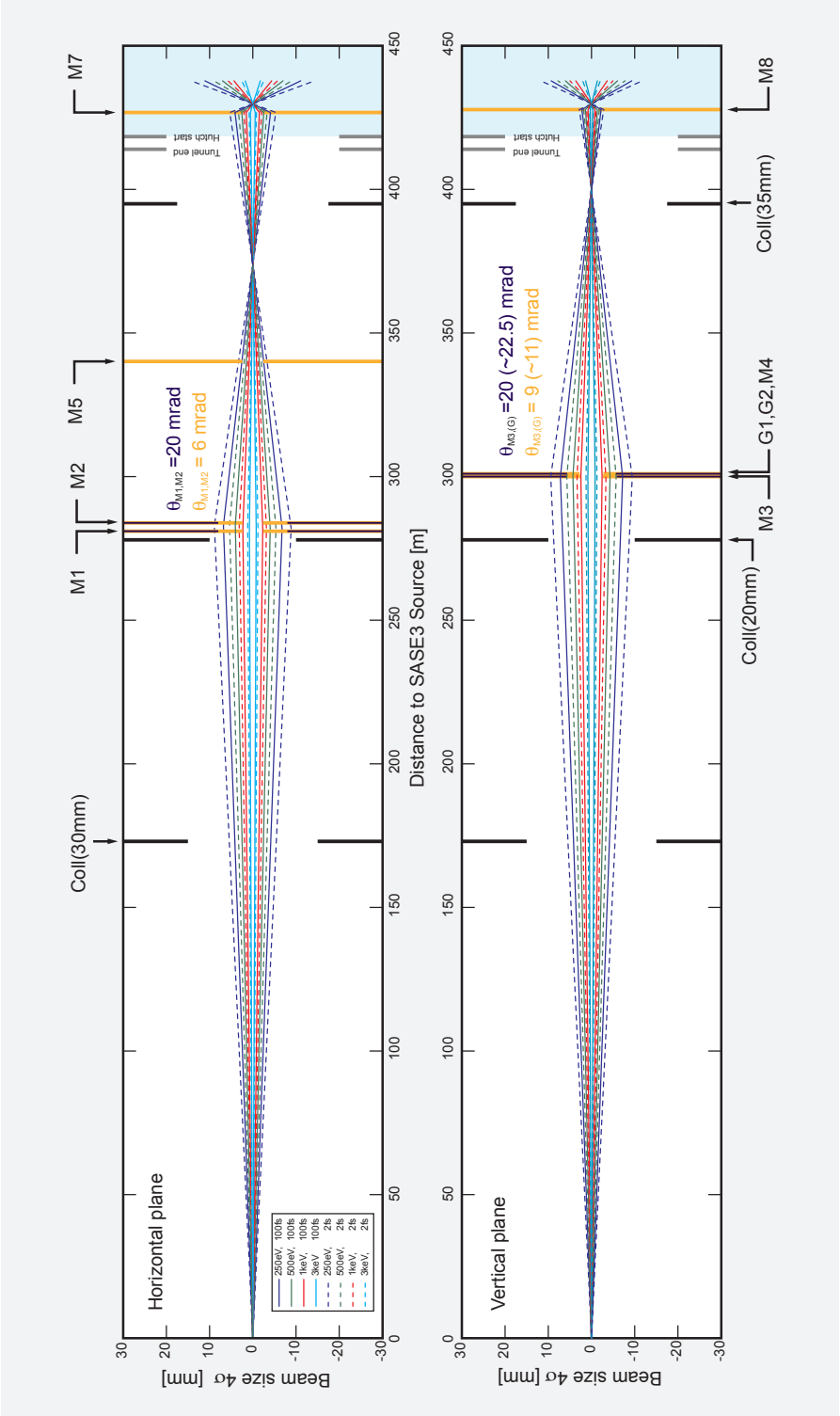

Figure 3.3: Beam size (4σ) along the SCS beam path for a set of photon energies (0.25–3 keV) and X-ray pulse durations (2 and 100 fs). Mirror apertures and collimators are indicated.

3.4 Soft X-ray monochromator

The technical design of the soft X-ray monochromator by the X-Ray Optics and Beam Transport group is described in detail in its TDR [45]. The grating chamber contains three positions for gratings. The current design foresees: (1) A 50 l/mm VLS grating G1 that provides a resolving power of 10 000 for the baseline. (2) A 150 l/mm grating G2 is planned as an upgrade that provides a resolving power of 40 000 at photon energies at absorption edges that are particularly important for high-resolution RIXS studies. (3) The third slot is a flat mirror M4 that would allow for seamless switching between pink and monochromatic operation mode. The monochromator has two different fixed-radius pre-mirrors, a pre-mirror for $\lesssim$ 1500 eV (M3b) and one for reaching higher photon energies (M3a), preserving a good performance of the monochromator over the entire energy range.

3.4.1 Grating resolving powers

The aim for very high resolving powers will limit time-resolved studies and experiments where a small spectral bandwidth or high resolution is not demanded but pulse durations on the order of the optical laser system (15 fs) or shorter are required. This leads back to path length differences introduced by the grating optics that cause pulse stretching that goes on top of the source pulse duration. The pulse stretching of a δ-like input pulse is discussed in Appendix B, "Grating performance under pulsed and shaped sources". This issue even holds for the baseline grating G1. Therefore, the concept of the soft X-ray monochromator is discussed in more detail in this CDR. One potential solution to mitigate the monochromatic pulse stretching and operate near the pulse minimum bandwidth–duration product is a controllable grating illumination, which is discussed at the end of this section. For this purpose, the resolving powers and spectral efficiencies of the gratings have been reproduced in this context using the baseline SASE3 source properties as outlined in Chapter 2, "SASE3 photon beam properties". The calculations include the illumination profile on the grating and diffraction effects, and are based on the grating illumination (second moment of the intensity distribution over the line grating) as described in Appendix B, "Grating performance under pulsed and shaped sources". The spectral efficiencies are calculated for laminar gratings with a groove depth of 15 nm. The spectral efficiencies of the actual blazed gratings are approximately a factor of 2 higher [45]. Excellent agreement is found for the resolving powers, and a reasonable description is obtained of the spectral efficiencies with calculations from WP73 that include the final monochromator working points and blazed grating angles. The latter are shown in Figure 3.4 on the next page and Figure 3.5 on page 37; they differ from the results presented in [45]. While the spectral efficiencies are consistent, the

resolving powers (RPs) of the gratings are lower overall but not diffraction-limited towards lower photon energies. However, the RPs are near the design goals under the assumption of perfect mirror surfaces. Mirror imperfection and thermal drifts of monochromator components during bunch trains will potentially reduce the monochromator performance further (estimate of 25% in [45]).

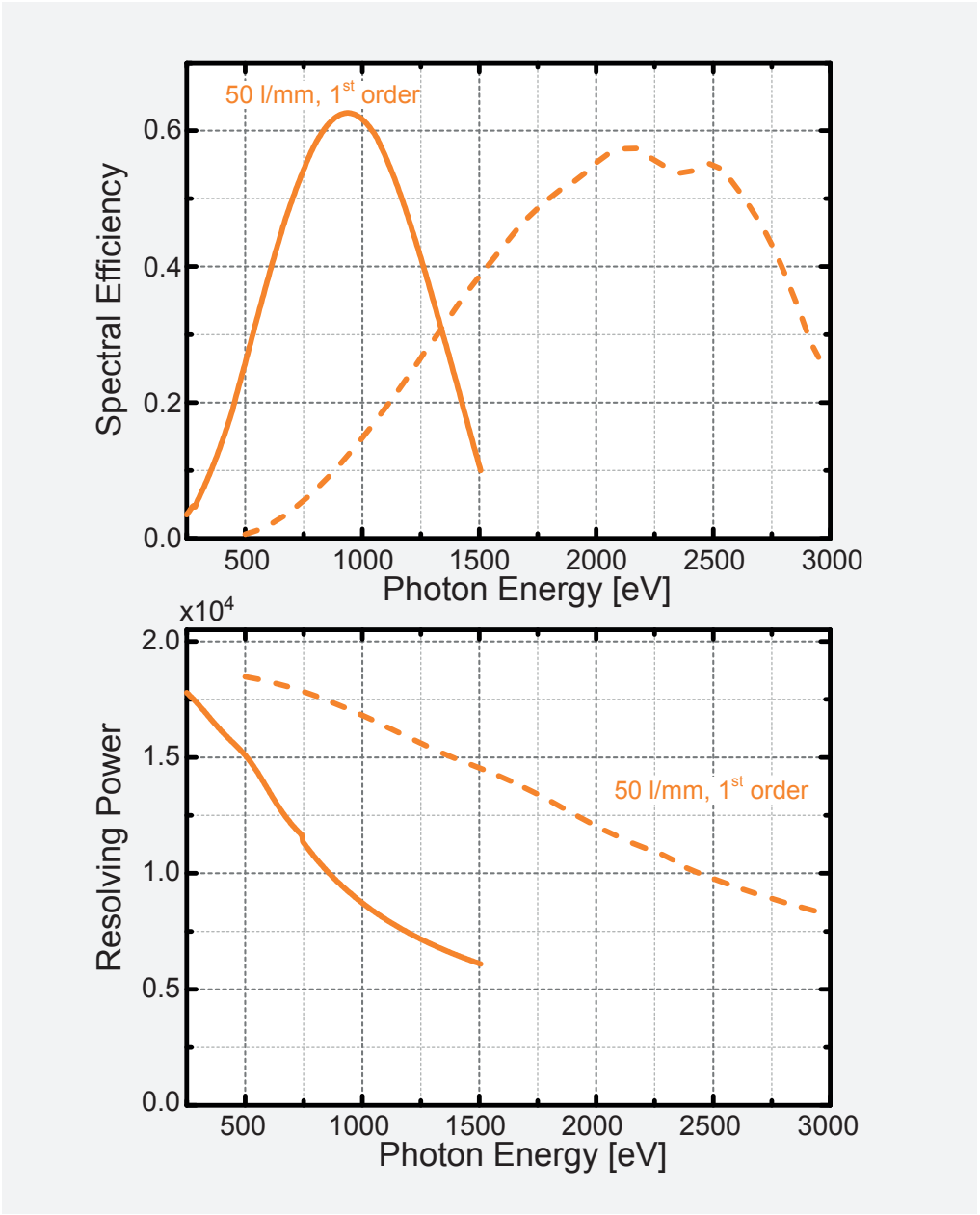

Figure 3.4: Soft X-ray monochromator: (top) spectral efficiency and (bottom) resolving power of the baseline grating G1 (50 l/mm). Mirror imperfections are not considered in this calculation, while diffraction effects are taken into account. Solid and dashed lines indicate the operating M3b and M3a pre-mirror at 20 mrad and 9 mrad incident angle, respectively. The spectral efficiency is calculated for a blazed grating angle of 0.1°.

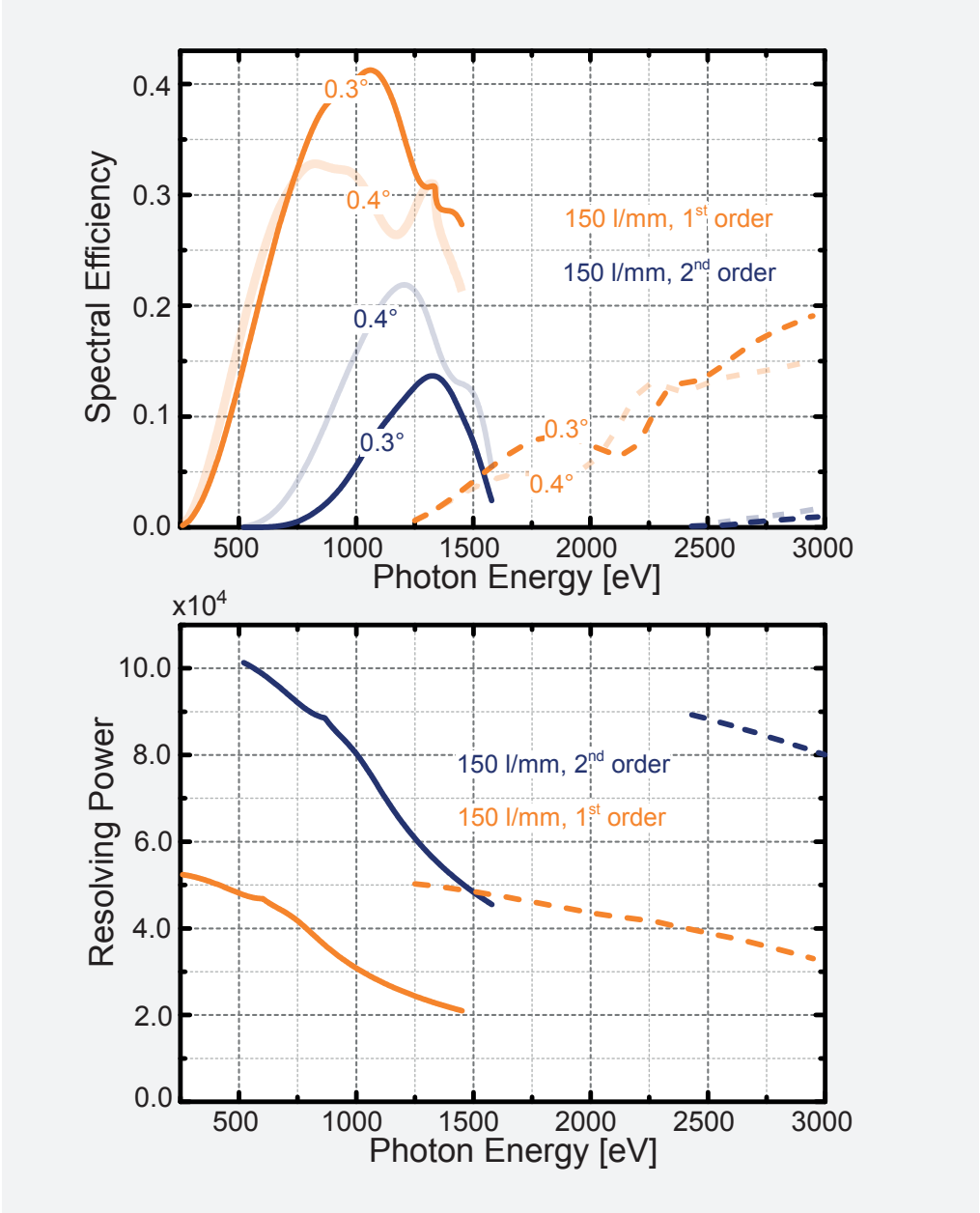

Figure 3.5: Soft X-ray monochromator: (top) spectral efficiency and (bottom) resolving power of the grating G2 (150 l/mm) that provides the high-resolution beamline extension option for the hRIXS instrument. Mirror imperfections are not considered in this calculation, while diffraction effects are taken into account. Solid and dashed lines indicate the operating M3b and M3a pre-mirror at 20 mrad and 9 mrad incident angle, respectively. The spectral efficiency is calculated for a blazed grating angle as indicated. The second diffraction order is shown as a possible extension of the resolving power for hRIXS, when needed.

The G1 and G2 gratings may produce RPs of over 10 000 and over 40 000 below ~ 750 eV. This level of resolving powers can also be reached at higher photon energies depending on the pre-mirror selection. The spectral efficiency of the high-resolution grating G2 may drop too low to have a sufficient number of photons at ≥ 40 000 RPs in the most interesting energy range of 500–1500 eV. In this case, the second diffraction order of the grating can be used. For this reason, the G2 blazed angle has been specified to 0.4°.

3.4.2 Monochromatic instrumental width and exit slit

The instrumental line spread function (LSF) is determined by the grating LSF and the focal width of the pre-mirror, and is shown in Figure 3.6 on the next page. This instrumental LSF corresponds to the resolving powers discussed in the previous section. The total resolution will finally depend on the choice of the exit slit. As the photon energy dependence of the instrumental LSF is rather weak, we consider here only the LSF mean values of the different gratings and photon energy ranges. The effective instrumental width is presented in Figure 3.7 on page 40. The nominal resolving powers can be achieved by closing the exit slit down to 15–20 µm. Resolving powers of 1000–2000 will result when opening the exit slit up to 250 µm. This possibility allows for increasing the number of photons on the sample accompanied by a proportional increase of the vertical beam size so that the pulse-integrated fluence on the sample remains constant. This mode would allow for compensating the beam loss on the entrance slit in case it is used for spoiling the monochromator resolution and for mitigating the monochromatic pulse stretching. This “spoiling” method is explained in Section 3.4.4, “Short-pulse preservation within the bandwidth–duration limits”.

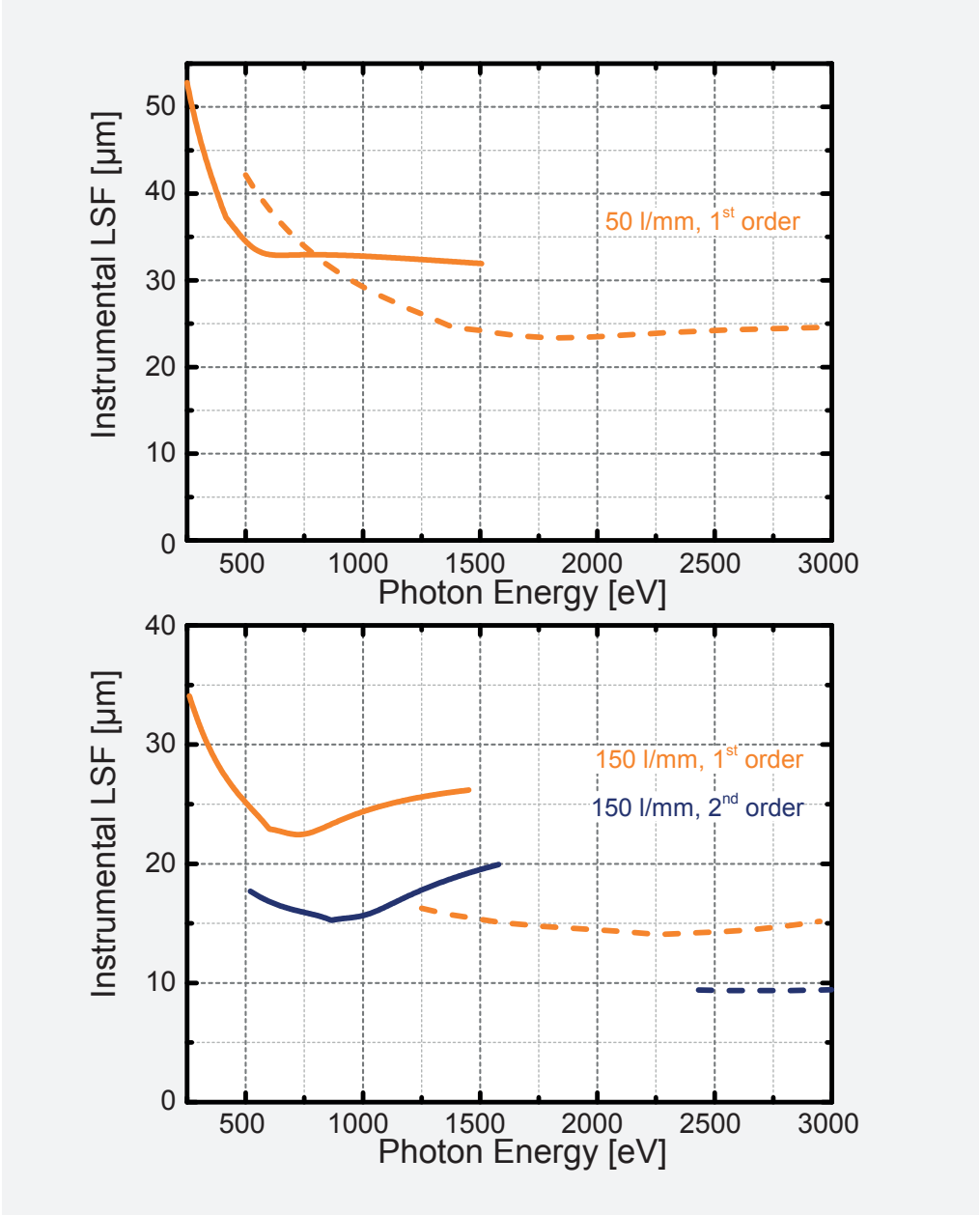

Figure 3.6: Instrumental LSF of the monochromator at the exit slit for (top) the 50 l/mm grating and (bottom) the 150 l/mm grating. This minimal instrumental width is a convolution of the grating LSF and the focal width of the pre-mirrors. Calculations are performed for 0.2 nC (20 fs pulse duration) and 14 GeV operation mode.

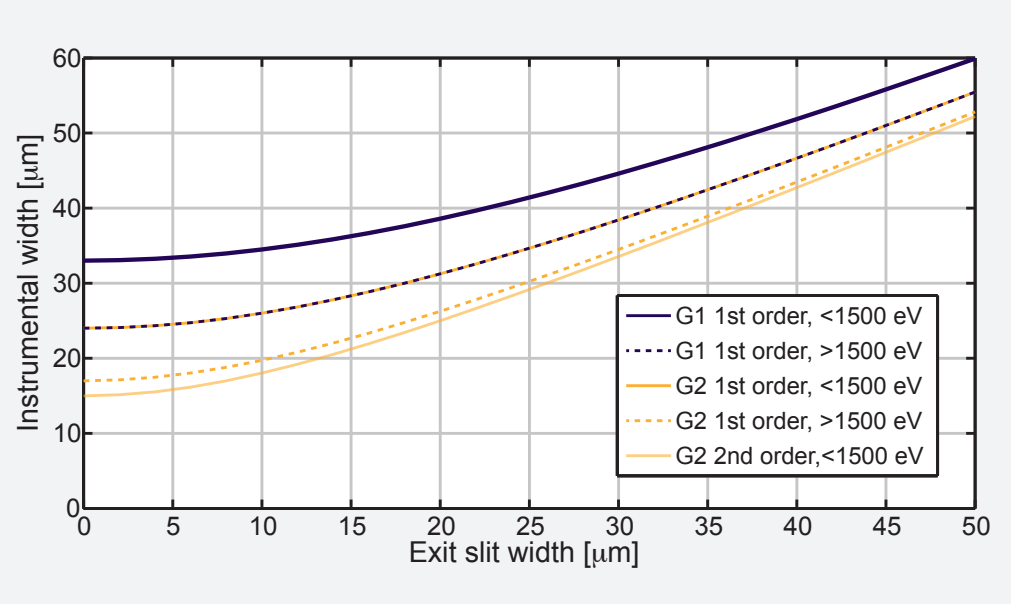

Figure 3.7: Instrumental width of the monochromator vs. the exit slit width that determines the effective resolution for the 50 l/mm (G1) and 150 l/mm (G2) gratings, as indicated. The nominal resolving powers can be achieved by closing the exit slit down to 15–20 µm.

3.4.3 Pulse durations in monochromatic mode

The monochromator pulse stretching $\Delta\tau$ is given by

$$\Delta\tau = \frac{\lambda}{c\Delta\lambda}\lambda = \frac{wd_0}{c}\lambda \tag{3.1}$$

where w is the width of the incident plane wavefront of a δ-like pulse and where $d_0 = 1/d \sin\alpha$ is the grating periodicity. More details can be found in Appendix B, "Grating performance under pulsed and shaped sources". As can be readily seen from the equation, the resolving power $\lambda/\Delta\lambda$ is given by $N = wd_0$, where N is the number of illuminated lines on the grating. For an arbitrary illumination profile of the grating over the dimension w, the resolving power and the pulse stretching can be deduced from the variance or second moment of the time delays that are generated between individual lines and are weighted by their respective illumination according to Equation B.3 on page 135.

In Figure 3.8 on the facing page, the minimum pulse durations are given for the resolving powers shown in Figure 3.4 on page 36 and Figure 3.5 on page 37. Taking experiments at the L edges of 3d transition metals (400–1000 eV), the pulse stretching imposes a ~ 70 fs pulse duration limit for time-resolved studies using the

baseline 50 l/mm grating that is given by the minimum FWHM bandwidth–duration product near the transform limit of $\Delta E \Delta \tau \geq h = 4.136$ eV · fs. Here, shortest X-ray pulses are four times longer than the optical laser system can deliver.

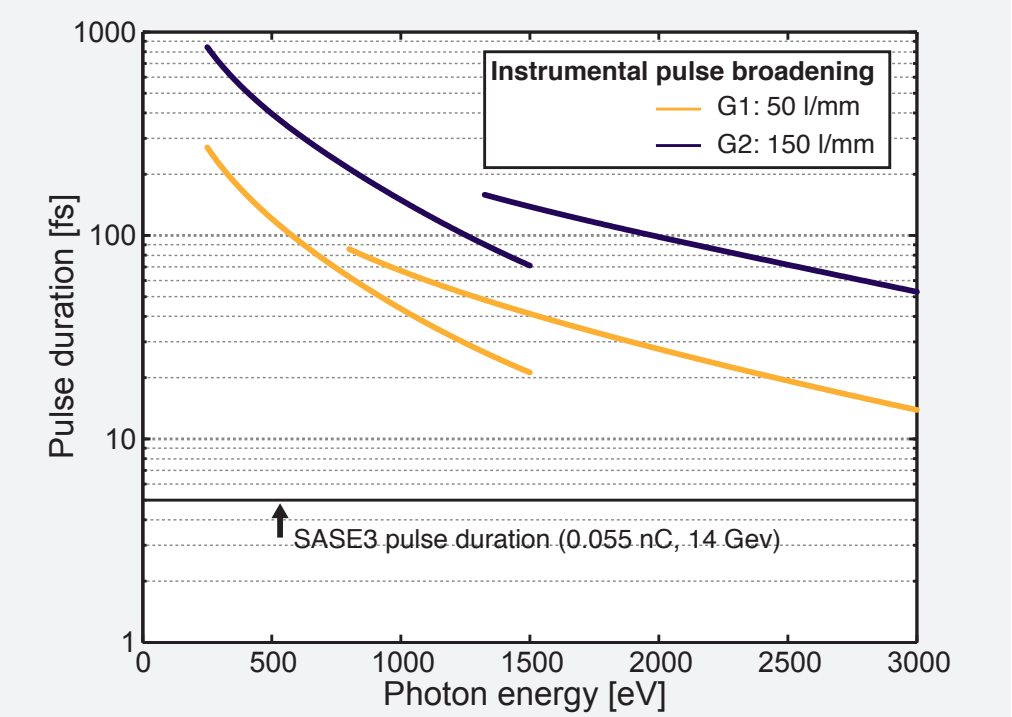

Figure 3.8: Instrumental pulse broadening of the monochromator with open entrance slit (full illumination of the gratings). Calculations are performed for 0.2 nC (20 fs pulse duration) and 14 GeV operation mode.

3.4.4 Short-pulse preservation within the bandwidth–duration limits

Two concepts can be employed at SASE3 to provide complementary sets of pulse durations and spectral bandwidths according to the needs of the user experiments. This is schematically shown in Figure 3.9 on the next page.

The first concept is to use the SASE3 self-seeding scheme, which significantly narrows the SASE3 spectral bandwidth and produces nearly transform-limited pulses [16; 43]. The simulations for 10 fs long FEL pulses indicate self-seeded energy bandwidths that corresponds to resolving powers of up to 1200 at 826 eV (1.5 nm wavelength) [16]. New calculations are under way that will explore the transform limits of this technique and how far the resolving power or bandwidth can be tuned using the

recent specifications of the SASE3 self-seeding monochromator (VLS grating with 10 000 resolving power) [43].

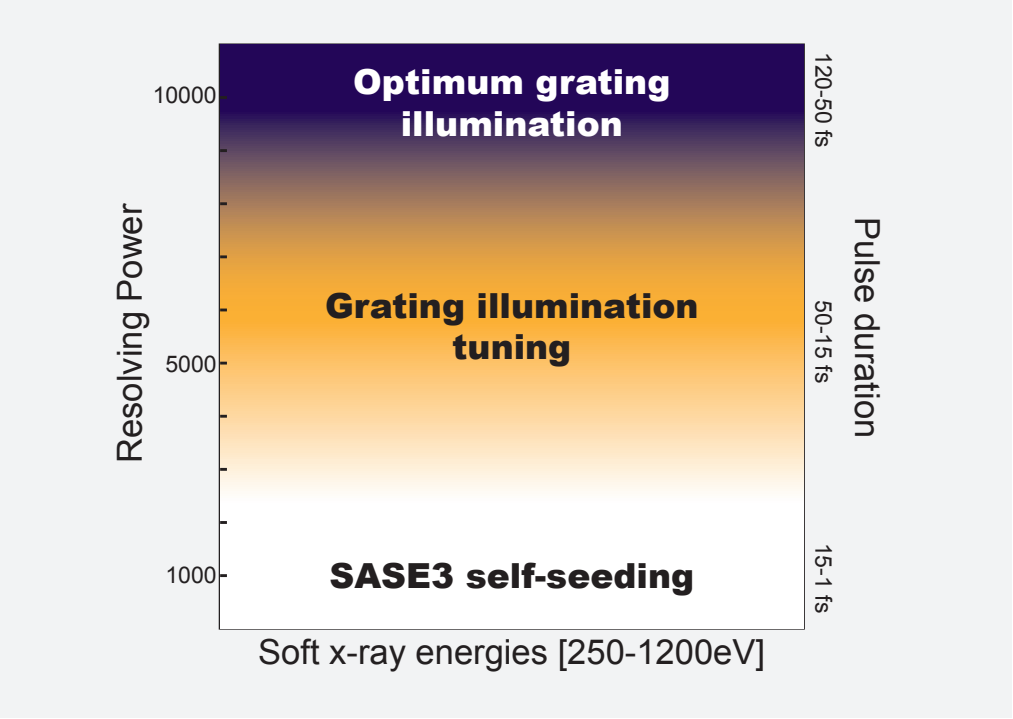

Figure 3.9: Illustration of the pulse duration and energy resolution tuning. The typical parameter space is presented for the 50 l/mm grating G1. The full time and energy scale is covered when including the soft X-ray self-seeding scheme.

The second concept is based on changing the grating illumination width and, hereby, changing the number of illuminated lines or the resolving power of the beamline monochromator. This form of “spoiling” requires an entrance slit that apertures the incident beam. Based on Equation B.3 on page 135, calculations of the resolving power and corresponding pulse duration as a function of monochromator entrance slit width have been carried out for several photon energies. The results are shown in Figure 3.10 on the next page for the G1 grating in low-charge operation corresponding to 5 fs SASE3 pulse durations. It turns out that the resolving power and pulse duration are tunable over a wide range. The clipping of the incident wavefront evidently reduces the monochromator transmission. For example, a pulse of 15 fs duration can be obtained at 1 keV with a resolving power of around 3000 when closing the entrance slit down to 4 mm. This results in a monochromator transmission that is an order of magnitude lower than the full beam transmission. This effect can be partially compensated by opening the exit slit by an amount that corresponds to the spoiled resolution, which will recover 30% of the beam intensity.

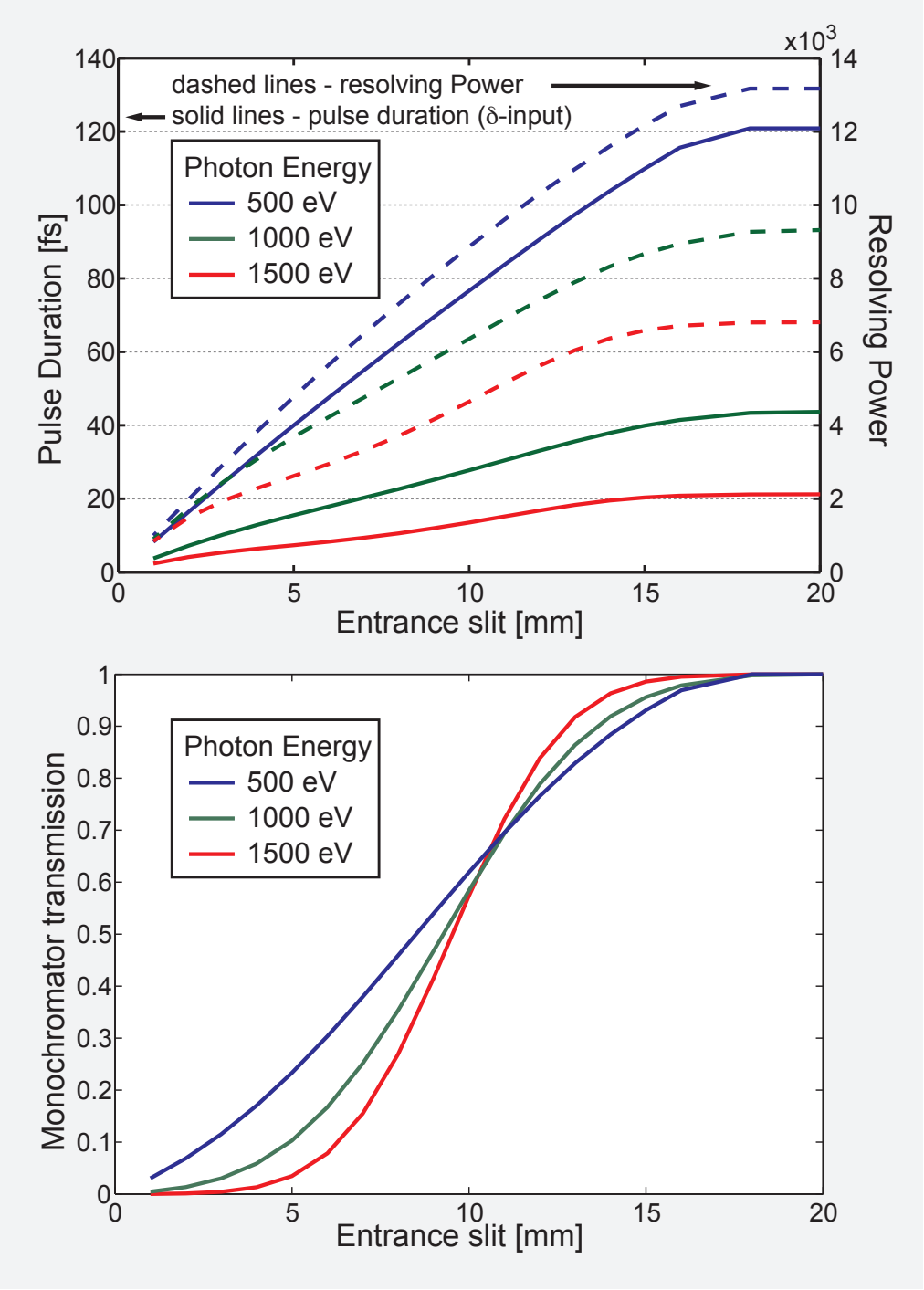

Figure 3.10: Total instrumental resolution and pulse stretching of a δ-like input pulse. G1 grating (50 l/mm), changing pulse durations. The beam operation parameters used for the calculation are 14 GeV and 0.055 nC, which corresponds to 5 fs long pulses.

3.5 KB refocusing optics

As outlined in Chapter 1 on page 13, "Scope of the SCS instrument", the diverse spectroscopy and coherent scattering techniques have very different requirements in terms of beam size on the sample. In practice, a variable beam size turns out to be the best approach to make optimum use of the delivered photons per FEL pulse in each experiment. The KB refocusing conceptual design therefore considers a bent mechanism that allows for moving the focus along the beam axis. At fixed sample interaction point, this feature could provide a variable beam size over three orders of magnitude. Such KB bent refocusing systems are employed at the soft X-ray beamlines of the Linac Coherent Light Source (LCLS) at SLAC National Accelerator Laboratory in Menlo Park, California.

Requirements for the KB refocusing optics

- Variable beam size at sample position, 1–1000 µm
- Mitigate wavefront distortions within 1–10 µm for CXDI
- Avoid diffraction effects ($4\sigma_{\text{beam}}$ < mirror aperture)
- RIXS: vertical ≤ 5 µm and horizontal beam size variable up to 1000 µm
- High transmission for the energy range 0.25–3 keV
- Operation at high FEL repetition rate (requires mirror cooling)

3.5.1 Working with intermediate source points

The X-ray optical layout of the SASE3 instrument provides the option of operating with an intermediate source point in the horizontal and vertical planes. This enables us to modify the source point position, which in turn changes the beam refocusing by the KB optics, i.e. M7 (horizontal) and M8 (vertical). The vertical intermediate focus is given by the exit slit of the monochromator. Having an intermediate source point has the advantage of limiting the beam size in the experiment hutch, in particular for the lower photon energies (Figure 3.3 on page 34). The optical length requirements of the KB mirrors in order to prevent diffraction effects in the sample focus become less demanding. At higher photon energies (> 2 keV), where the beam divergence is smaller, operation without intermediate source points is possible. In this case, SASE3 is the source point for the KB refocusing system and a smaller sample focus (approximately 2×) is in principle possible within the geometrical and diffraction limits. The focal size may ultimately be limited by mirror imperfections and the performance

of the KB bent mechanism. Both the horizontal and the vertical intermediate source points are therefore an integral part of the KB conceptual design.

3.5.2 Conceptual design

The starting point for the conceptual design is the definition of further boundary conditions. The minimum distance between the KB mirrors and the sample interaction point is given by the length of the optical laser in-coupling, timing diagnostics, differential pumping, and thin film–based solid beam attenuator that are described in Chapter 7, “Instrument diagnostics", and Chapter 8, “Optical laser delivery”. The current design estimates that a nominal focus of 2 m for the vertical KB mirror M8 provides sufficient space for the additional instrumentation. This defines the geometrical limit of the KB focus in the vertical direction with a source demagnification of 13.9 (monochromatic mode / vertical intermediate focus) and 213.9 (SASE3 source point).

In the next step, the diffraction limit of the vertical KB focus, which defines the suitable KB mirror aperture, has to be investigated. In order to ensure high transmission of the KBs for the full photon energy range, an incident angle of $\theta = 9$ mrad is required. As shown in Chapter 2, “SASE3 photon beam properties”, the source divergence increases the lower the photon energy and the lower the bunch charge. This conditions lead to an optical mirror length of at least 350 mm in the vertical and a respective mirror aperture of 3.2 mm, which is shown in Figure 3.3 on page 34.

The specifications for the horizontal KB mirror M7 are then defined along the same line of considerations for M8. We require a similar demagnification of the source point in the horizontal direction in order to achieve a rather round lateral beam spot on the sample. A focal length of 3.33 m would satisfy this conditions without having the KB mirrors too far apart from each other. A minimum optical length of 500 mm is required corresponding to a mirror aperture of 4.5 mm, which is shown in Figure 3.3 on page 34.

The geometrical focus and the sum of diffraction-limited and geometrical focus size (FWHM) are shown in Figure 3.11 on the following page, Figure 3.12 on page 47, and Figure 3.13 on page 48 for monochromatic-beam operation (G1 and G2), pink-beam operation using a vertical intermediate source point (M4), and pink-beam operation without intermediate source points, respectively.

The vertical beam size in the focus will depend on the exit slit setting of the monochromator (Figure 3.11 on the next page), which has been set for this

calculations to 20 µm. This limits the geometrical beam size to 1.5 µm. The beam size further increases by up to 15% due to the contribution of the diffraction effects. The horizontal focus size is smaller overall than the vertical one and varies more with photon energy. When operating the monchromator in pink-beam mode, and thereby keeping the intermediate source point at the exit slit, the vertical beam focus approaches the dimension of the horizontal one, as shown in Figure 3.12 on the facing page. Figure 3.11 shows the focus dimension when no intermediate source point is chosen and when SASE3 is the source point. The pink-beam operation will provide beam sizes that are about a factor of 2 smaller, down to 0.5 µm in diameter.

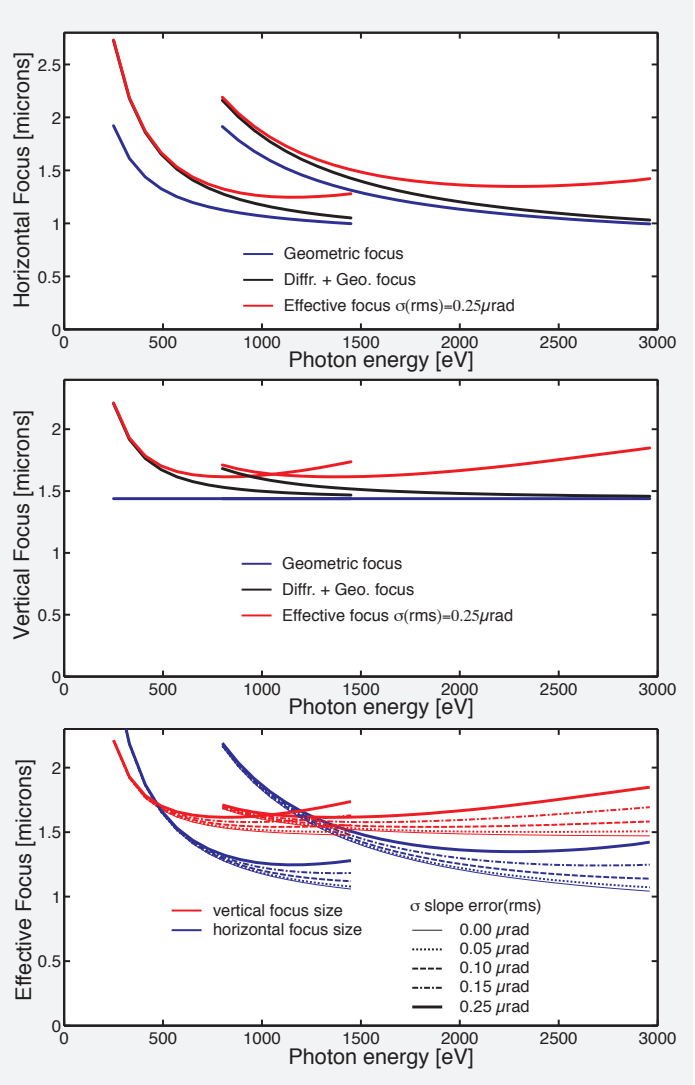

Figure 3.11: KB focus at the sample in monochromatic-beam operation: Geometrical focus (blue), sum of geometrical and diffraction-limited focus (black), and effective focus (red) accounting for 250 nrad (rms) slope error of the horizontal (top) and vertical (middle) mirrors. The bottom panel shows the vertical (red) and horizontal (blue) focus size for a set of slope errors.

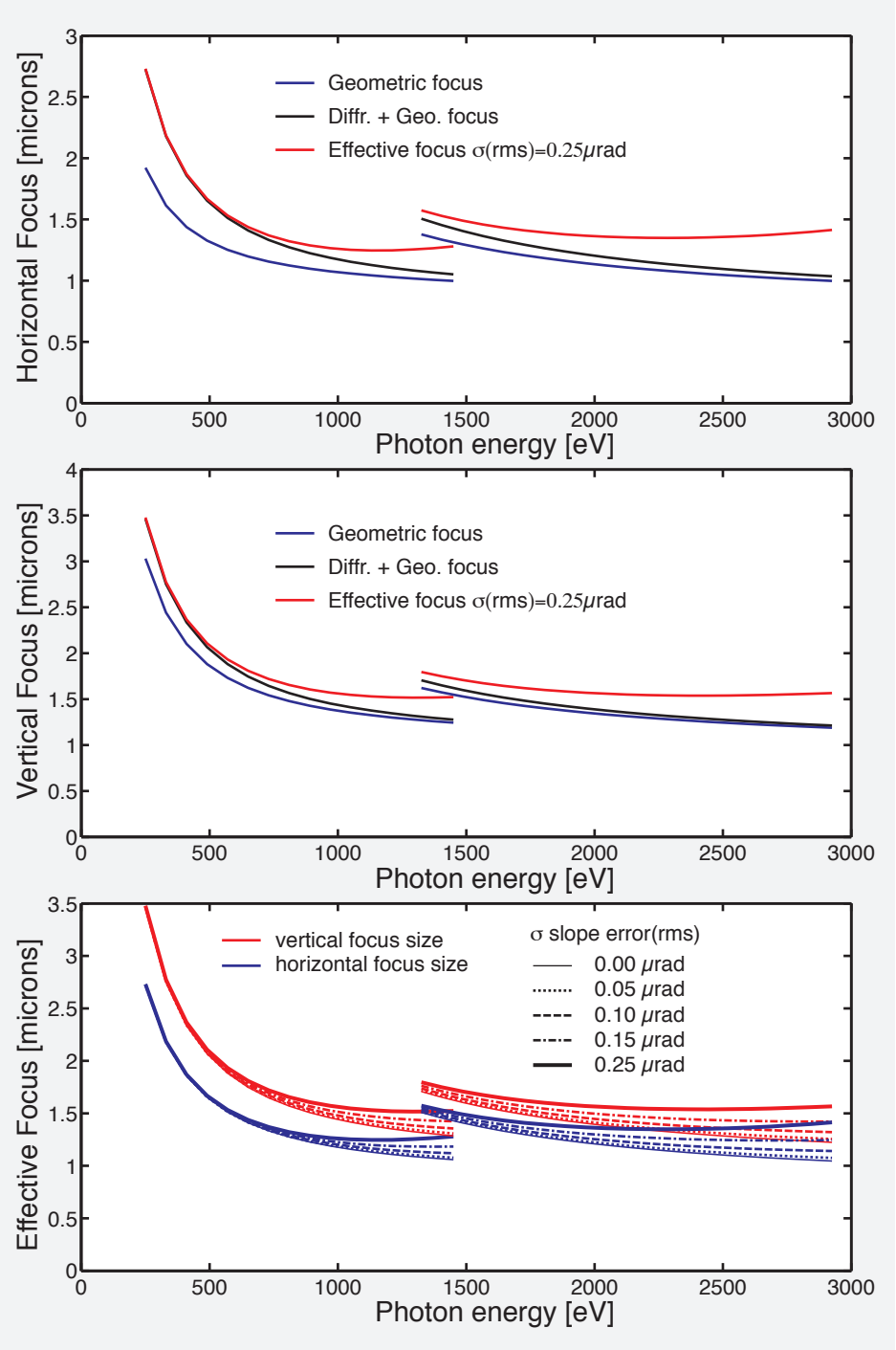

Figure 3.12: KB focus at the sample in pink-beam operation with intermediate source points: Geometrical focus (blue), sum of geometrical and diffraction-limited focus (black), and effective focus (red) accounting for 250 nrad (rms) slope error of the horizontal (top) and vertical (middle) mirrors. The bottom panel shows the vertical (red) and horizontal (blue) focus size for a set of slope errors.

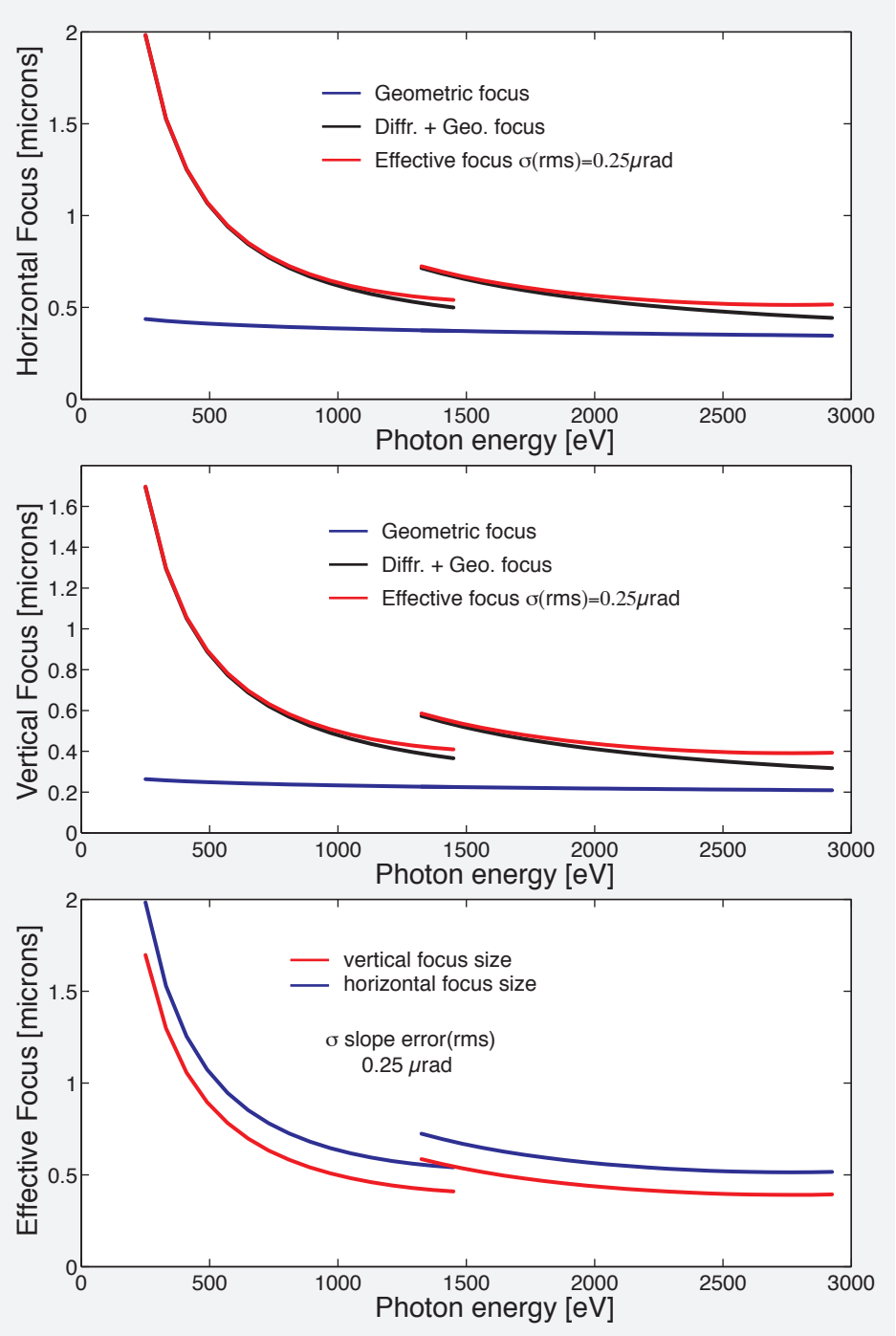

Figure 3.13: KB focus at the sample in pink-beam operation with a SASE3 source point: Geometrical focus (blue), sum of geometrical and diffraction-limited focus (black), and effective focus (red) accounting for 250 nrad (rms) slope errors of the horizontal (top) and vertical (middle) mirrors. The bottom panel shows the vertical (red) and horizontal (blue) focus size for 250 nrad (rms) slope error.

3.5.3 KB mirror focus, mirror roughness, and slope error specifications

High-quality coherent X-ray optics with σ = 50 nrad slope error over a 350 mm optical length have been achieved by deterministic polishing [44]. The key challenge for the KB system remains to reach sufficiently low slope errors with a bent mechanism and water cooling attached.

We performed simulations for studying the effect of slope errors on the mirror imaging quality. The simulations are based on a statistical approach of residual height errors expressed by the power spectral density (PSD) of the mirror surface, a quantity that can be deduced from profile measurements in the laboratory. The simulations follow the formalism proposed by Church and Takacs [8], which provides a generalized description for mirror specifications and produces an ensemble average image intensity distribution from which beam size and peak intensity reduction can be obtained. The slope error profile from Ref. [44] has been used for the calculation and is shown in Figure 3.14 on the following page. The slope error has been scaled to produce different slope errors in the simulation. The PSD function (Figure 3.15 on page 51) and intensity distribution in the focus are then calculated from the resulting height errors.

A common way to describe the quality of a mirror is the Strehl ratio, which is the ratio between the achieved peak intensity and the ideal peak intensity in the image of an optical system. For details, see e.g. [44]. It is generally considered that a high-quality mirror has a Strehl ratio of 0.8 or larger, which leads to the Marechal criterion

$$\Delta h_{\mathrm{rms}} \leq \frac{\lambda}{14\sqrt{N}2\theta} \tag{3.2}$$

where λ is the wavelength, N the number of reflecting surfaces, and θ the beam incident angle to the mirror surface. This equation shows that, with shorter wavelengths or higher photon energies, the rms height error over all spatial frequencies of the mirror surface has to decrease to meet the Marechal criterion. Therefore, high-quality coherent optics for the hard X-ray range are technically more demanding than the ones for soft X-rays.

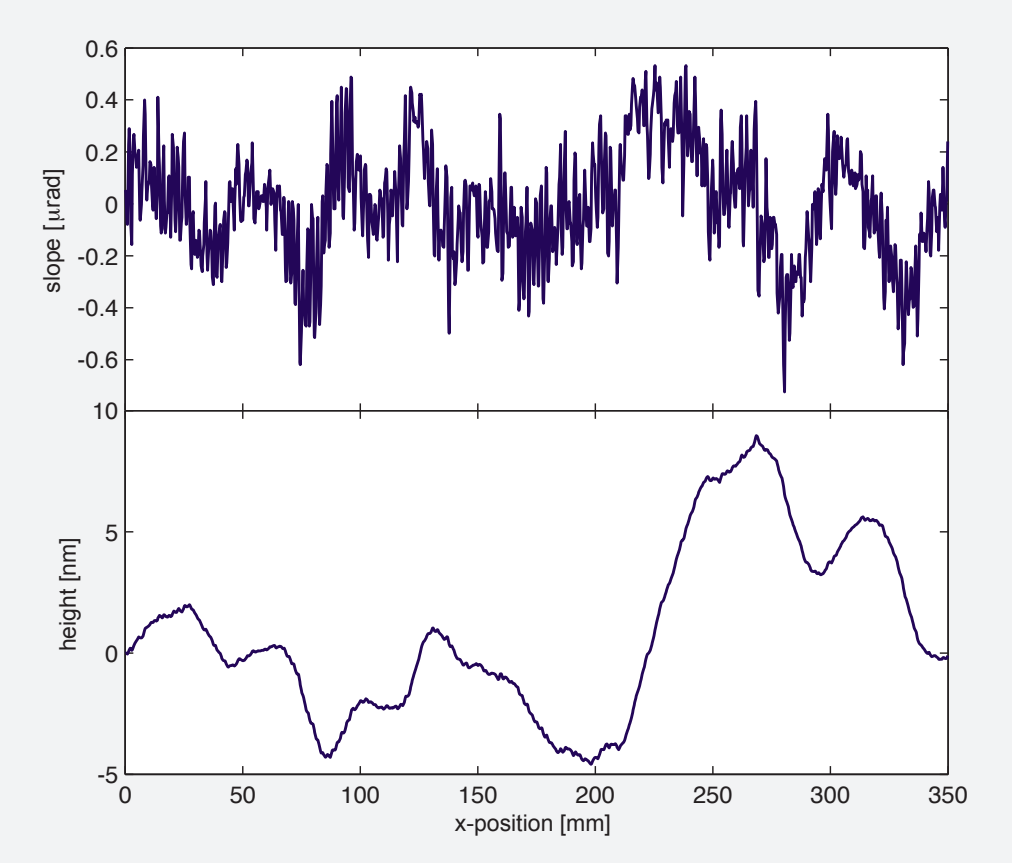

Figure 3.14: Simulation of height and slope error effects based on actual measurements from [44]: (top) The dataset has been scaled to produce a slope error of $\sigma_{\text{slope}} = 0.25$ µrad. (bottom) The corresponding residual height error of the mirror surface ($\Delta h_{\text{rms}} = 3$ nm).

This tendency is reflected in the results shown in the bottom panels of Figure 3.11 on page 46 and Figure 3.12 on page 47, which show the focus size as a function of photon energy for different slope errors. The simulations suggest that slope errors of 250 nrad are tolerable for photon energies up to 3 keV. This corresponds to $\Delta h_{\text{rms}} = 3$ nm. For photon energies below 1 keV, even larger slope errors may be acceptable. Finally, it should be noted that all X-ray optics in the SCS beamline have to be taken into consideration. Omitting the X-ray beam split and delay line, the minimum number of optical elements is $N_{\text{hor}} = 4$ and $N_{\text{ver}} = 3$ in the horizontal and vertical plane, respectively. This means, according to the Marechal criterion, that height errors must be limited to ≤ 2 nm (rms) in order to preserve the geometrical focus properties in the high photon energy range.

The simulation represents an ensemble average of coherent X-ray optics that reveal the same spatial–frequency dependence of the PSD function. In the following section,

results of wavefront propagation simulations are presented that have been carried out to investigate the beam profile of a coherently illuminated mirror.

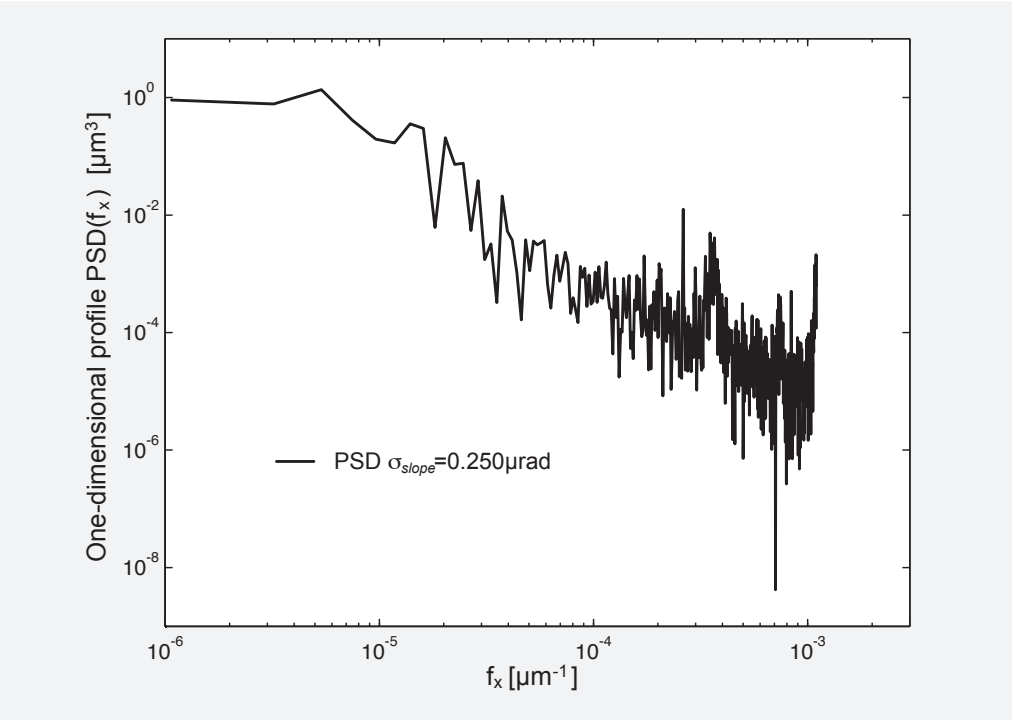

Figure 3.15: One-dimensional profile power spectral density (PSD) of the mirror surface that results from scaled height errors in Figure 3.14 on the preceding page corresponding to σ_{slope} = 0.25 µrad.

3.5.4 Wavefront propagation results

In collaboration with WP73, we started wavefront simulations to investigate the KB performance in terms of the beam profiles at the sample position. The source point in these calculations is described by the SASE3 source divergence using the parameterization presented in Section 2.1, “SASE3”. The code simulates the propagation of a Gaussian wave packet so that the source size is then given by the preselected source divergence. As a result, the source size is typically underestimated in the wavefront propagation simulations by 20–30%. The calculated beam sizes at the sample position are therefore smaller than the ones presented in Section 3.5.3, “KB mirror focus, mirror roughness, and slope error specifications”.

The results are listed in Table 3.2 on the following page for 500, 800, 1500, and 3000 eV. The results can be compared with the beam sizes that have been obtained for pink-beam operation with intermediate source points in Figure 3.12 on page 47

since the exit slit of the monochromator was not included in the simulations. Overall, the beam size is underestimated by 10%, but the relative increase of the beam size caused by the slope errors across the photon energies are in reasonable agreement with the results in Figure 3.12 on page 47. The beam sizes at low photon energies (< 1500 eV) are more or less unaffected for slope errors < 380 nrad (rms), while the beam sizes at high photon energies are impacted by up to 100% increase in size. Since the wavefront propagation results suggest that slope errors of ≤ 250 nrad (rms) would increase the beam size at 3 keV by up to 5% only, we specify for the KB mirrors a maximum slope error of 250 nrad (rms) at the nominal focus. The beam profiles in the nominal focus of the KB refocusing mirrors is shown in Figure 3.16 on the next page for a slope error of 250 nrad (rms).

Table 3.2: Wavefront propagation results of the beam size in the nominal focus of the KB refocusing optics as a function of slope errors σ (rms) and photon energies

Nominal focus size [µm]	$\sigma_{\text{slope.err}}$ **0.0 µrad**	$\sigma_{\text{slope.err}}$ **0.042 µrad**	$\sigma_{\text{slope.err}}$ **0.168 µrad**	$\sigma_{\text{slope.err}}$ **0.254 µrad**	$\sigma_{\text{slope.err}}$ **0.381 µrad**
hor @ 500 eV	2.17	2.17	2.17	2.18	2.18
ver @ 500 eV	1.94	1.94	1.94	1.94	1.94
hor @ 800 eV	1.20	1.20	1.20	1.20	1.21
ver @ 800 eV	1.44	1.44	1.44	1.45	1.46
hor @ 1500 eV	1.01	1.01	1.05	1.12	1.68
ver @ 1500 eV	0.98	0.98	1.00	1.03	1.12
hor @ 3000 eV	0.82	0.83	0.91	1.12	1.68
ver @ 3000 eV	0.98	0.98	1.00	1.03	1.12

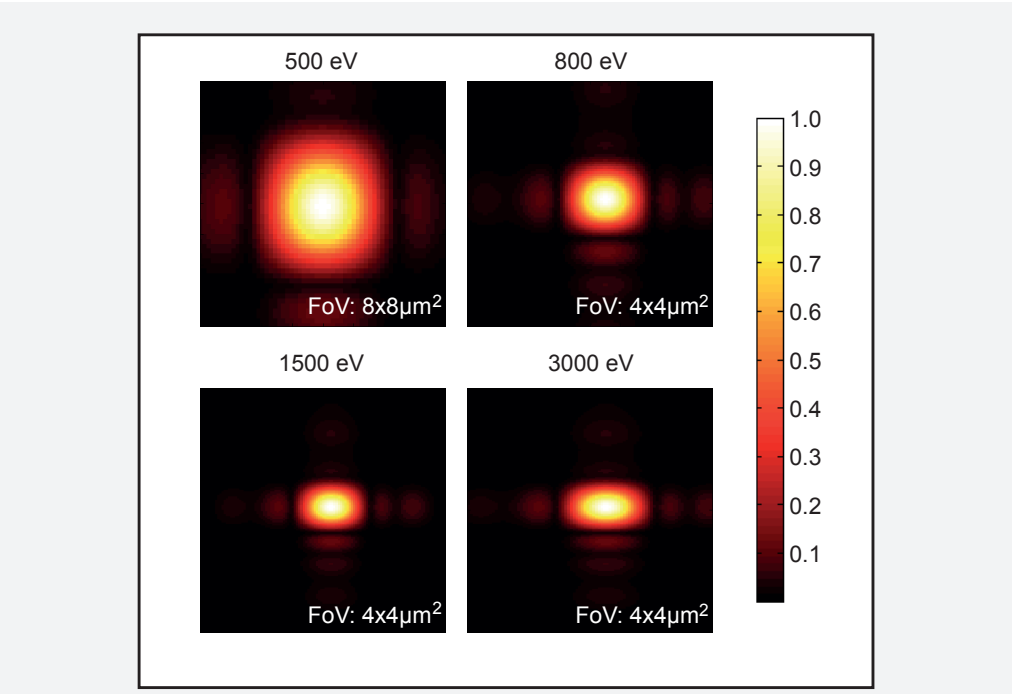

Figure 3.16: Wavefront propagation results of the beam profile in the nominal focus of the KB mirrors (FoV: Field of View)

3.5.5 Near-focus beam properties

Larger beam sizes up to tens of micrometres can be achieved in the near-focus region. We can define this range in terms of the Rayleigh range or focus depth, which is twice the Rayleigh range. The Rayleigh range characterizes the distance from the focus where wavefront curvatures occur and start to contribute to the beam profile. However, the beam profile may still have rather structureless features near the Rayleigh range.

For CXDI experiments, a variable beam size from 1–10 µm is required to cover different sample sizes. Table 3.3 on the following page lists the ratio of the upstream sample position to the Rayleigh length that is required for a 10 µm beam size (FWHM) at the sample for different photon energies. This suggests that, for < 1000 eV photon energies, this requirement can be met within the Rayleigh length. For sufficiently low slope errors, the beam quality may then be well maintained, see wavefront propagation results for the TDR of the Single Particles, Clusters, and Biomolecules (SPB) instrument at 1.8 times the Rayleigh length [29].

Table 3.3: KB refocusing: 10 µm beam size in the near focus in terms of depth of focus (twice the Rayleigh range)

Photon energy [keV]	10 µm horizontal offset / Rayleigh length	10 µm vertical offset / Rayleigh length	Rayleigh length (hor, ver) [mm]
0.5	0.4	0.4	(23.6, 24.6)
1.0	0.7	0.7	(17.2, 22.2)
2.0	1.2	1.0	(17.8, 28.2)
3.0	1.4	1.1	(22, 36)

Figure 3.17 on the next page shows wavefront propagation results for the SCS KB mirrors with 250 nrad (rms) slope errors at 800 eV. A beam size of 10 µm is obtained for 16 mm upstream offsets to the nominal focus or about one Rayleigh length. The beam structures originate from the slope errors of the KB mirrors (not shown). A significant improvement of the beam profile can be achieved for slope errors < 150 nrad (rms) where structureless beam profiles can be achieved at 50 nrad. Such small slope errors on mirror surfaces can be produced but are challenging to achieve with a mirror bent mechanism. The specification of the mirror surface will therefore be 50 nrad slope errors before bending. The metrology will then optimize the mirror bent mechanism for the nominal focus, with the smallest and reproducible slope error achievable, but no more than 250 nrad.

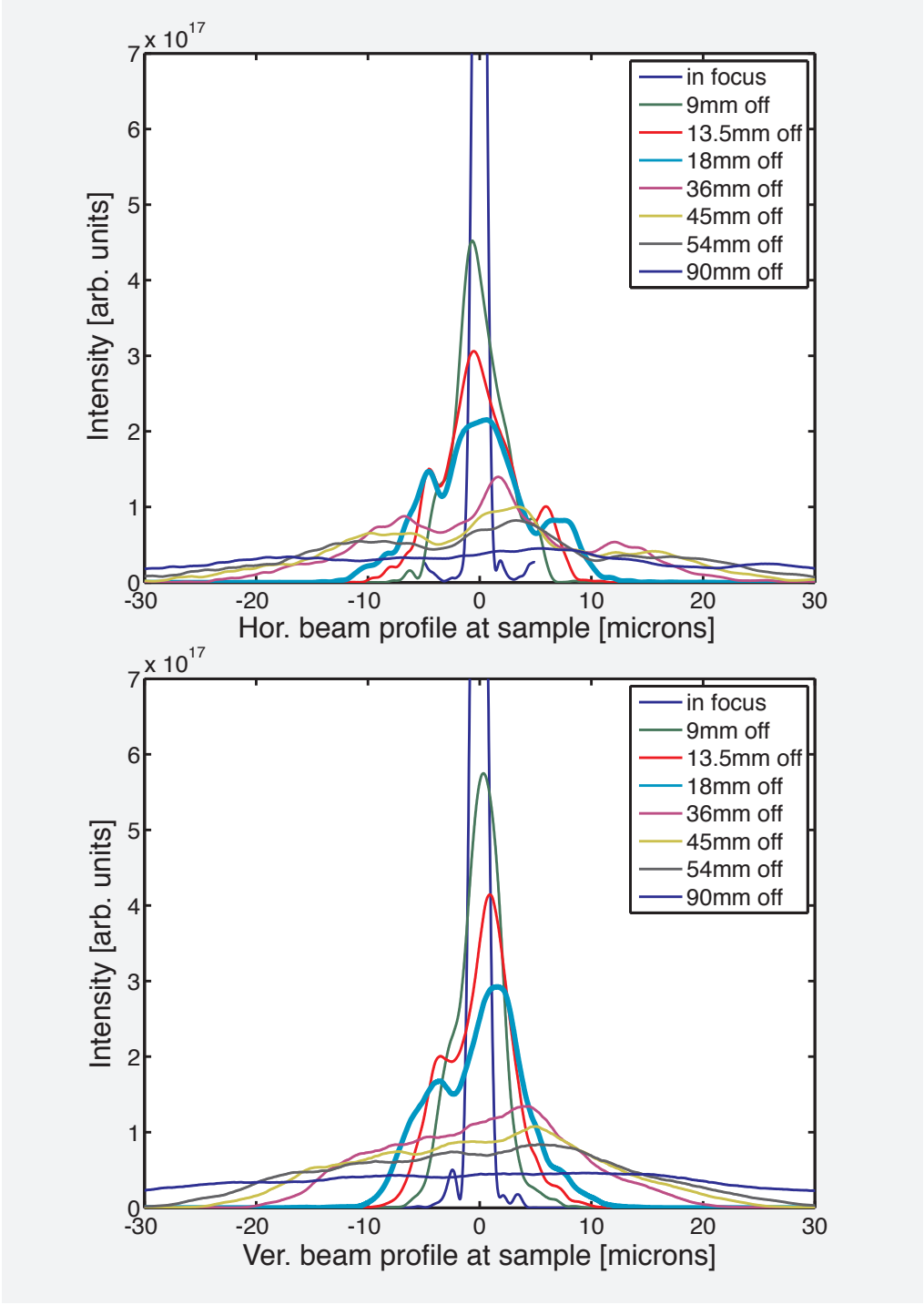

Figure 3.17: Wavefront propagation results in near-focus regime at 800 eV

3.5.6 Out-of-focus beam sizes

For beam sizes larger than 10 µm, the bent mechanism of the KB mirrors can be used to move the focus position further downstream of the sample position. The beam profile will sustain structures imposed and accumulated by the imperfections and apertures of the beamline mirrors. For time-resolved pulse-averaged studies, this poses minor problems as long as even hot spots in the beam remain under the sample damage thresholds. The pulse-to-pulse variation in the beam structure will average out in the experimental data. The beam size can be varied up to 1 mm at soft X-ray energies (< 1 keV) by moving the focus downstream by 2–6 m. This defines in principle the useful beam bending range for the mirrors (Figure 3.18).

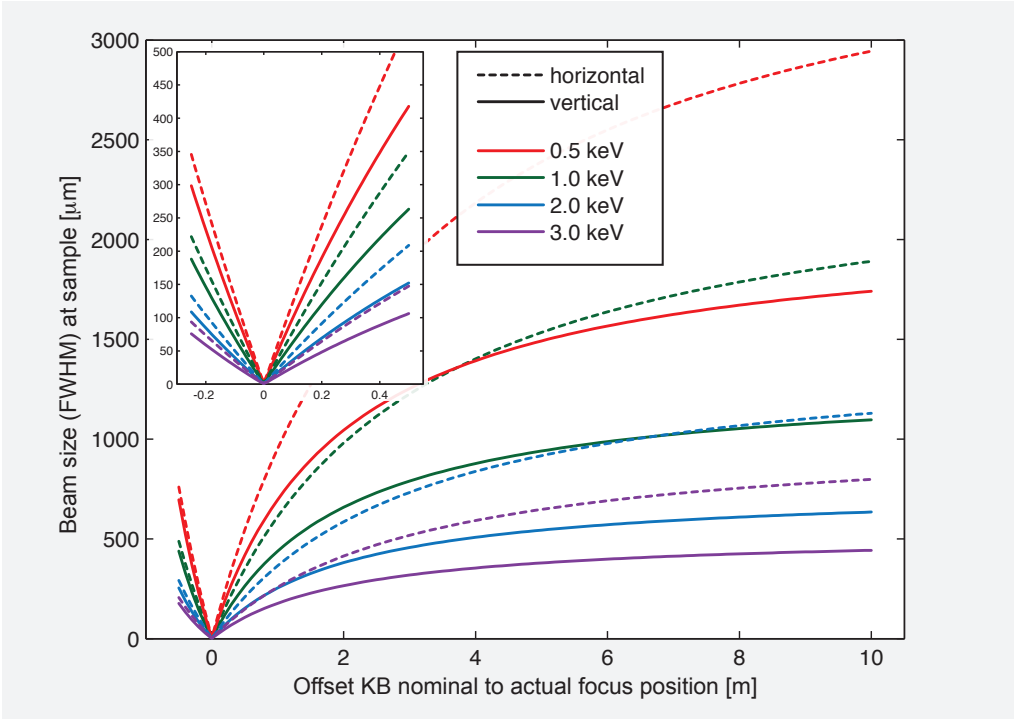

Figure 3.18: Out-of-focus beam sizes: Beam size at the sample in the nominal focus as a function of focus offset (= actual to nominal focal distance) along the optical axis by mirror bending

3.5.7 Bent mechanism

Which type of bent mechanism for the KB mirrors can achieve slope errors of < 250 nrad (rms) is currently an open subject. The technical feasibility of KB bent refocusing optics with these specifications has to be discussed with potential vendors and is beyond the scope of this CDR. It should be noted that these specifications have to be met for the nominal focus only. A standard approach would be to start with flat KB mirrors with slope errors of 50 nrad, and then apply a bent at the end of mirror substrates with a leaf spring mechanism to form the mirror ellipse for the nominal focus [21]. The nominal radius is 348 and 207 m for the horizontal and vertical mirror, respectively. The horizontal mirror figure is shown in Figure 3.19. In order to produce the elliptical figure from a flat mirror, the bent actuators have to exert a force that corresponds to a bent of ~ 50 µm at the ends of the mirror. Assuming equal forces at the ends of the mirrors, an elliptical figure can also be approximated by a length-dependent mirror width. The mirror width profile (80 mm minimum mirror width) for a mirror height of 50 mm is shown as an example in the bottom panel of Figure 3.19. The final height, width, and substrate length of the mirrors will be depend on the technical design of the bent mechanism that will be specified in the SCS TDR.

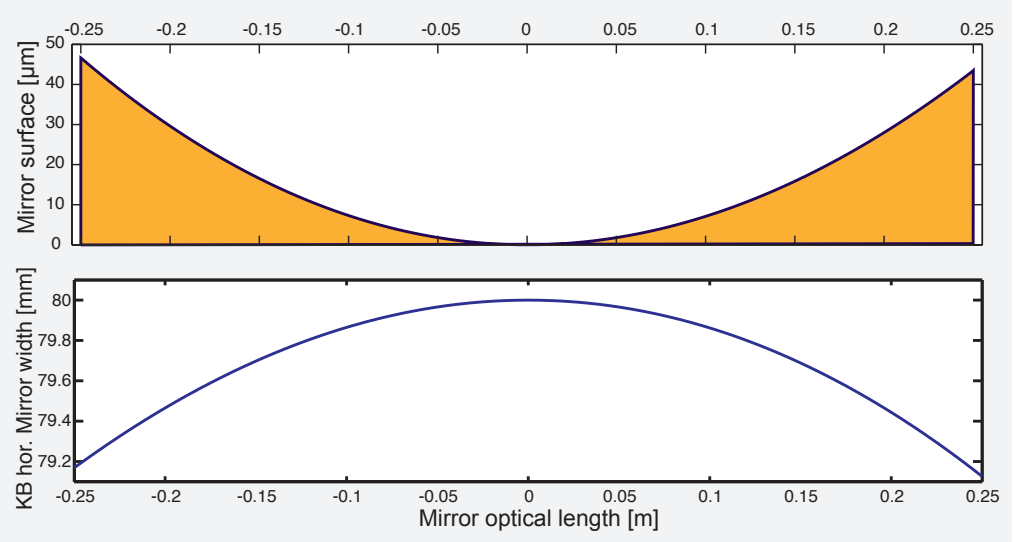

Figure 3.19: Mirror surface and width profile to approximate ellipse

3.5.8 Summary of KB mirror specifications

The current specifications of the KB mirrors as detailed in this section are summarized in Table 3.4.

Table 3.4: KB bent mirror specifications for the nominal focus

Specification	**Horizontal KB (M7)**	**Vertical KB (M8)**
Optical length	$\geq$ 500 mm	$\geq$ 350 mm
Dist. intermediate focus	52.5 m	27.8 m
Nominal focus f_0	3.33 m	2.0 m
Demagnification	15.8	13.9
Incidence angle	9 mrad	9 mrad
Figure	Ellipse	Ellipse
Radius	348 m	207 m
Slope error (rms)	$\leq$ 250 nrad	$\leq$ 250 nrad
Coating	B_4C	B_4C
Coating thickness	50 nm	50 nm
Substrate	800 mm	500 mm
Width	80 mm	80 mm
Height	50 mm	50 mm

3.6 X-ray beam split and delay line

A beam splitter in the SASE3 X-ray beam transport system enables X-ray pump, X-ray probe, interferometric experiments and nonlinear X-ray science. Wavefront division beam splitters have been successfully operated at UV–XUV energies at the Free-Electron Laser in Hamburg (FLASH) at Deutsches Elektronen-Synchrotron (DESY), Germany, with delay lines of up to 20 ps [31; 47]. The principle is illustrated in Figure 3.20. A simple two-mirror split and delay device with up to 150 fs time delays has been commissioned for the LCLS soft X-ray beamlines [32].

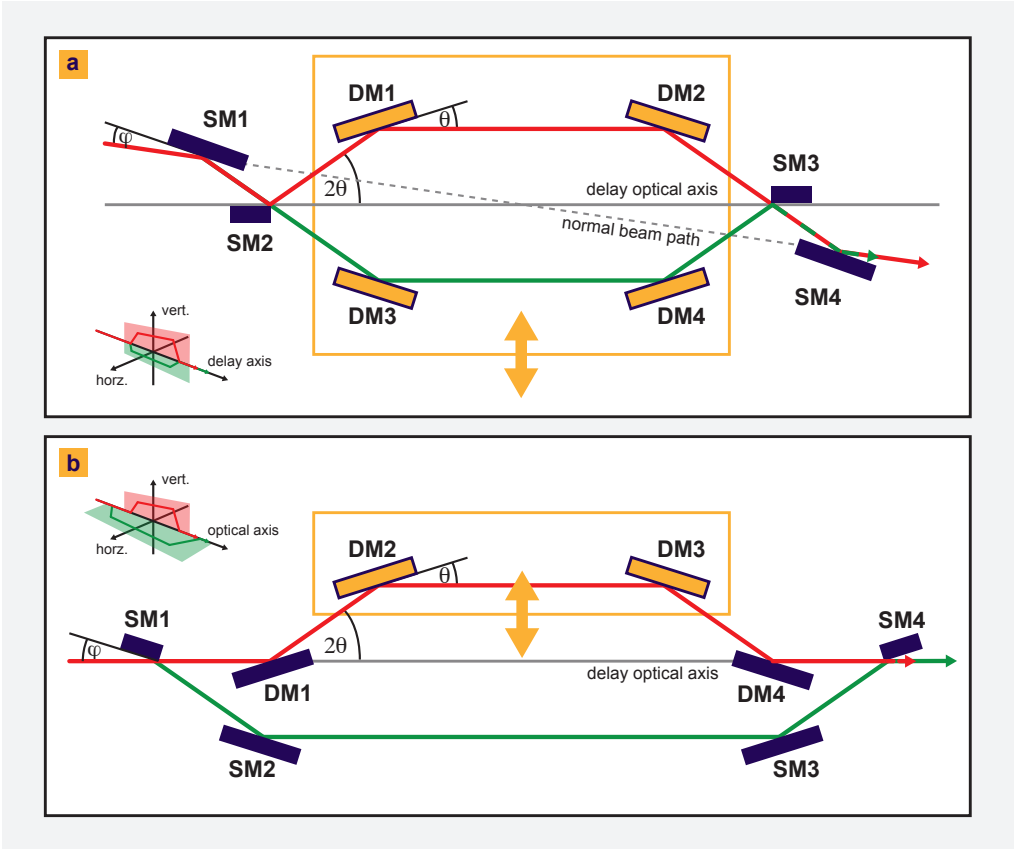

Figure 3.20: Possible schemes to implement a soft X-ray split and delay device at SASE3/SCS (SQS): (a) Wavefront division beam splitter with grazing incidence Mach-Zehnder interferometer [47]. (b) Wavefront division beam splitter with asymmetric geometry using a fixed and a variable delay in different mirror planes [31]. SM and DM indicate mirrors responsible for the split and delay of beams, respectively

Before describing the conceptual design of a soft X-ray beam split and delay (XBSD) line for the European XFEL, we briefly review the requirements that have been listed in [28]:

Requirements for the XBSD line

- Soft X-ray delay line with at least 10 ps delays extending as far as possible into the picosecond time scale
- Asymmetric mirror arrangements to achieve the largest delay range
- Photon energy range must include 3d transition L edges
- High transmission of the XBSD device
- Wavelength control for the individual pulses
- Spatial separation of the two beams behind the sample for individual detection
- Evaluation of alternatives, such as grating-based splitters and multilayer coatings

For the X-ray delay stage, a path length difference Δ of 0.3 mm per picosecond has to be achieved. When considering B_4C-coated mirrors, an incidence angle θ can be chosen in the range of 10–20 mrad without significant loss of transmission below 1.5 keV (Figure 3.2 on page 33). The length of the delay stage along the optical beam path is approximately given by $L_{\text{delay stage}} \simeq \Delta/2\theta^2$. This yields a 3.75–15 m device length with a 10 ps delay range for 20–10 mrad incidence angles, respectively.

A device of such length requires the motion of each delay mirror on a long high-precision axis. It is desirable to keep the concept of the XBSD line as simple as possible. Therefore, the commissioning of the device parameter space to stabilize the beam path over the scannable delay range will be as effortless as possible and, therefore, rather independent of the photon energy by avoiding multilayer coatings for the mirrors. In addition, the variable delay should be controlled by involving a minimum set of mirrors. These requirements would favour a setup similar to Mitzner et al. [31], which further has the advantage of having only four optical elements per delay branch. The asymmetric arrangement of fixed and variable delays allows for

placing the zero delay length of the two beams near the beginning of the variable delay range.

A suitable location of the XBSD line is between the grating tank of the monochromator and the distribution mirrors M5 and M6.

This concept has several key advantages:

- XBSD can be used by all three beamlines of SASE3
- Monochromator can be integrated as a beam splitter using zeroth- and first-order beams of the grating
- Zeroth-order beam can be used as an X-ray pump pulse and conceptually integrates the self-seeding schemes generating ultrashort, longitudinally coherent, and nearly transform-limited pulses
- Recombination of the two beams onto the vertical exit slit can be designed such that the wavelength of the individual beams can be controlled

The operation modes listed in Table 3.5 may be realized and are conceptually discussed in the following section.

Table 3.5: Possible operation modes of the XBSD line by combining the soft X-ray monochromator gratings G1, G2, and M4 with either the zeroth-order reflecting mirror (ZOM) or the wavefront beam splitter (BS). λ_1 and λ_2 indicate different wavelength selection of the two beams.

Operation mode	**X-ray pump**	**X-ray probe**
G1/G2 & ZOM	Zeroth-order of G1/G2, self-seeded	First-order G1/G 2 at λ_1
G1/G2 & BS	First-order G1/2 at λ_1	First-order G1/2 at λ_1
G1/G2 & BS	First-order G1/2 at λ_1	First-order G1/2 at λ_2
M4 & BS	Pink beam (zeroth order), self-seeded	Pink beam (zeroth order), self-seeded

3.6.1 Conceptual design

The SCS conceptual design of the XBSD device, which represents a retractable nested beamline, is shown in Figure 3.21. The corresponding mirror positions, optical length, and proposed incident angles are given in Table 3.6 on the facing page. The mirrors of the fixed and variable delays of the XBSD device operate in the vertical and horizontal planes, respectively, for two reasons: (1) The X-ray pump pulse propagates along the fixed delay line. Taking advantage of the beam splitter properties of the grating, the zeroth-order beam can be used to pump the sample with a longitudinally coherent pulse when self-seeding the SASE3 becomes available. Therefore, the fixed delay line mirrors operate in the vertical plane. (2) The variable delay line mirrors can technically be better controlled and translated by installing the mirrors on a horizontal stage.

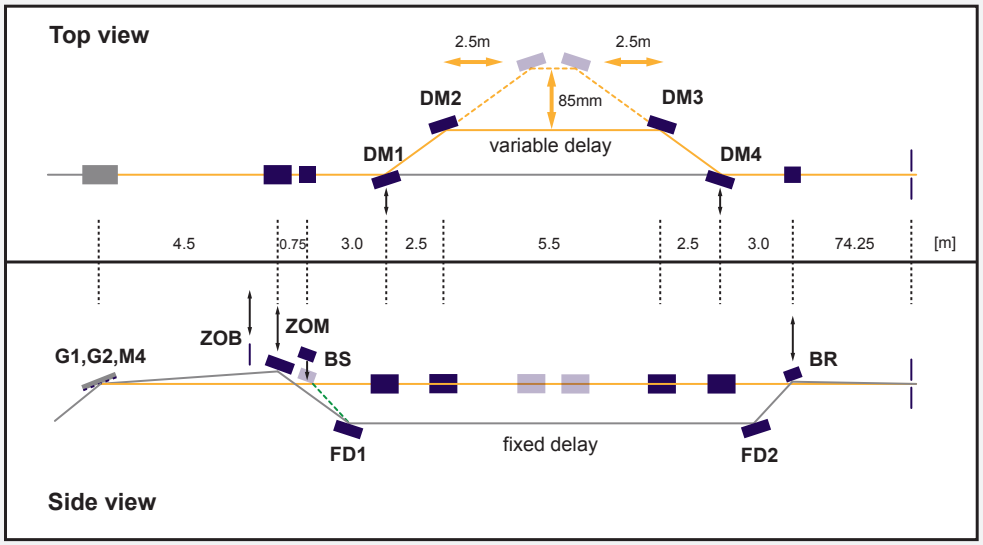

Figure 3.21: Proposed scheme for the XBSD line integrated into the soft X-ray monochromator. The mirrors DM and FM form the variable delay and fixed delay line path, respectively. The illustration shows the beam split operation using the gratings G1, G2 or M4 and the zeroth-order reflecting mirror (ZOM). The zeroth-order beam stop (ZOB) is inserted when the XBSD devise operates with the wavefront beam splitter (BS).

Table 3.6: Proposed mirror location relative to the monochromator grating, their optical length, and their incident angles

Mirror	Description	Distance to grating [m]	Length [mm]	Incident angle [mrad] (0.4–1.2 keV)
ZOS	Zeroth-order stopper	4.0	≥ 650 mm	19–21
ZOM	Zeroth-order mirror	4.5	≥ 650 mm	19–21
BS	First-order beam splitter	5.25	300 mm	20-30
FD1	Fixed delay start	8.25	650 mm	20-30
DM1	Variable delay start	9.25	400 mm	20-30
DM2	Moving delay	11.75–14.00	400 mm	20-30
DM3	Moving delay	14.50–17.00	400 mm	20-30
DM4	Variable delay end	19.5	400 mm	20-30
FD2	Fixed delay end	20.5	650 mm	20-30
BR	Beam recombination	23.5	≥ 300 mm	19–30

3.6.2 Beam splitting

The beam splitting can be performed in two ways: (1) The grating can be used as a beam splitter. The zeroth order and first order are separated by 2–4 mrad, depending on the photon energy (0.45–1.2 keV). The zeroth-order stopper (ZOS) can be removed and the zeroth-order mirror (ZOM) deflects the beam into the fixed delay line. (2) The beam splitter (BS) mirror is inserted, redirecting a variable portion of the beam into the fixed delay line. The position of the BS is approximately where the ZOM-deflected beam crosses the normal beam path of the monochromator. This minimizes vertical movements of the mirrors FD1 and FD2 in the fixed delay line for the two different operation modes. Table 3.5 on page 61 summarizes the possible operation modes of the XBSD device.

3.6.3 Variable delay line

The variable delay line is inserted by moving the mirrors DM1 and DM4 into the normal beam path. The relative delay time between the fixed and variable delay line is changed by moving the mirrors DM2 and DM3. It has to be further investigated whether this motion should be done by one or two motor axes. The delay range depends on the incident angle θ and can be designed to be adjustable. For this reason, it may be advantageous to have independent motion control of the delay mirrors, one along and one orthogonal to the delay axis as indicated in Figure 3.21 on page 62. This would allow for extending the delay significantly into the picosecond time range at the cost of significantly lower beam transmission of the mirrors (Figure 3.2 on page 33). In the case of XPCS experiments where long delay ranges may be required, this loss in photon numbers could be compensated by choosing a smaller focus on the sample and, thereby, further increasing the speckle size in the diffraction patterns. In the case of NLXS experiments, shorter delays with high transmission of the delay lines may be sufficient. Table 3.7 gives potential time delay ranges for different incident angles.

Table 3.7: Possible time delay range of the XBSD line for different incident angles

Time delay range [ps]	Incident angle θ [mrad]	Transmission
-0.7 – +2.6	10	0.8
-2.6 – +10.6	20	0.5 below 1.5 keV and $\ll$ 0.1 above 1.5 keV
-6.0 – +24.0	30	$\sim$ 0.1 below 1.5 keV
-11 – +42	40	$<$ 0.1 below 1.5 keV

3.6.4 Beam recombination

The BR mirror recombines the beams of the two delay lines. Since the mirror deflects the beam of the fixed delay line in the dispersion plane of the grating, different wavelengths can be selected in the second operation mode (BS is inserted in first order of the grating) by varying the beam position on the vertical exit slit. The two beams will be collinear in the vertical plane because of the ~ 80 m distant and narrow exit slit. The horizontal plane could be used to produce a small angle between the two beams that will overlap at the exit slit and the sample. This would allow for separate detection of the pump and probe beams behind the sample. For this scheme, the horizontal KB mirror aperture has to be large enough to capture both beams and to refocus them on the sample.

4 SCS photon beam properties

This chapter summarizes the X-ray photon beam properties at the sample interaction point of the SCS instrument. The SASE3 source parameters and the SCS X-ray beam transport system and components have been described in Chapter 2, “SASE3 photon beam properties”, and Chapter 3, “X-ray optical layout”, respectively. The requirements of X-ray photon beam at the sample position depend strongly on the X-ray techniques. We proposed typical parameters for the SASE3 and SCS beamline operations that emphasize the particular needs of the experiments as described in Chapter 1, “Scope of the SCS instrument”. The X-ray photon beam parameters or operation modes differ in terms of maximizing the number of photons, shortest pulses, and spectral bandwidth, as well as maximizing or minimizing the photon flux. The operation modes and beamline settings are listed in Table 4.1 on the next page.

The listed parameters have been used to predict the expected number of photons per pulse, peak and average intensities, and pulse-integrated fluence in the corresponding figures 4.1–4.7. The baseline SASE3 operation of 14 GeV has been assumed for most of the X-ray techniques.

The soft X-ray monochromator entrance and exit slit settings have been adjusted to the SASE3 pulse length (1 nC or 100 fs, 0.2 nC or 20 fs, 0.06 nC or 5 fs) to account for pulse stretching (see Section 3.4.4, “Short-pulse preservation within the bandwidth–duration limits”) and focusing requirements. Note that, in case of high-resolution RIXS, the pulse length is dominated by the minimum spectral bandwidth–duration product of the monochromator and that reducing the bunch charge to produce shorter pulses has essentially no effect. For Figure 4.4 on page 71, Figure 4.6 on page 73, and Figure 4.7 on page 74, the nominal focus size of the KB refocusing optics is used (see Section 3.5, “KB refocusing optics”). The average intensity is calculated based on the maximum repetition rate of the European XFEL, i.e. 27 000 pulses per second (Figure 8.2 on page 121).

Table 4.1: Operation modes of the SCS instrument with proposed beamline parameters that reflect the emphasis of individual techniques

Operation mode	Electron energy [GeV]	Bunch charge [nC]	Mono operation	Entrance [mm] / exit [µm] slits	Sample focus [µm^2]
TR-spectrocopy,	14	1 (100 fs)	G1	50 / 20	100 x 100
TR-diffraction,	14	0.2 (20 fs)	G1	6 / 60	100 x 100
TR-PES (Fig. 4.1)	14	0.06 (5 fs)	G1	3 / 200	100 x 100
TR-RIXS	14	1 (100 fs)	G1	50 / 20	1000 x 10
(Fig. 4.2)	14	0.2 (20 fs)	G1	6 / 20	1000 x 10
	14	0.06 (5 fs)	G1	3 / 20	1000 x 10
HR-RIXS	14	1 (100 fs)	G2	50 / 20	1000 x 10
(Fig. 4.3)	14	0.2 (20 fs)	G2	6 / 20	1000 x 10
	14	0.06 (5 fs)	G2	3 / 20	1000 x 10
Mono CXDI	14	1 (100 fs)	G1	50 / 20	< 2 x 2
on small targets,	14	0.2 (20 fs)	G1	6 / 20	< 2 x 2
NLXS (Fig. 4.4)	14	0.06 (5 fs)	G1	3 / 20	< 2 x 2
Mono CXDI	14	1 (100 fs)	G1	50 / 20	10 x 10
on larger targets,	14	0.2 (20 fs)	G1	6 / 60	10 x 10
(Fig. 4.5)	14	0.06 (5 fs)	G1	3 / 200	10 x 10
Pink CXDI	17.5	1 (100 fs)	Pink (M4)	Open	< 2 x 2
with intermediate	17.5	0.2 (20 fs)	Pink (M4)	Open	< 2 x 2
focii (Fig. 4.6)	17.5	0.06 (5 fs)	Pink (M4)	Open	< 2 x 2
Pink CXDI	17.5	1 (100 fs)	Pink	Open	< 1 x 1
(Fig. 4.7)	17.5	0.2 (20 fs)	Pink	Open	< 1 x 1
	17.5	0.06 (5 fs)	Pink	Open	< 1 x 1

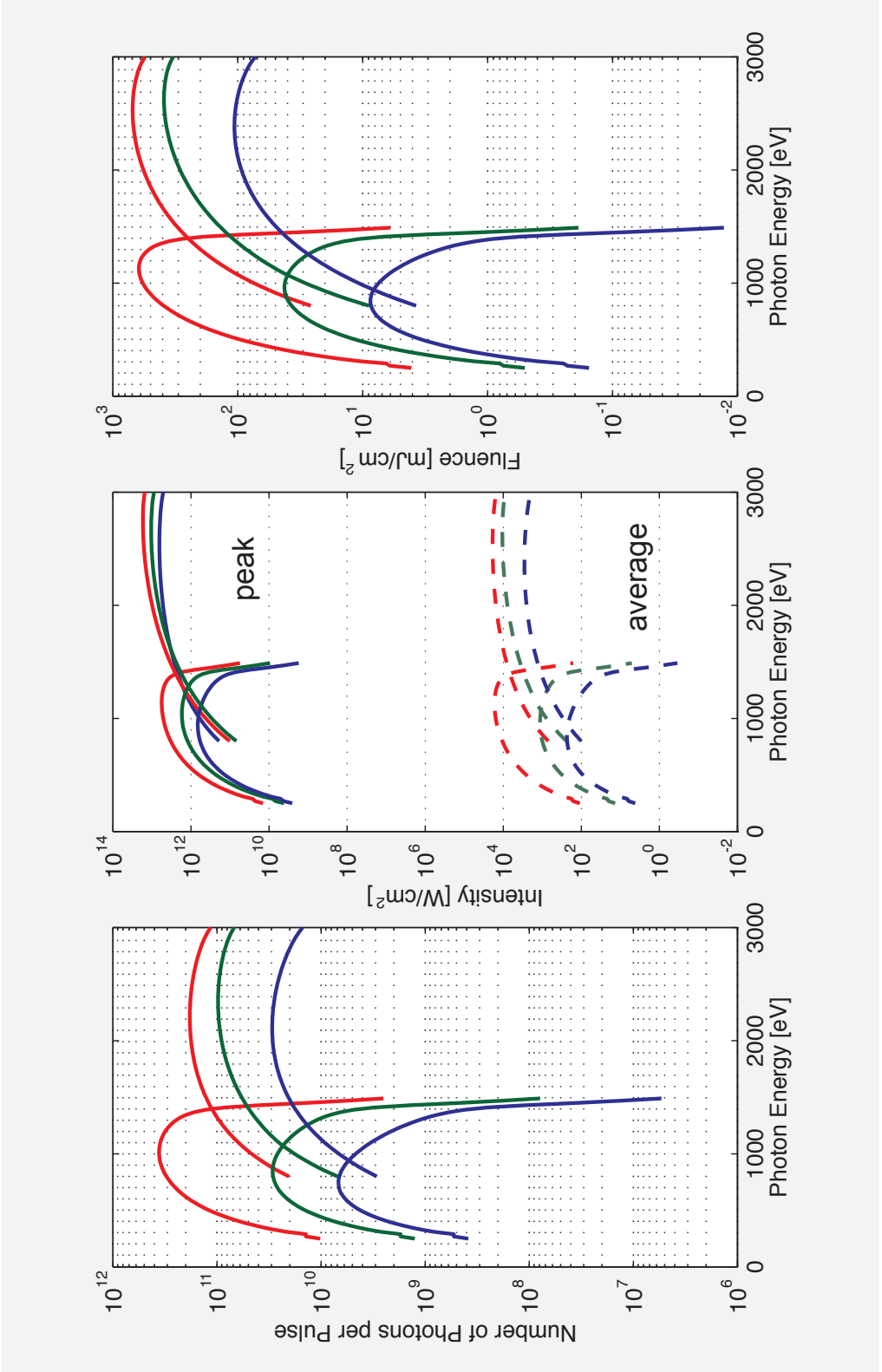

Figure 4.1: Photon beam properties for time-resolved spectroscopy and diffraction using the G1 grating. The number of photons, intensity, and fluence are calculated based on the parameters listed in Table 4.1 on the previous page and the following bunch charge: (red) 1 nC or 100 fs, (green) 0.2 nC or 20 fs, and (blue) 0.06 nC or 5 fs pulse duration.

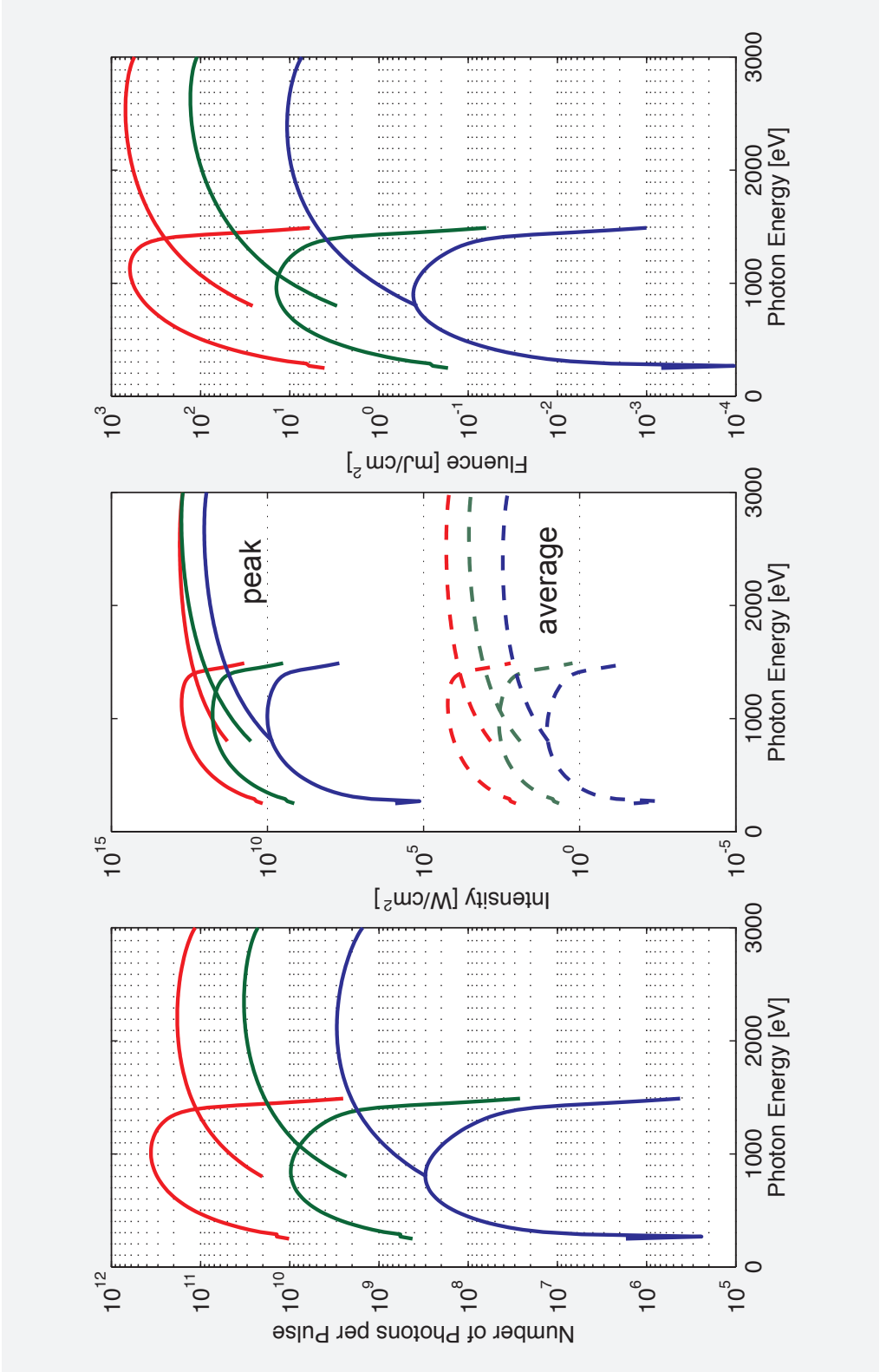

Figure 4.2: Photon beam properties for time-resolved RIXS using the G1 grating. The number of photons, intensity, and fluence are calculated based on the parameters listed in Table 4.1 on page 67 and the following bunch charge: (red) 1 nC or 100 fs, (green) 0.2 nC or 20 fs, and (blue) 0.06 nC or 5 fs pulse duration.

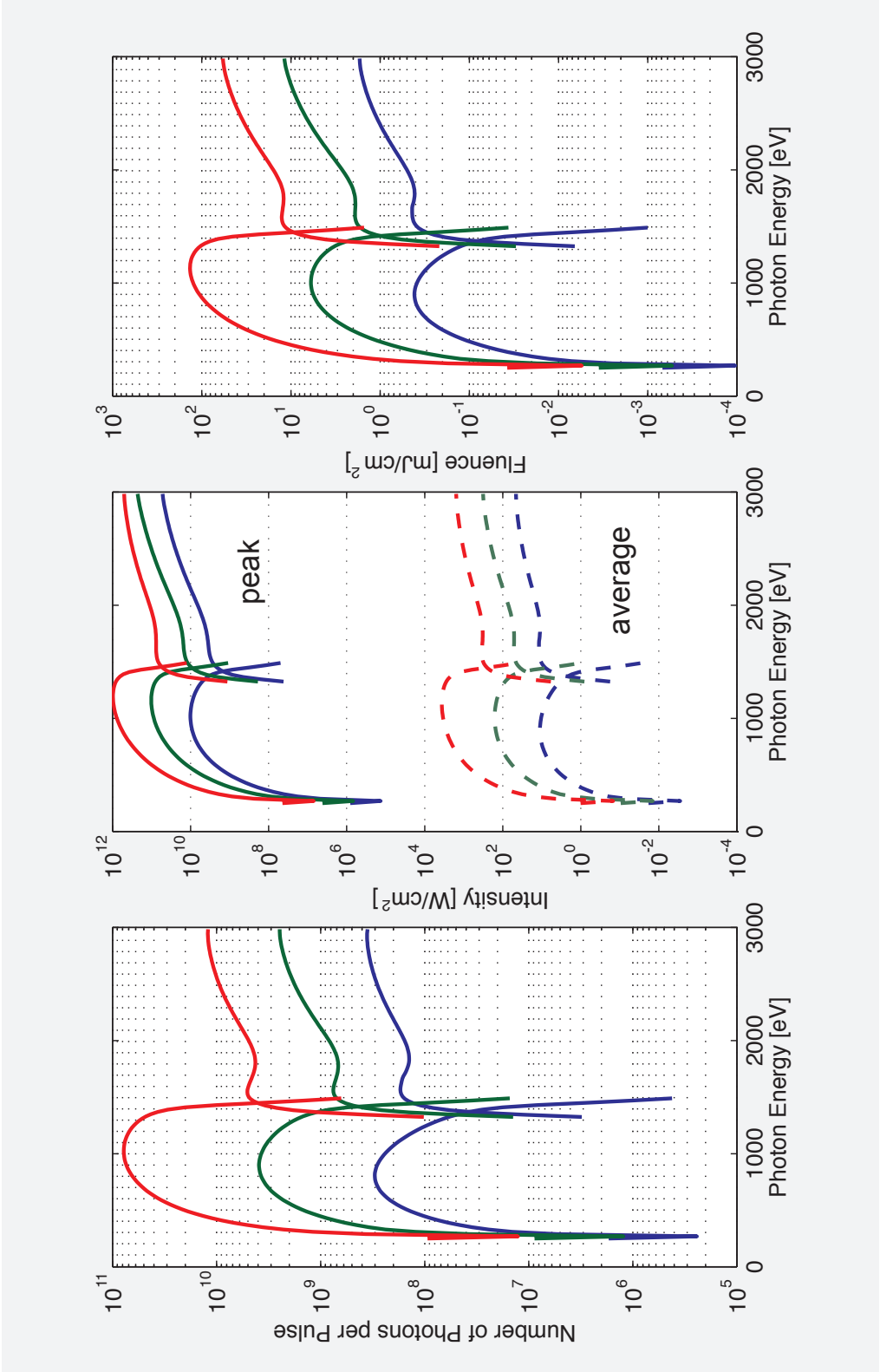

Figure 4.3: Photon beam properties for high-resolution RIXS using the G2 grating. The number of photons, intensity, and fluence are calculated based on the parameters listed in Table 4.1 on page 67 and the following bunch charge: (red) 1 nC or 100 fs, (green) 0.2 nC or 20 fs, and (blue) 0.06 nC or 5 fs pulse duration.

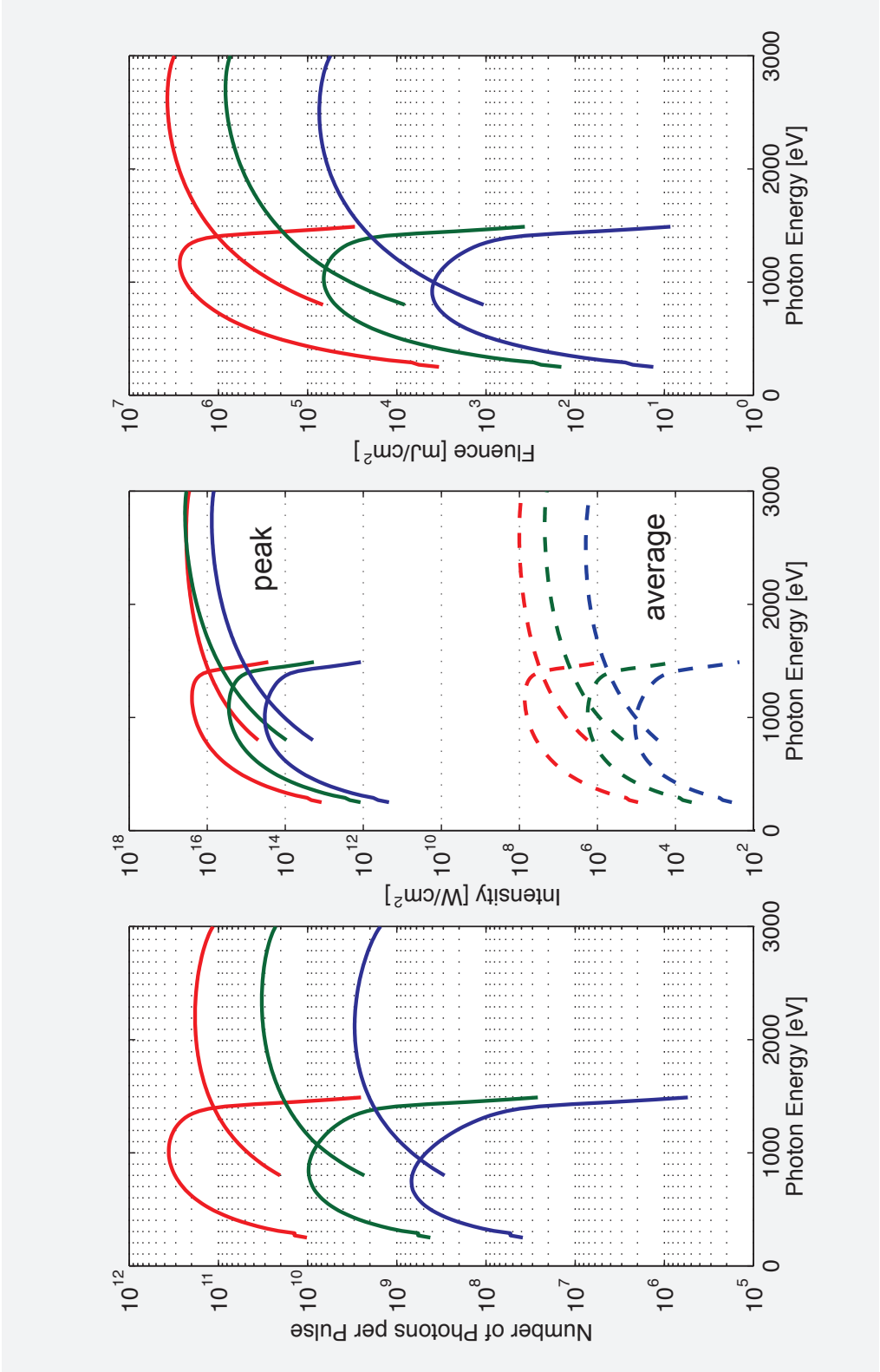

Figure 4.4: Photon beam properties for resonant CXDI on small targets ($\lesssim$ 1 µm). The number of photons, intensity, and fluence are calculated based on the parameters listed in Table 4.1 on page 67 and the following bunch charge: (red) 1 nC or 100 fs, (green) 0.2 nC or 20 fs, and (blue) 0.06 nC or 5 fs pulse duration.

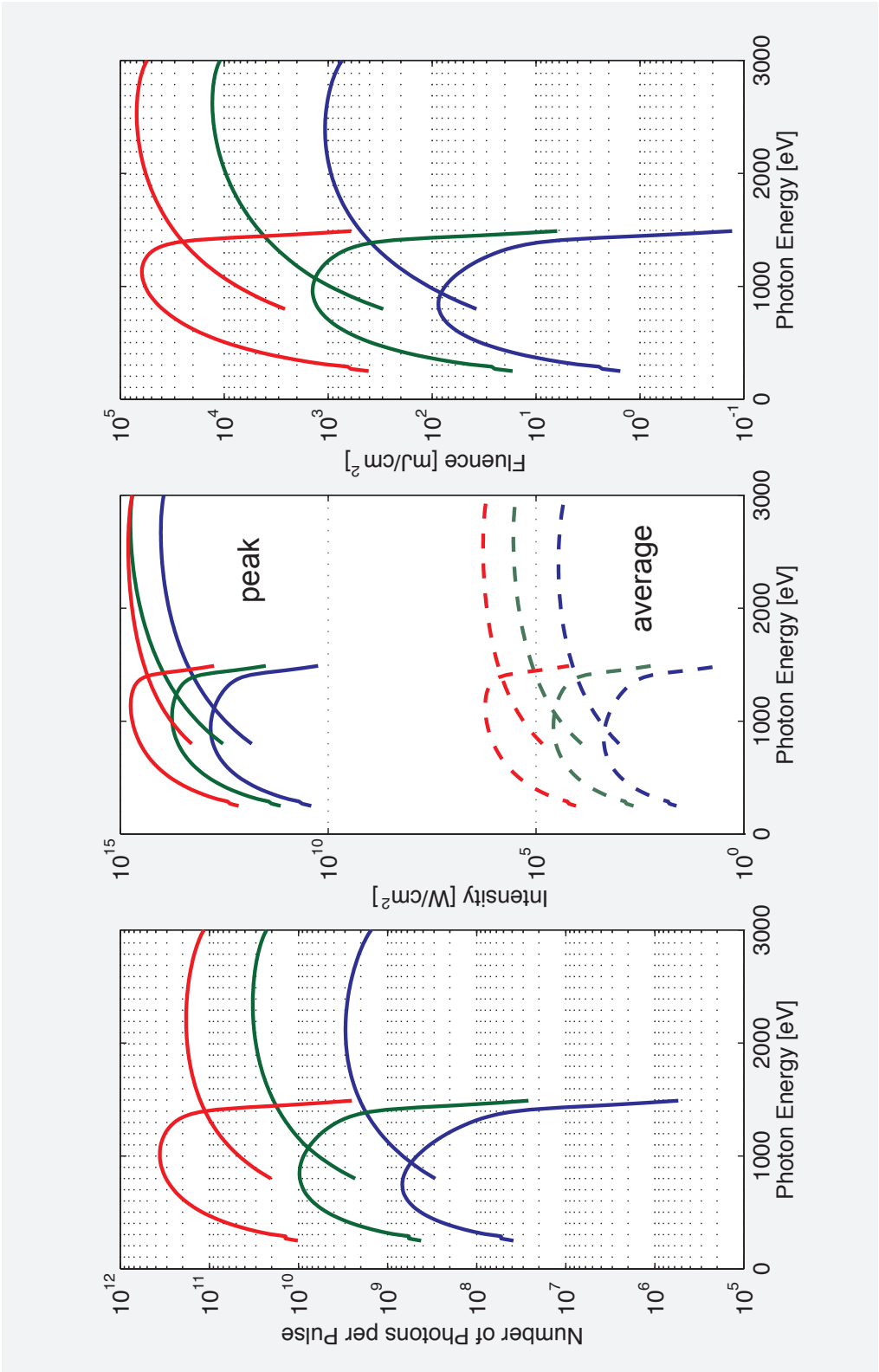

Figure 4.5: Photon beam properties for resonant CXDI on larger targets (< 5 µm). The number of photons, intensity, and fluence are calculated based on the parameters listed in Table 4.1 on page 67 and the following bunch charge: (red) 1 nC or 100 fs, (green) 0.2 nC or 20 fs, and (blue) 0.06 nC or 5 fs pulse duration.

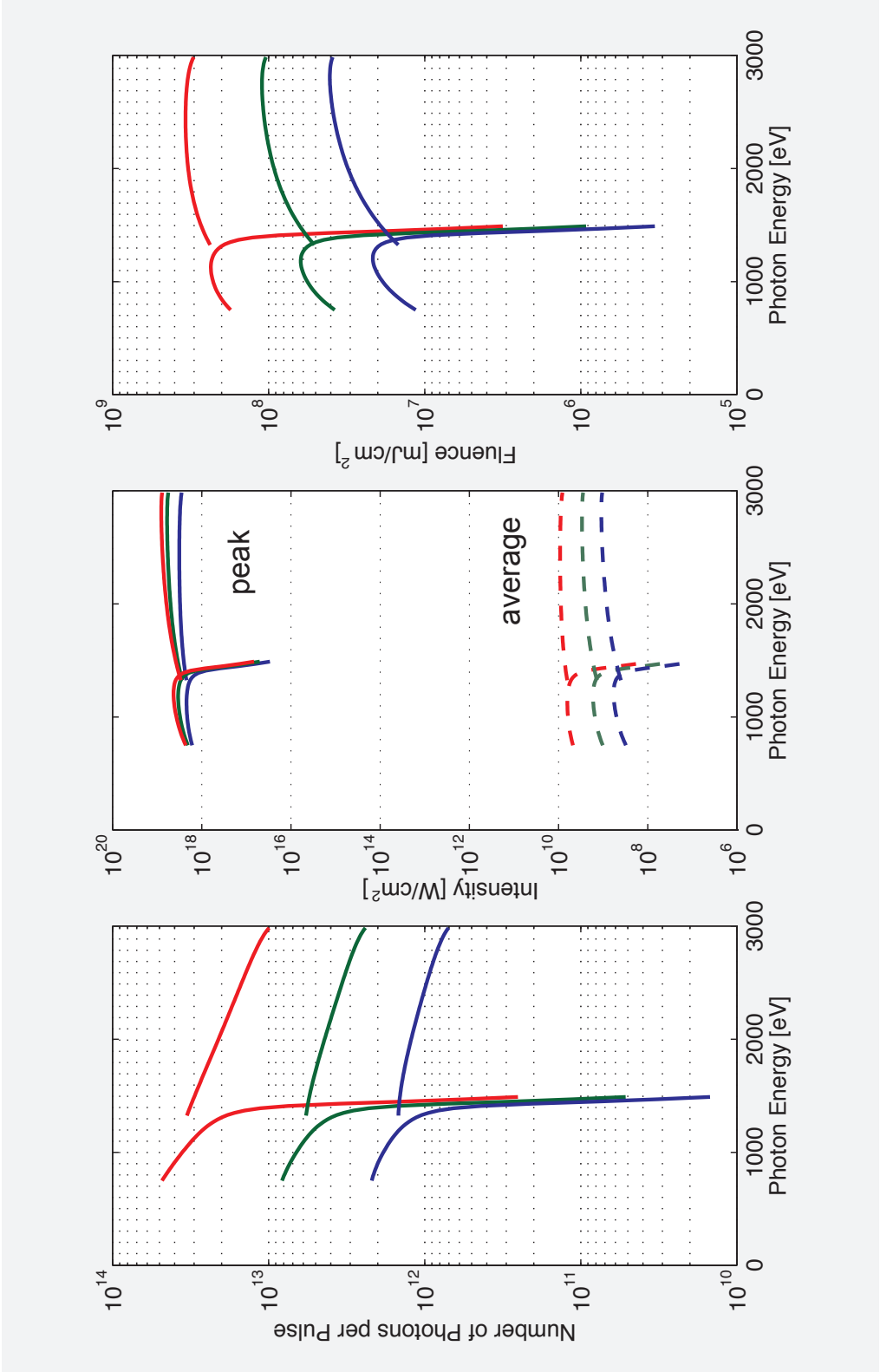

Figure 4.6: Photon beam properties for CXDI on small targets ($\lesssim$ 1 µm) using pink beam and intermediate focus. The number of photons, intensity, and fluence are calculated based on the parameters listed in Table 4.1 on page 67 and the following bunch charge: (red) 1 nC or 100 fs, (green) 0.2 nC or 20 fs, and (blue) 0.06 nC or 5 fs pulse duration.

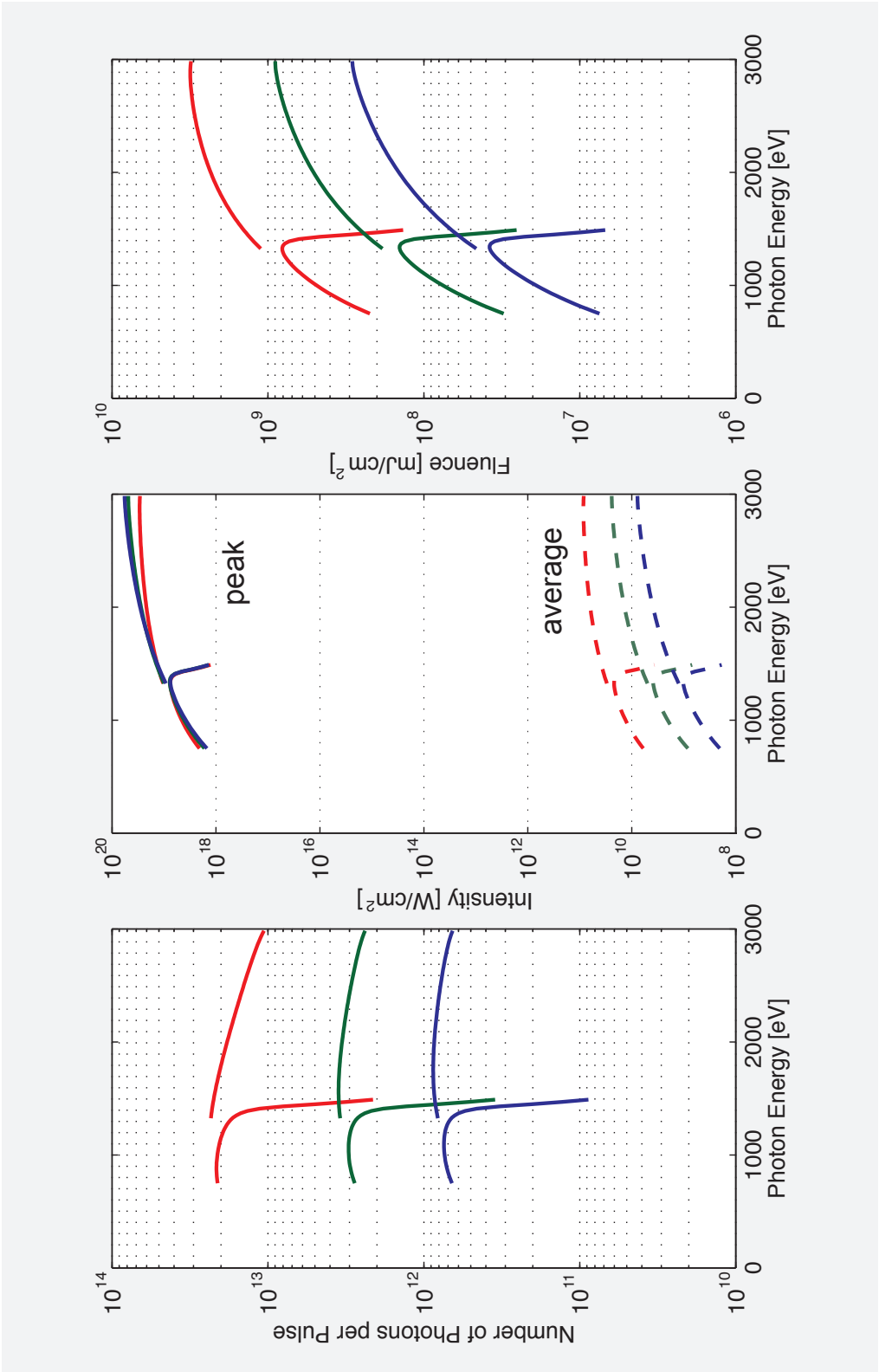

Figure 4.7: Photon beam properties for CXDI on small targets ($\lesssim$ 1 µm) using pink beam without intermediate focus. The number of photons, intensity, and fluence are calculated based on the parameters listed in Table 4.1 on page 67 and the following bunch charge: (red) 1 nC or 100 fs, (green) 0.2 nC or 20 fs, and (blue) 0.06 nC or 5 fs pulse duration.

5 SCS hutch infrastructure and experiment setups

This chapter describes the SASE3 area in the experiment hall, followed by the envisioned experiment setups for the various techniques in the SCS hutch and the conceptual design of the experiment chamber. The complex sample environment is broken down into potential assemblies that will provide temperature and magnetic field controls. It is clear that these assemblies are subject to different constraints in terms of sample manipulation, which will partly exclude each other. The technical design and how the various sample environments can be combined are the subject of further development.

5.1 Hutch layout

Figure 5.2 on page 80 shows the SASE3 area in the experiment hall. The SASE3 area has three ports: two of them are for the baseline instruments SCS and SQS, while the third port is open. It is currently being discussed whether the third port is a suitable location for PES experiments. At this stage of the SCS conceptual design, it is too early to make any integration planning from the side of the SCS group. The SCS operation area comprises the experiment hutch (SCS.EXP, area = 137 m^2), the SCS laser hutch (SCS.LAS, area = 34 m^2), the SCS control room (SCS.CTR, area = 38 m^2), and the SCS rack gallery (SCS.RCK, area = 34 m^2), which is located on top of the SCS.EXP hutch for space reasons and hosts up to 15 racks. Access to the rack gallery is provided through the higher-level gallery that goes around the experiment hall.

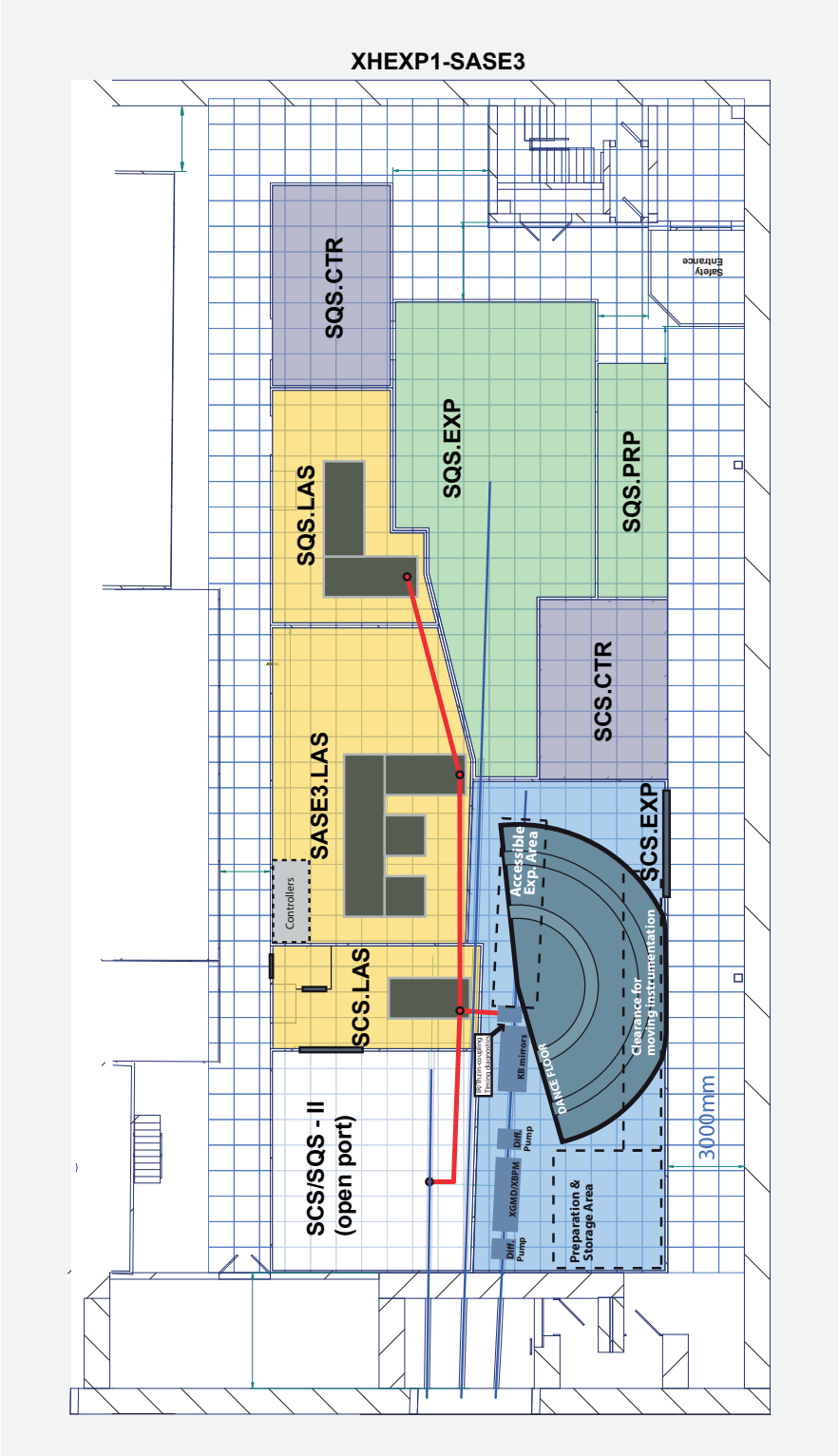

Figure 5.1: Experiment hall floor plan of the SASE3 area. The dimension of the blue background grid is 1 m.

5.1.1 SCS experiment hutch (SCS.EXP)

The current integration plan for the SCS experiment hutch, SCS.EXP, considers instrumentation related to photon-in/photon-out spectroscopy and coherent scattering techniques. It should be noted that the instrumentation is not restricted to these techniques, and that PES experiments could be integrated as well with the caveat that space for preparation and storage in the SCS.EXP area is already very limited. To enable different experiment setups at SCS, it is necessary to swap large instrumentation. Conceptually, this swapping is possible; technically, however, it is more demanding—in terms of parallel integration of the instrumentation and the time required to set it up—than having a single end station and detector. Therefore, spatial constraints require keeping the minimum of key instrumentation and designing a setup that is as modular as possible. This is discussed in more detailed in Section 5.3, “Experiment setups”.

The SCS.EXP area will be equipped with a crane that covers the largest area of the hutch interior to change instrumentation. The experiment area can be accessed from the outside on the floor through a wide sliding or roll-up door and by means of the hall crane through the ceiling of the SCS.EXP hutch in the area between the accessible experiment area and the entrance point (Figure 5.1 on the preceding page). The floor of SCS.EXP has specific requirements for the RIXS spectrometer in the area indicated as the “dance floor”. In this area, heavy and large-scale instrumentation will be moved on air pads. It has to be further investigated with the hRIXS UC whether the envisioned pentrasil floor will meet the requirements after hardening by wet treatment and polishing to 1 mm/10 m. Alternative solutions used at the Swiss Light Source (SLS) at Paul Scherrer Institute (PSI) in Villigen are granite tiles on top of the hall floor, which could create potential difficulties in swapping experiment setups. SCS.EXP contains an area that allows for storing and preparing (during SCS offline mode) modules of the SCS instrument that are not in use.

5.1.2 SCS laser hutch (SCS.LAS)

From the SASE3 laser room (SASE3.LAS), which is operated and maintained by the Optical Lasers group (WP76), the optical laser beam is delivered either to the SCS or SQS laser hutch. In the current laser operation scheme, a simultaneous operation for the two instruments is not possible. The SCS laser hutch, SCS.LAS, allows for the up- or down-conversion of the fundamental frequencies. From SCS.LAS, the beam is finally distributed to the optical laser in-coupling in the SCS.EXP hutch or the open-port hutch. The separate SCS.LAS hutch provides access for laser work while

the SCS.EXP hutch is in operation mode. Further details can be found in Chapter 8, “Optical laser delivery”.

5.1.3 SCS control room (SCS.CTR)

The SCS control room, SCS.CTR, provides the minimum space for controlling and running the experiment, as well as online analysis to steer the experimental run.

The room will host computer pools and big overhead screens for the following areas:

- Beamline and diagnostics controls
- Instrument controls
- Detector controls
- DAQ controls
- Optical laser and timing controls
- Online analysis (1)
- Online analysis (2)

5.1.4 SCS rack gallery (SCS.RCK)

The SCS rack gallery, SCS.RCK, is located on top of the SCS experiment hutch. The cables are routed to the instrumentation and detectors directly above the sample interaction point in the ceiling of the experiment area. As the detectors have a rotational degree of freedom around the sample interaction point, this appears to be the best option for the interface in order to keep cable length as short as possible.

5.2 Permanent beamline components and diagnostics

The first component in the experiment hutch is the intensity and beam position monitor for recording the monochromatic-beam intensity, which shows only a small correlation to the pink-beam intensity measured further upstream behind the SASE3 gas attenuator. The device has been located on the experiment hall floor because the tunnel and experiment hall rest on different fundaments. The beam position monitor can detect small beam drifts on long time scales and potentially feedback to the KB refocusing mirrors. Details can be found in Section 7.1, “Intensity monitor”, and Section 7.2, “Beam position monitor”. The X-ray gas monitor (XGMD) / X-ray beam position monitor (XBPM) device that is enclosed by differential pumping sections is followed downstream by the KB refocusing mirrors. In between the KB mirrors and the

sample interaction point is the laser in-coupling with a differential pumping section (see Section 8.4, “Laser in-coupling with differential pumping section”) that includes the upstream parasitic X-ray optical pulse timing diagnostics (see Section 7.4, “X-ray–optical pulse timing diagnostics”) and, optionally, a thin-fim X-ray attenuator chamber (see Section 7.5, “Thin-film X-ray attenuator chamber”). The permanently installed beamline components are separated by the SCS beamline closing valve. The various end stations will be connected to the beamline valve via a bellow/spooling piece that can be individually pumped and short-baked to maintain high vacuum conditions on both ends of the instrumentations. The beam monitor chamber (BMC) is located downstream at the end of the experiment hutch and includes a B_4C beam stop and a set of photodiodes with different coatings and respective attenuation levels.

5.3 Experiment setups

Figure 5.2 on the following page shows the conceptual experiment setups a)–d) that will be sequentially integrated during the transition from SCS commissioning to user operation mode. The main instrument components include a forward-scattering fixed-target (FFT) chamber, a back-scattering fixed-target (BFT) chamber (add-on chamber by hRIXS UC), modules with array detectors (DSSC, FastCCD), and the hRIXS spectrometer. A liquid-jet chamber is also envisioned as a contribution to the SCS instrumentation from the hRIXS UC. This liquid-jet system may be used in all experiment geometries. The FFT and BFT systems will thus be considered here as a placeholder for this system. The key for allowing modular setups is the technical design of their interfaces.

A sequential integration plan could look like the following:

1 Integration of FFT and array detectors for time-resolved small-angle diffraction and single-shot imaging (CXDI), i.e. SCS baseline instrumentation, as the startup configuration in early 2016.

2 Integration of BFT and hRIXS spectrometer for time-resolved and high-resolution RIXS, i.e. the add-on hRIXS UC instrumentation

3 Integration of BFT and array detectors for REXS

4 Integration of XBSD line (see Section 3.6, “X-ray beam split and delay line”) for XPCS in forward- and back-scattering geometry

5 Integration of FFT and hRIXS spectrometer for NLXS, such as impulsive stimulated X-ray Raman spectroscopy

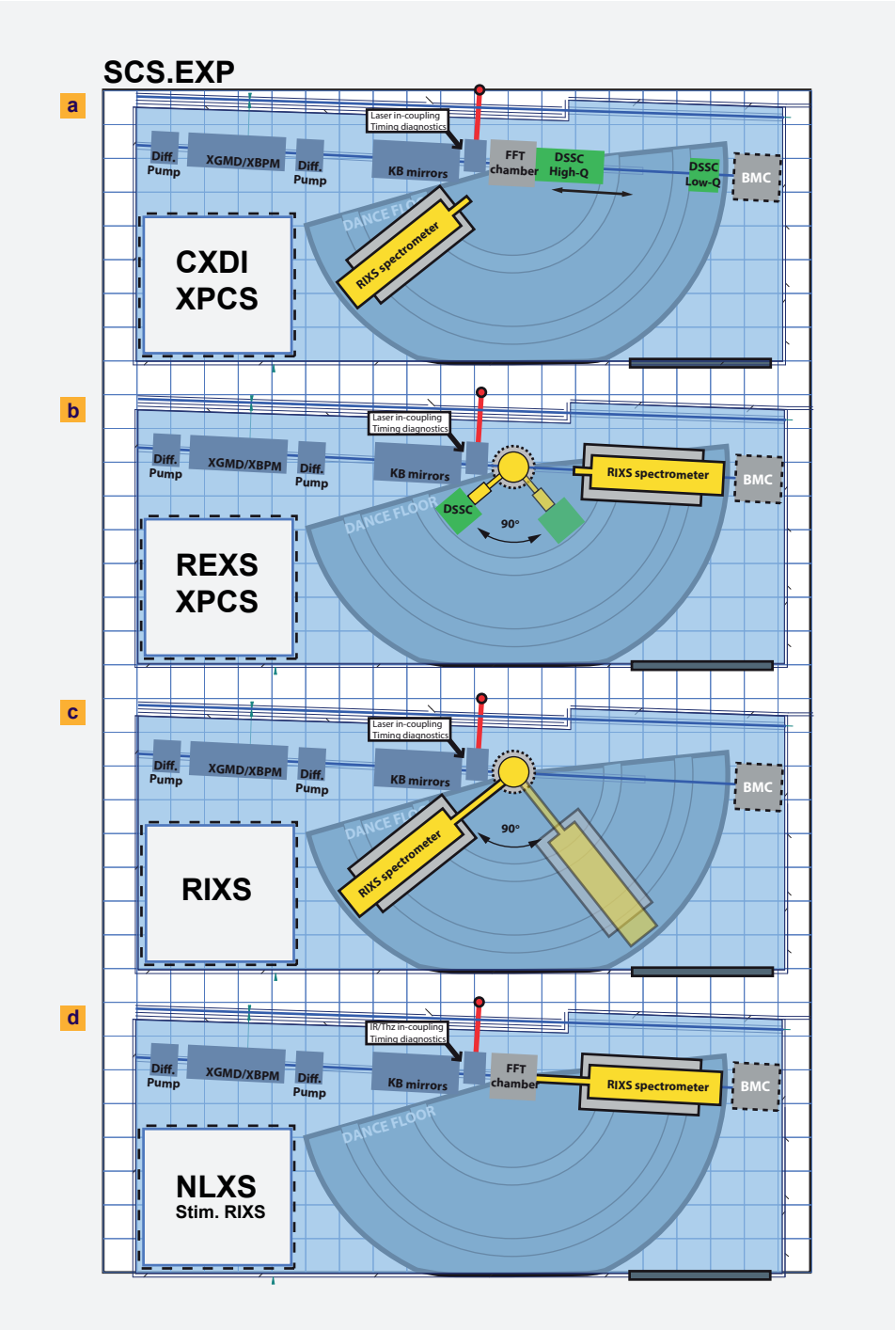

Figure 5.2: Experiment setups in the SCS hutch: a) Forward-scattering geometry for CXDI, time-resolved SAXS, and XPCS. b) Back-scattering geometry for REXS and CXDI in reflection. c) RIXS experiment setup. d) NLXS experiment setup (e.g. stimulated RIXS). The dimension of the blue background grid is 1 m.

The sequential integration of the experiment setups will realistically add up to one year as a coarse time estimate, divided into periods of commissioning and user time on integrated components.

5.4 FFT chamber

The forward-scattering fixed-target (FFT) chamber will serve forward-scattering geometries on fixed targets. This includes time-resolved small-angle diffraction and coherent X-ray diffraction imaging as well as nonlinear X-ray spectroscopy. A schematic side view of the system is shown in Figure 5.3.

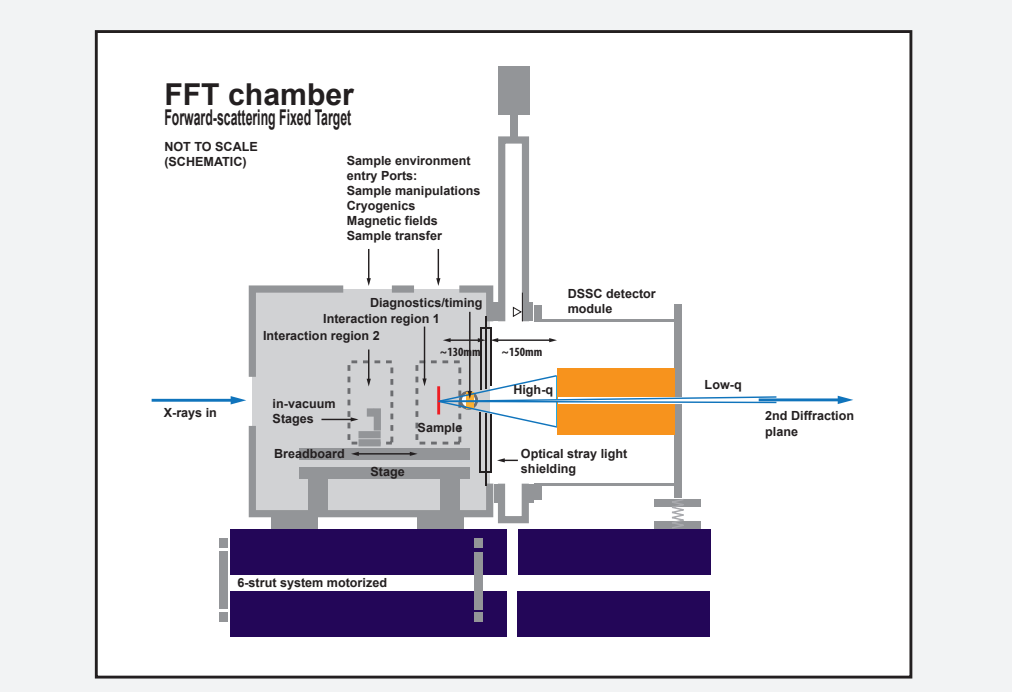

Figure 5.3: Conceptual design of the FFT chamber: The FFT chamber has a cubic shape and could provide space for two interaction regions with different sample environments or sample transfer. This configuration shows the FFT chamber with the DSSC module attached. The shortest sample–detector distance is approximately 280 mm (with gate valve) and 150 mm (without gate valve). The range of the sample–detector distance can be adjusted either by moving the detector (limited) or by moving the breadboard stage.

The shape of the system is cubic in order to accommodate the large-area DSSC detector and to minimize sample–detector distance. The dimension of the DSSC module is still open and could have a flange interface as large as DN800. Efforts are being made to decrease this dimension down to the limit of DN600. This will

determine the final height and width of the FFT chamber. The length of the FFT chamber will be on the order of 600 mm. This gives room for two sample interaction regions or a longer travel range along the beam direction to vary the sample–detector distance.

5.4.1 Interaction regions

As discussed in Section 5.6, “Sample environment and delivery”, the system could provide diverse sample environments for a broad range of applications. However, the space to bring sample environments like magnetic fields, low-temperature cryostats installed on manipulators, and sample transfer mechanism into the interaction region is limited. It is therefore advantageous to have two sample interaction regions.

Those could be used in different ways as, for example:

- Conveniently switching between two incompatible setups: for instance, one using out-of-vacuum sample manipulation and the other using in-vacuum sample manipulation
- Combining both interaction regions to one and extending the sample–detector distance range by ~ 100 mm
- Using one region for sample transfer or load lock if this is incompatible with the sample environment at the interaction point

5.4.2 Breadboard

The in-vacuum support for the sample environment is mounted on a breadboard that is positioned on a linear stage along the beam propagation direction. An *xyz* sample manipulation and optional add-on rotational degrees of freedom are planned based on in-vacuum stages from e.g. SmarAct or Nanomotion. A guard stage in front of the sample stage can be used to stop X-ray stray light from upstream optics, which could casts light shadows on the detector from, for instance, adjacent sample membranes. Additional stages for optical elements may be required for optical laser manipulation near the sample, such as THz generation.

5.4.3 Ports for additional sample environment

Access to the interaction region from the outside can be provided on three sides of the chamber. These ports can be used for magnetic fields and low-temperature sample environments or sample transfer to a load lock system.

5.4.4 Detector port

Small-sized samples act as point scatterers for optical radiation and will produce a bright background radiation in the FFT chamber. The detector port will have an installation to shield the detector from optical stray light as best as possible in optical pump, X-ray probe experiments. It will be investigated if the aperture of this shielding can be designed to be remotely adjustable. Additional optical filters on the DSSC detector are required for laser-induced dynamical studies.

5.4.5 Diagnostics

The FFT chamber will be equipped with an additional diagnostics stage, which is located between the Interaction Region 1 and the detector port and can be fully retracted. The diagnostics stage holds coarse timing diagnostics based on an antenna as well as a set of photodiodes with different coatings and thus X-ray attenuation levels.

5.5 hRIXS instrumentation of user consortium

The RIXS spectrometer is a proposed add-on instrumentation for the SCS instrument and will be provided by the hRIXS user consortium (UC). It can be rotated around the sample interaction point to vary the momentum transfer. The energy resolving power of the system (beamline and spectrometer) will be $\leq$ 10 000 and 30 000 below 1 keV matching the resolution given by the SASE3 soft X-ray monochromator gratings of 50 l/mm and 150 l/mm. The optical design is led by the group of Prof. Giacomo Ghiringhelli of Politecnico di Milano, Italy, a member of the hRIXS UC.

The requirements for the BFT chamber, which provides back-scattering geometries, are very similar to those for RIXS and REXS. This end station should provide ultrahigh-vacuum (UHV) conditions with, ideally, constantly variable detection angle. The hRIXS UC is planning for such a system for RIXS studies as add-on instrumentation, and it could also be employed for REXS studies. A prototype system

is presently being tested that would provide a 90° rotation of a flange on the outer diameter of a vacuum tank covering 60–150° angular range. The BFT chamber could interface with the RIXS spectrometer and the DSSC or FastCCD detector. In addition to the BFT chamber, a chamber is envisioned for liquid and gaseous sample environments.

A separate TDR for the hRIXS instrumentation will be prepared that will describe the integration of the components at the SCS instrument. At this time of the SCS CDR, it is too early to provide further details.

5.6 Sample environment and delivery

The sample environment and delivery discussed here is envisioned as common instrumentation for the FFT chamber and the add-on end stations, such as the BFT chamber, even though the requirements may differ at different levels. At this conceptual design stage, the options of sample environments are outlined for a further technical refinement in the SCS TDR. The development of the sample environment is done in collaboration with the Sample Environment group (WP79). The biggest challenges are spatial constraints given by the necessary degrees of freedom for sample manipulation, sample transfer, and the instrumentation for producing high magnetic fields and temperature control. An one-size-fits-all solution appears unrealistic at this stage, and experiment-specific requirements need refinement for guidance of the technical design. Here, further input is needed from the UCs and general users.

Requirements for the fixed-target sample environment

- Sample load lock and transfer system
- Precise temperature control: 2–2000 K
- Magnetic fields:
  - Pulsed high magnetic fields (several tens of Tesla)
  - Static high-field magnet (several Tesla)
  - Permanent-magnet options
- Forward- and back-scattering geometries with and without optical laser delivery
- Fast sample scanning capability for destructive sample probe

5.6.1 Fixed-target installation

5.6.1.1 Low-temperature goniometer sample holder

A low-temperature goniometer would be based on a liquid-helium flow cryostat providing sample temperatures in the range of 15 K to 400 K. The sample environment could be supplemented with exchangeable sample pucks and load lock as well as sample transfer systems. This sample environment is a potential solution for back-scattering geometries (Figure 5.4).

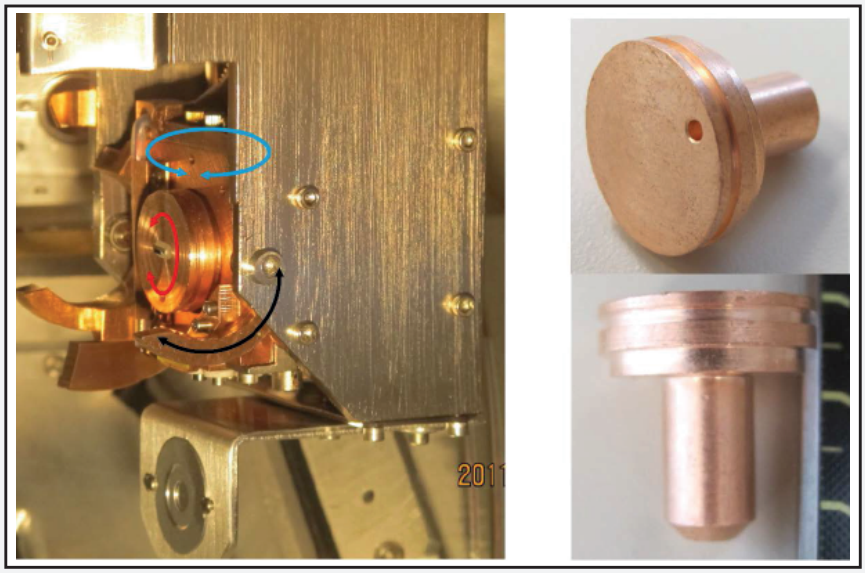

Figure 5.4: (a) Sample holder with liquid-helium flow cryostat combined with goniometer having three degrees of rotation and *xyz* linear motion. The temperature range is 15–400 K. (b) Exchangeable sample pucks.

5.6.1.2 Ultralow-temperature cryostat

An ultralow-temperature cryostat (T = 2–300 K) would be compatible with the high-field magnets that are described in Section 5.6.3, “Magnetic fields”. This sample environment can also be supplemented with a load lock and sample transfer systems. A simple design of the sample holder should allow for inserting the sample inside the constrained space of the high-field magnets (Figure 5.5).

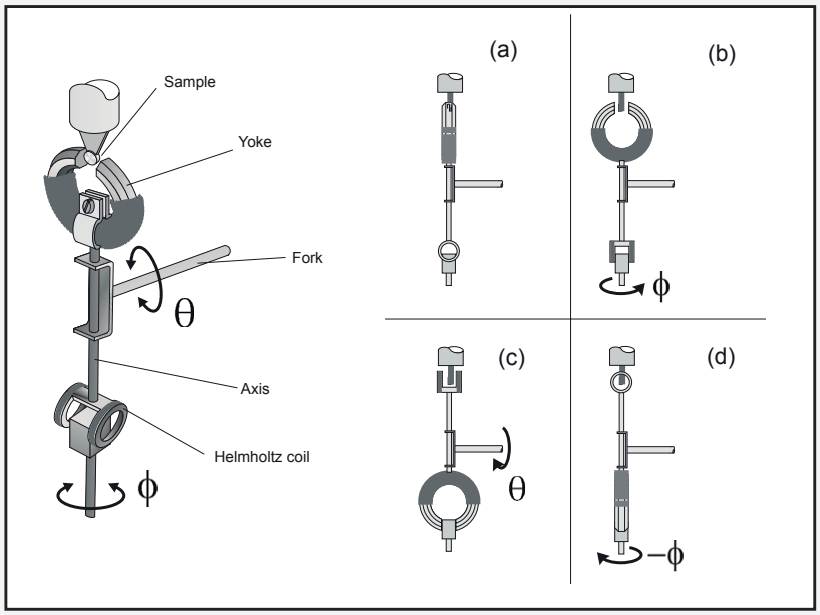

Figure 5.5: (a) Ultralow-temperature cryostat (T = 2–300 K) compatible with the different types of magnets: static high-field, high-field pulsed or permanent magnet. (b) Different geometries for the magnet holder. Reproduced from Rev. Sci. Instrum. **73**, 369 (2002), F. Heigl, O. Krupin et. al.

5.6.1.3 Fast-scan in-vacuum stage

The sample stage will have a flexible mounting interface (e.g. for cooling) and should hold, for instance, samples that consists of large membrane arrays on wafers. It would enable fast scans with micrometre-positioning precision at 10 Hz European XFEL pulse operation (Figure 5.6).

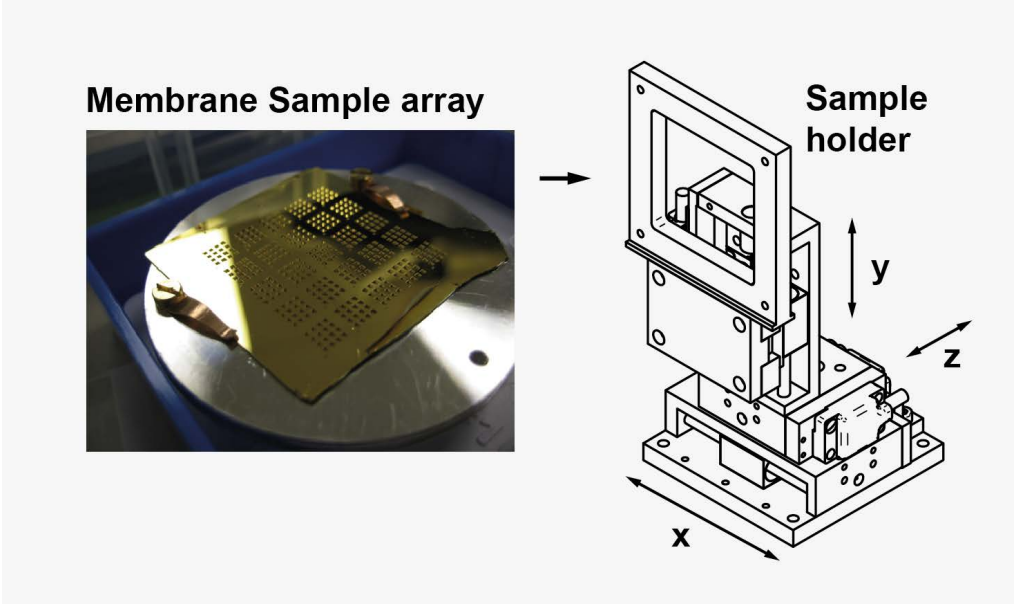

Figure 5.6: Typical in-vacuum stage with *xyz* motion. Sample rotation and cooling could be supplemented. The motion range would allow for reaching samples in large membrane arrays on wafers. The example shows a wafer piece 25 × 25 mm in size.

5.6.2 Cryostats

Cryogenic cooling technology is a well-developed technology widely used in scientific experiments. Liquid-helium continuous-flow cryostats, closed-cycle cryostats, and multistage cryostats achieve temperatures lower than the liquid-helium temperature. They are commercially available and could be employed for the integration of the sample environments described in Section 5.6.1, “Fixed-target installation".

5.6.3 Magnetic fields

Different types of magnets can be envisioned for the SCS instrument to satisfy particular needs of the user experiments:

Options for magnetic-field environments

- High-field pulsed magnets with fields up to 30 T
- Commercial static/rapid-scan magnets with fields up to 8 T
- Including 2D vector magnets with fields up to 5 T
- Conventional electrical iron yoke magnets with fields up to 0.3 T
- Permanent magnets with fields up to ~ 1.5 T

5.6.3.1 High-field pulsed magnets

The high-field pulsed magnets are currently under development in the Sample Environment group (WP79). The considered designs are illustrated in Figure 5.7 on the next page. The magnets will have inner bore sizes in the range of 8 to 20 mm, producing the fields up to 30 T.

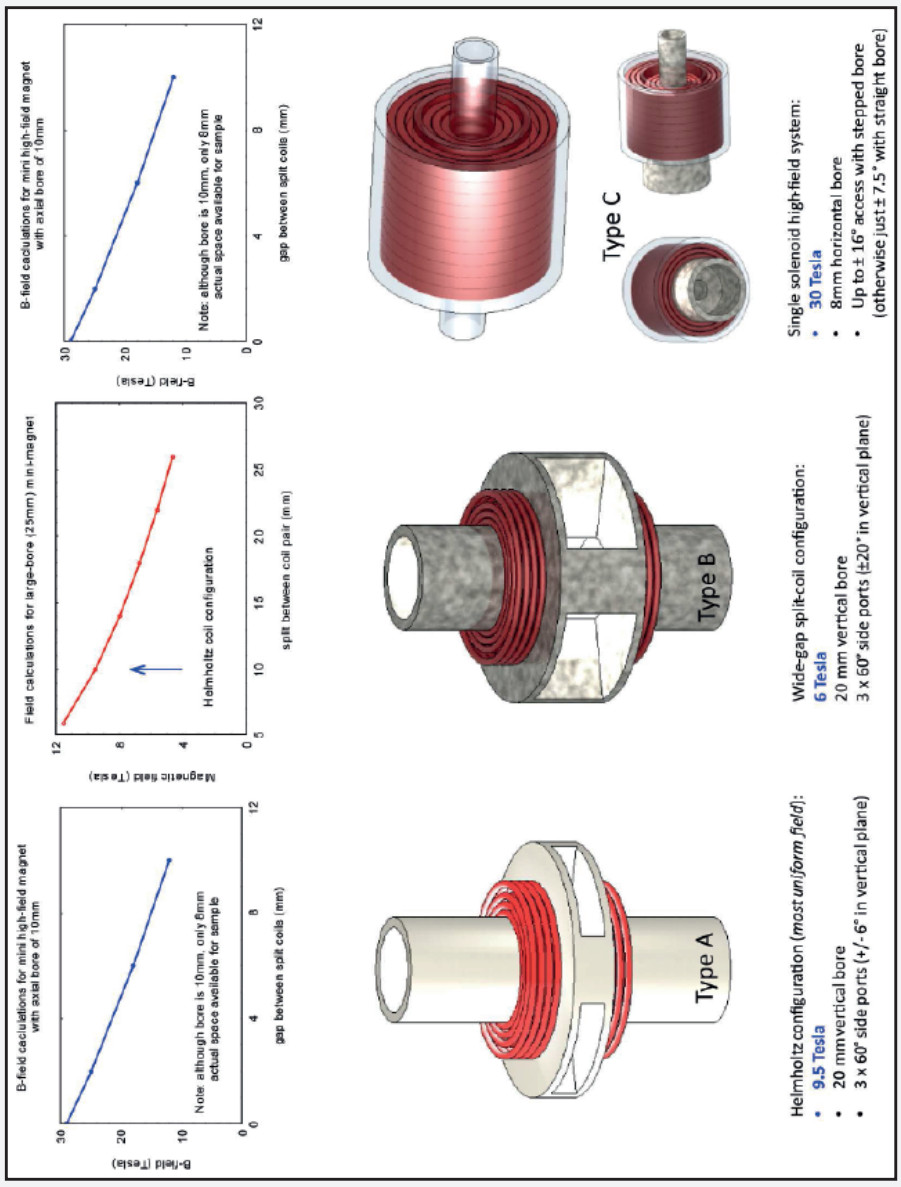

Figure 5.7: Pulsed high-field magnets and their parameters as developed by WP79 at European XFEL

5.6.3.2 Commercial high-field magnets

Commercially available static/rapid-scan magnets, including 2D vector magnets, can be used to obtain magnetic fields up to 8 T (Figure 5.8).

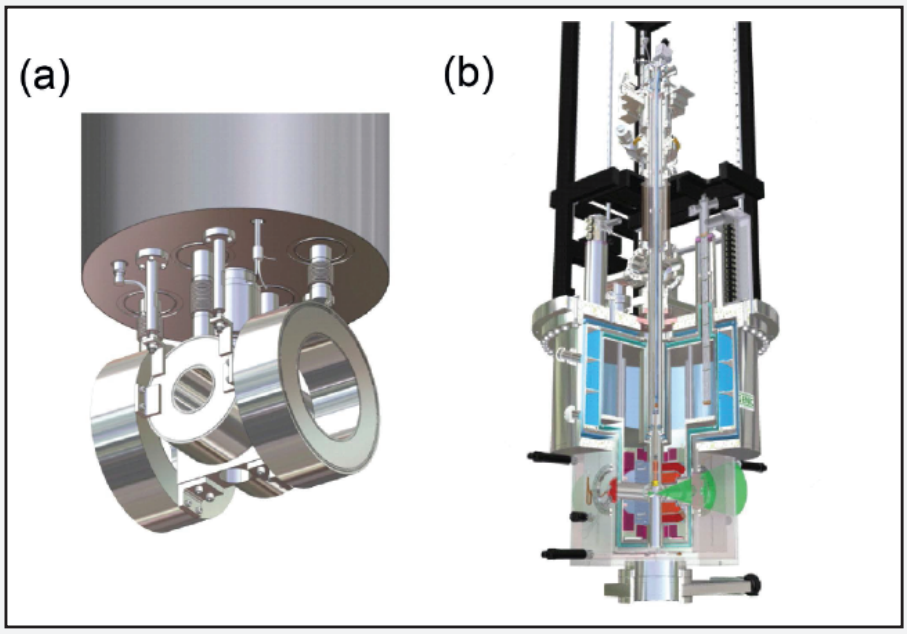

Figure 5.8: Commercially available static/rapid-scan magnets (~ 8 T): (a) 2D vector magnet from Oxford Instruments and (b) from Cryogenics Ltd.

5.6.3.3 Permanent magnets

Permanent magnets, such as neodymium magnets (N52), can be used for experiments that require only a static magnetic field.

Neodymium magnets (N52) have typical parameters as follows:

- Dimensions: 7.5 × 10 mm / Volume: 442 mm^3
- NdFeB magnet in N52 (1.48 T)
- Magnetized direction: through 10 mm
- N-pole marked
- Coating: nickel
- Max. operating temperature: 80°C

6 Detectors

6.1 Experimental requirements

The experimental requirements for 2D array detectors in terms of frame rate, dynamical range, and geometries depend strongly on the science case and samples. The tightest constraint is given by how fast samples could be replenish in the X-ray beam. In contrast to liquid jets and injected particles, fixed targets or solid-state systems pose a particular limit on the rate at which new samples can be positioned in the beam with a precision that could range from the sub-millimetre down to the one micrometre level. The Sample Environment group (WP79) is currently developing an in-vacuum fast sample exchanger (see Section 5.6, "Sample environment and delivery") that would provide this capability at a rate of 10 Hz. Other important constraints are the number of required photons per X-ray pulse and the acceptable sample radiation dose. These constraints would further divide experiments into non-destructive and destructive categories. These considerations lead to the choice of operation mode, i.e. acquiring data at a 10 Hz rate or up to 4.5 MHz (bunch train).

The Detector Development group (WP75) has several detector development programmes running [24]. The DEPFET Sensor with Signal Compression (DSSC) [36], FastCCD [11], and pnCCD [49] are the options for the soft X-ray energy range. Their specifications are listed in Table 6.1 on the next page.

In principle, all detectors could either be used in 10 Hz or 4.5 MHz pulse train operation, even though only the DSSC performs a frame capture of 4.5 MHz. If the dynamic range of the detector is sufficient and a pulse-by-pulse diagnostics or data binning is not required, the FastCCD or pnCCD can be used to integrate the signal over the bunch train. This offers a detector option where a small pixel size detector is mandatory and could offer an option for the hRIXS spectrometer detector.

In the following, we describe the particular detector modalities and the resulting boundary conditions for *CXDI experiments*, which have the highest demands on the detectors. Given the short time period in which this CDR was compiled, only the detector integration and experiment geometries will be described. A fully detailed and technical description of detector geometries, including CXDI simulations, will be presented in the forthcoming SCS TDR.

Table 6.1: Specifications and performances of the DSSC, FastCCD, and pnCCD detectors in the soft X-ray energy range (from WP75)

Specification	**DSSC**	**FastCCD**	**pnCCD**
Photon energy range	0.5–6 keV	0.25–6 keV	0.05–20 keV
Number of pixels	1024×1024	1960×960	256×256
Pixel coordinates	Hexagonal	Cartesian	Cartesian
Pixel size	204×236 µm^2	30×30 µm^2	75×7 µm^2
Dynamic range	10^4	10^3 above 0.5 keV	10^3 at 12 keV
Max. frame rate	4.5 MHz	200 Hz	200 Hz
Min. el. noise	50 e^- rms	25 e^- rms	2 e^- rms
Storage capacity	640 frames	0	0
Vacuum operation	$10^{-7} - 10^{-6}$ mbar	$10^{-7} - 10^{-6}$ mbar	$10^{-7} - 10^{-6}$ mbar
Central hole	Yes	Yes	No
Variable size	Yes	No	No

6.2 Detector geometry and CXDI sampling

An (x, y) array detector samples a coherent diffraction pattern along one dimension at N discrete values and interval u. The optimum sample–detector distance depends on the size of the object and the wavelength λ. This condition can be derived by considering the minimum momentum transfer $q^{\min}$ that can be readily defined from Figure 6.1 as

$$q_{x,y}^{\min} = \frac{4\pi}{\lambda z} u_{x,y} \tag{6.1}$$

where we made use of the small-angle approximation and where z is the sample–detector distance. The minimum momentum transfer defines the largest dimension in real space or field of view (FoV)

$$\mathrm{FoV} = \frac{2\pi}{q_{x,y}^{\min}} = \frac{\lambda z}{u_{x,y}} \,. \tag{6.2}$$

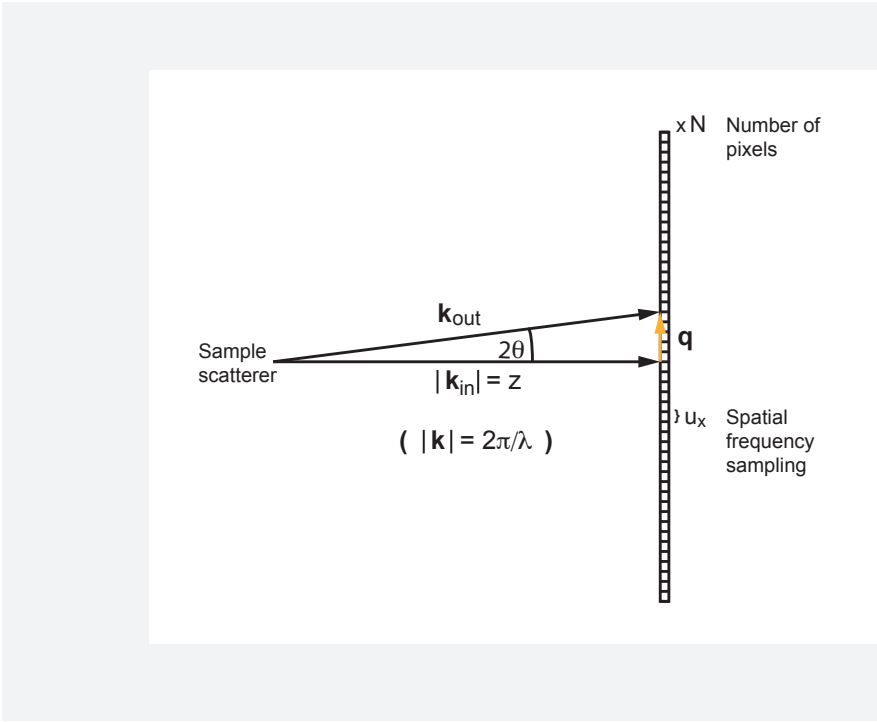

Figure 6.1: Definitions of the detector geometry and CXDI sampling (see text)

In Fourier transform holography (FTH) [12; 40; 30; 18; 53], the object region of size ϕ_{obj} is holographically encoded by a reference scatterer of size $\phi_{\mathrm{ref}} \ll \phi_{\mathrm{obj}}$ that is placed at a minimum reference–object distance of $1.5 \times \phi_{\mathrm{obj}}$ [39]. By Fourier inversion or

back-propagation to the object plane, this compact form of a hologram results in a real-space FoV that is four times larger than the object size of interest, i.e. $\mathrm{FoV} = 4\phi_{\mathrm{obj}}$. The ratio of FoV to object size is also called the oversampling factor Ξ. In fact, an oversampling factor of $\Xi = 4$ or 5 is typical in CXDI for a successful reconstruction of the object in real space using phase retrieval algorithms (see [52] and references therein). Hence, the detector geometries that are discussed in the following are applicable to both imaging approaches. Using Equation 6.2 on the previous page, we can determine the optimum sample–detector distance for a given wavelength and object size according to

$$z = \Xi \cdot \frac{\phi_{\mathrm{obj}} \cdot u_{x,y}}{\lambda} = \frac{\mathrm{FoV} \cdot u_{x,y}}{\lambda} \simeq 4 \cdot \frac{\phi_{\mathrm{obj}} \cdot u_{x,y}}{\lambda} \,. \tag{6.3}$$

The real-space resolution ξ is derived from considering the largest momentum transfer

$$q_{x,y}^{\mathrm{max}} = \frac{4\pi}{\lambda z} \cdot (N_{x,y}/2) \cdot u_{x,y} \tag{6.4}$$

that is captured by the detector (cf. Figure 6.1 on the preceding page). The real-space resolution is then given by

$$\xi_{x,y} = \frac{2\pi}{q^{\mathrm{max}}} = \frac{\lambda z}{N_{x,y} \cdot u_{x,y}} \,. \tag{6.5}$$

As the detector distance is determined by the sample size and wavelength, the spatial resolution is obtained by inserting the expression of z from Equation 6.3

$$\xi_{x,y} = \Xi \cdot \frac{\phi_{\mathrm{obj}}}{N_{x,y}} = \frac{\mathrm{FoV}}{N_{x,y}} \,. \tag{6.6}$$

Intuitively, the attainable spatial resolution is limited to the object size and the available number of detector pixels. In Table 6.2 on the facing page (DSSC) and Table 6.3 on the next page (FastCCD), the detector distances and attainable resolutions are listed for different object sizes and photon energies.

Table 6.2: DSSC boundary conditions for different sample sizes and the resulting best achievable resolutions in 2D imaging

Sample size ϕ_{obj} [µm]	1	3	5	10
FEL diameter [µm]	3	9	15	30
DSSC distance [mm]				
0.5 keV	355	1065	1774	3549
0.8 keV	568	1703	2839	5678
1.2 keV	852	2555	4259	–
2.0 keV	1420	4259	–	–
3.0 keV	2129	6388	–	–
Resolution [nm]	4	12	20	39

Table 6.3: FastCCD boundary conditions for different sample sizes and the resulting best achievable resolutions in 2D imaging. The FastCCD has 1960 × 960 pixels, and the values in parentheses correspond to the long detector edge with 1960 pixels.

Sample size ϕ_{obj} [µm]	1	3	5	10
FEL diameter [µm]	3	9	15	30
FastCCD distance [mm]				
0.5 keV	48	145	242	484
0.8 keV	77	232	387	774
1.2 keV	116	348	581	1161
2.0 keV	194	581	968	1936
3.0 keV	290	871	1452	2904
Resolution [nm]	4 (2)	13 (6)	21 (10)	42 (21)

6.3 Expected detector working distances and second diffraction plane

Using FTH or other holographic approaches [12; 40; 30; 56; 38], the fixed-target sizes have a typical range between ϕ_{obj} = 1–3 µm. In case of single-particle imaging, nanoparticles, biomolecules, or organelles have object sizes that range from less than 0.1 to 3 µm [29]. According to Table 6.2 and Table 6.3, it can be expected that the most important detector working distances range from 0.35 to 6.5 m for the DSSC detector and from 0.04 to 1.0 m for the FastCCD detector at 0.5–3.0 keV photon

energies. This geometry is compatible with the available space in the SCS experiment hutch.

Recording the low-q information is crucial for the real-space image recovery. The central problem is the dynamic range of the detectors as the signal levels at high-q are several orders of magnitude weaker than the low-q ones. The centre hole of the DSSC and FastCCD avoid detector beam damage. An adjustable centre hole (DDSC only) and pixel signal gain further allow for avoiding signal overflow in the centre pixels. The missing low-q information will then be recorded in a second diffraction plane and stitched to the first diffraction plane by back-propagation. The position of and sampling in the second diffraction plane require detailed simulations of objects with generic structure factors. The simulations will be performed with the coherent resonant X-ray scattering (COREXS) simulator and will be reported in the SCS TDR. First results on holographic structures indicate that a second diffraction plane is needed and suitable detector geometries have to be defined.

6.4 Highest spatial resolutions in time-resolved X-ray diffraction

Time-resolved X-ray diffraction allows for studying dynamics in complex systems at unprecedented time and spatial resolutions [17; 22]. It is not always necessary to acquire real-space information, as detailed and sufficient information may already be obtained from the dynamic structure factor. In case the structure factor of a complex system subscribes to several real-space models, imaging may ultimately be required. The object dimension plays a secondary role unless speckles in the diffraction patterns need to be resolved (XPCS). Therefore, the spatial resolution or the smallest length scale that can be observed in time-resolved X-ray diffraction is given by the shortest sample-detector distance. Employing Equation 6.5 on page 94, the SCS instrument would provide ~ 1 nm spatial resolutions using either the DSSC and or the FastCCD detector. The DSSC detector interface to the FFT chamber will include a removable gate valve. The smallest observable length scales of corresponding sample–detector distances are listed in Table 6.4 on the next page.

Table 6.4: Shortest observable length scale (corresponding to the largest momentum transfer) at the minimum detector–sample distance as a function of photon energy. The shortest sample distances of the DSSC detector are 150 mm and 280 mm, with a gate valve that separates the end station from the detector module.

Photon energy [keV]	ξ_{min} [nm] DSSC (150 mm)	ξ_{min} [nm] DSSC (280 mm)	ξ_{min} [nm] FastCCD (40 mm)
0.5 keV	1.7	3.1	1.7
0.8 keV	1.0	1.9	1.1
1.2 keV	0.7	1.3	0.7
2.0 keV	0.4	0.8	0.4
3.0 keV	0.3	0.5	0.3

6.5 DSSC detector

The DSSC detector will provide maximum frame rates of 4.5 MHz for the photon energy range of the SCS instrument [36]. The detector can store at least 640 frames within the pulse train and a veto trigger allows for rejecting frames on-the-fly before all frames are read out to the data acquisition system between consecutive pulse trains. The detector is based on a pixelated silicon sensor with integrated DEPFET (Depleted P-Channel Field Effect Transistor) signal amplification structure. The total sensor size is 210×210 mm^2 with 1024×1024 pixels of hexagonal shape. The hexagonal pixel pitch is 204×236 µm^2. A nonlinear DEPFET characteristic enables a dynamic range of 10^4 (at 1 keV) without compromising single-photon detection sensitivity. The gain can be lowered between pulse trains on a pixel-by-pixel basis to further extend the dynamic range, an option that is particular important to avoid overflow of the central low-q data in single-shot imaging. This makes the detector highly adaptive to CXDI experiments. The unscattered beam can pass the variable detector centre that is formed by offsetting the quadrants (detector tiles). A detailed description of the DSSC is given in [36].

6.5.1 DSSC detector integration

The detector will be hosted in a vacuum system, which is currently being designed (see Figure 6.2 on the following page). The current design proposes a DN800 flange interface to the end stations, which poses a constraint on the FFT chamber dimension.

It is advantageous to have a gate valve between the detector and the FFT chamber (see Figure 5.3 on page 81), thereby separating the vacuum systems. The gate valve would allow for independent servicing of the detector and the FFT chamber, or protecting the detector in beam alignment or experiment preparation modes.

For optical pump, X-ray probe experiments, an optical filter and iris are required to shield off optical stray radiation that could produce sizeable signal backgrounds on the detector. The comparably long sample–detector distances (Table 6.2 on page 95) are sufficient to place these extra components near the detector interface.

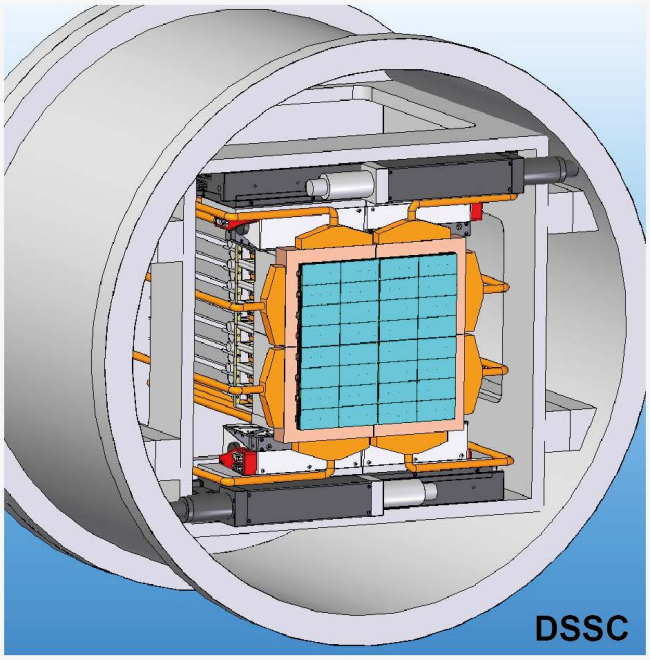

Figure 6.2: DSSC detector module. The proposed design currently considers a DN800 flange interface to the end stations.

In most experiments, it will be required to change the photon energy in order to tune to certain X-ray absorption resonances. Therefore, the sample–detector distance has to be adjustable over larger distances (0.35–6.5 m). It is envisioned to place the detector on a sliding carriage that is supported by a girder of respective length. As a rather long travel range is needed, working ranges will be defined in terms of sample size and photon energy range. In the technical design of the detector girder, a “close distance” (< 0.5 m), an “intermediate distance” (0.5–2 m), and a “far distance” (2–6 m) operation are foreseen.

6.5.2 Hexagonal versus Cartesian detector sampling

The DSSC detector samples diffraction data on a hexagonal lattice. This type of sampling is particularly attractive for rather isotropic sample structure factors. Fast conversion schemes exist to change between the hexagonal and the more convenient Cartesian representation of the 2D data. Such conversion schemes come with different levels of data loss due to the extrapolation methods between the sampling grids. Therefore, the CXDI data processing will be first performed in the hexagonal coordinates, e.g. using respective discrete Fourier transform algorithms, before representing the image reconstructions or diffraction data in Cartesian coordinates. The data conversion schemes and inflicting noise levels will be investigated in simulations as part of the SCS TDR. Figure 6.3 shows a reversible, fast, and high-quality grid conversion scheme that is based on three successive shear operations conserving the power spectral density [9].

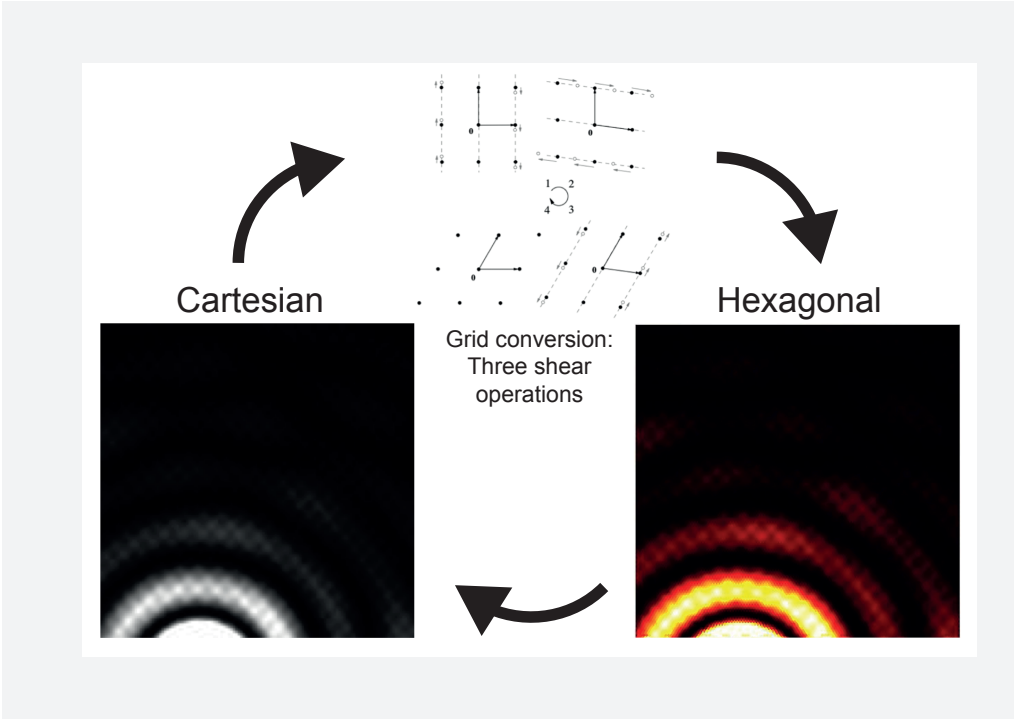

Figure 6.3: Reversible Cartesian (left) to hexagonal (right) grid conversion of an X-ray hologram by three shear operations (centre, adapted from [9]). This method conserves the power spectral density.

6.6 FastCCD detector

The first generation of the FastCCD detector was employed in the resonant soft X-ray scattering (RSXS) chamber at the Soft X-ray Materials Science (SXR) instrument of LCLS [11]. The FastCCD detector with the specifications given in Table 6.1 on page 92 represents the second generation and will be available at the SCS instrument. The frame rate of 200 fps is not compatible with the 4.5 MHz bunch train operation, but the “fast transfer mode” of the detector makes it possible to capture two frames (960×960 pixels) per pulse train on the sensor. The detector has a pixel size of 30 µm and offers an option for experiments where a small pixel size detector is mandatory (e.g. for the hRIXS spectrometer) and pulse train–integrated signals are acceptable. The detector will be the day-one option for fixed-target single-shot imaging at 10 Hz repetition rate, as a full DSSC detector (four quadrants) will first become available in 2017.

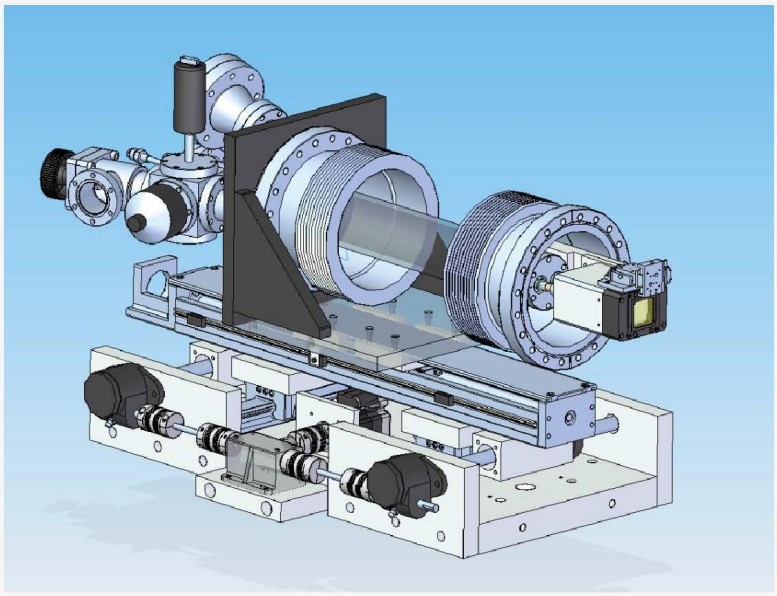

Figure 6.4: Possible scheme to integrate the FastCCD detector for experiments at the SCS instrument. This setup was developed for integrating commercial in-vacuum CCDs in the Resonant Coherent Imaging (RCI) chamber at LCLS.

6.6.1 FastCCD detector integration

The overall size and design of the FastCCD resembles commercial in-vaccum CCD detectors. The FastCCD detector integration could be built on existing detector stage designs of the RCI chamber at the SXR instrument of LCLS shown in Figure 6.4 on the preceding page. In this design, the travel range of the detector along the beam axis is 400 mm. As the smaller numerical aperture of the detector requires sample–detector distances that are as short as ~ 40 mm, the entire detector has to be moved into the FFT chamber, and further space constraints in the technical design of the sample environment have to be considered. The optical laser shielding needs to be attached to the detector housing. The FastCCD may also serve in combination with the DSSC detector as second diffraction plane detector to recover the missing low-q data.

7 Instrument diagnostics

Due to the stochastic character of the X-ray free-electron laser (XFEL) SASE process, a pulse-by-pulse photon diagnostics is crucial for a quantitative analysis of the recorded experimental data in nearly all user experiments at the SCS instrument. Ideally, the photon beam diagnostics should be performed in a non-perturbative way and should run in parallel with user experiments in order to provide the photon beam parameters on a pulse-by-pulse basis. The main X-ray diagnostic parameters are the pulse energy, the beam position, the pulse arrival time, the photon energy, the polarization of X-ray pulses, and their transverse and longitudinal coherence. The layout of the diagnostic tools along the SCS beamline is shown in Figure 7.1.

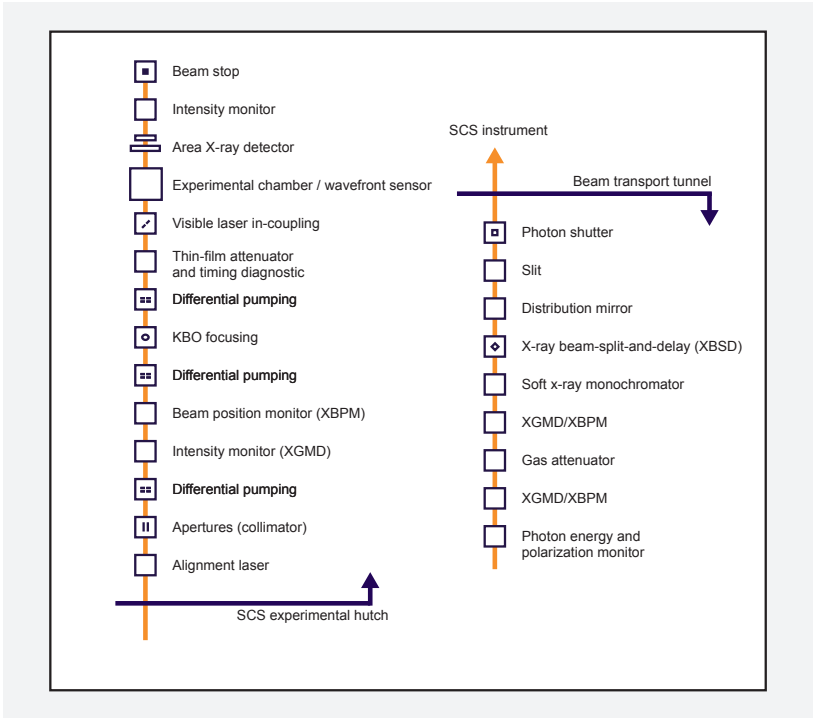

Figure 7.1: Layout of the SCS diagnostic tools

7.1 Intensity monitor

Three X-ray gas monitor detector (XGMD) and X-ray gas position monitor (XBPM) units will be installed upstream of the SCS experiment chamber along the SCS instrument beam path. Two of them will be installed in the tunnel before and after the gas attenuator for precise measurement of the pulse energy and beam position. The third unit will be installed after the monochromator exit slit in the SCS experiment hutch for probing the monochromatic beam intensity, as there is little correlation between the pink and the monochromatic beam due to the spectral SASE fluctuations.

The application of gas-based devices for the photon beam diagnostics at the SCS instrument is the appropriate choice, as they do not invade the X-ray beam properties and demonstrate very good performance in extensive tests at synchrotrons and FELs around the world. Currently, the designated SCS XGMD and XBPM are already in the design and construction phase at DESY. A schematic diagram of the XGMD and XBPM is shown in Figure 7.2.

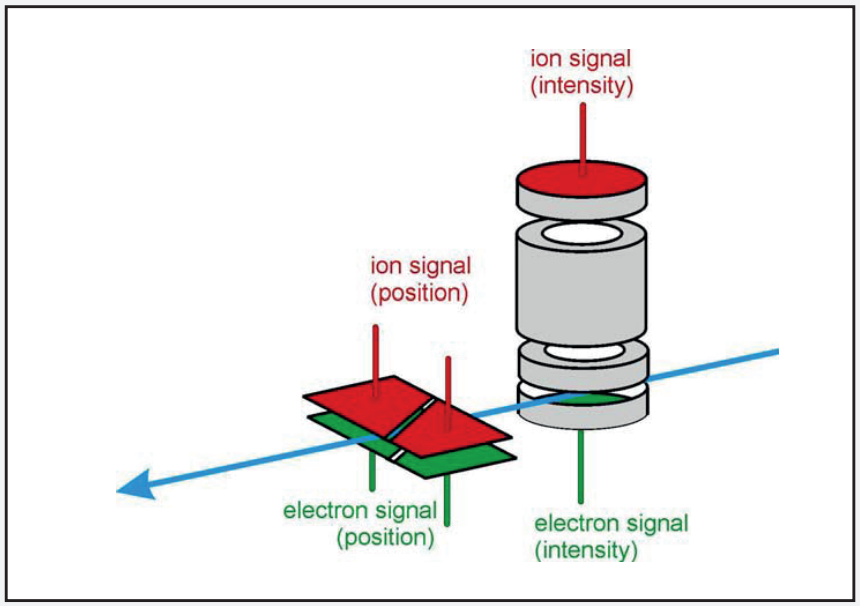

Figure 7.2: Schematic diagram of XGMD and XBPM: The X-rays propagate through a noble gas at gas pressures in the range of 10^{-4}–10^{-6} mbar in order to generate electrons and ions that are extracted by an electric field and detected at the electrodes. Reproduced from [51].

The operation of the XGMD and XBPM units is based on the detection of photoionized ions that are created by the X-ray pulses propagating through a noble-gas environment. The precise ion current measurements are performed in the XGMD unit, which allows for both the absolute, time-averaged intensity and the relative, pulse-to-pulse intensity diagnostic of the X-ray photon beam. The position of the X-ray beam is monitored in the XBPM unit in terms of the spatially resolved detection of ions that are extracted with a homogeneous electric field. The prototypes of the two devices have already been built, tested, and optimized for a few years; currently, it is safe to assume that they will meet the SCS requirements in terms of sensitivity.

A sketch of the XGMD unit consisting of two chambers is given in Figure 7.3. The large-area metal-plate electrodes and a small-aperture commercial multiplier are located in the first chamber. The second chamber holds a huge-aperture open multiplier (HAMP). The targeted operation pressure of the XGMD is of the order of 10^{-4} mbar using conventional metal-plate electrodes, which can be extended downwards to 10^{-6} mbar operation pressure when the small-aperture commercial photomultiplier is used. In the HAMP chamber, the generated ion current per X-ray pulse is further amplified by a cascaded electron emission process taking place in the large-area open electron multiplier section, which consists of 25 aluminium meshes and is electrically biased by 10 kV (400 V/mesh).

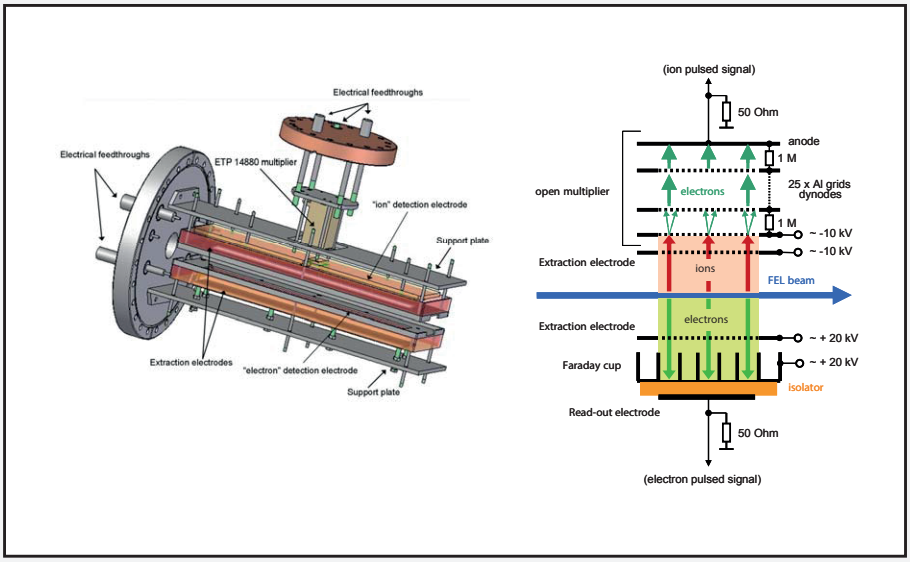

Figure 7.3: XGMD unit: The first part of the XGMD chamber consists of the plane electrode detectors and the small-aperture photomultiplier. The second part of the XGMD is the HAMP detector [51].

Specifications of the XGMD unit at soft X-ray energies

- Operating pressure: 10^{-4} mbar (down to 10^{-6} mbar using the photomultiplier)
- Gases: Xe for the high-energy part of the SCS monochromator energy range, Kr for the low-energy part of the SCS monochromator energy range
- Uncertainty of absolute pulse energy measurements (integration time 20–30 s): < 10%
- Uncertainty of relative pulse-by-pulse energy measurements (with HAMP detector): < 3% (for 10^8 photons/pulse);
  or uncertainty of relative pulse-by-pulse energy measurements (with HAMP detector): < 10% (for 10^6 photons/pulse)
- Temporal resolution: < 180 ns
- Apertures along the X-ray beam path: 30 mm
- Length of the XGMD and XBPM section: ~ 2.3 m.

7.2 Beam position monitor

For pulse-to-pulse diagnostics of the X-ray beam position fluctuations, a XBPM unit will be employed that is being developed at DESY together with the above-mentioned XGMD device. The operation of the XBPM unit is based on the spatially resolved detection of the electrons and ions that are photogenerated by the X-ray beam pulses traversing a noble-gas environment between two split-electrode plates in the interaction chamber. Those electrons and ions are extracted by a static homogeneous electric field that is applied between the diagonally split electrodes, as illustrated in Figure 7.2 on page 103. The signal collected by each electrode is proportional to the length of the X-ray beam path projection on the corresponding electrode because of the static homogeneous electric field. Therefore, the individual current signals recorded on the diagonally split electrodes can be converted into an X-ray beam position relative to the electrodes.

Specifications of the XBPM unit at soft X-ray energies

- Measurement uncertainty of the time-averaged beam position: 10 µm (for beam position variations of 1 mm)
- Temporal resolution: better than 180 ns
- Operating pressure (Xe, Kr): 10^{-4} mbar
- Detectable position range: ±10 mm minus half the beam size
- Apertures along the optical path of the X-ray beam: 30 mm

7.3 Photon energy and polarization monitor

X-ray pulses of left and right circular polarizations, as well as vertical and horizontal linear polarizations, will become available with the installation of the circular-polarization afterburner at SASE3 (see Section 2.2, "Circular- and linear-polarization afterburner"). These X-ray beam properties will be measured by a photon energy and circular/linear polarization monitor developed by the X-Ray Photon Diagnostics group (WP74).

The photon energy distribution and polarization analysis of the X-ray pulses is realized using photoemission spectroscopy on noble gases. A time-of-flight (TOF) photoemission spectrometer (Figure 7.4 on the facing page) is used to record the energy and angular distribution of the X-ray-excited electrons of suitable noble-gas atoms on a pulse-to-pulse basis. Real-time data processing with a low latency of $< 10^{-5}$ s will allow for online data analysis and for reducing the amount of data stored by the TOF spectrometer.

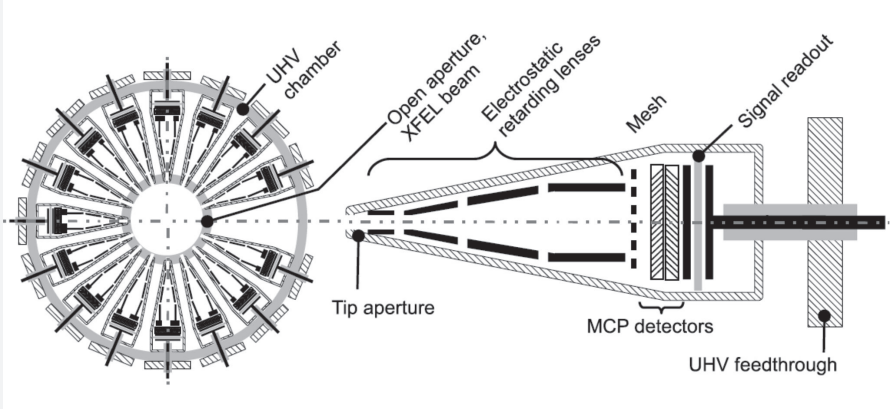

Figure 7.4: Photon energy and polarization monitor: Sketch of the TOF setup consisting of 16 flight tubes and design of the flight tube / detector unit of the TOF spectrometer. Reproduced from [5].

The spectral distribution of the SASE pulses can be reconstructed directly from the photoemission spectra, because the photon energy distribution of the X-ray pulses is projected onto the kinetic-energy distribution of the photoelectrons that are emitted from specific orbitals of the gas atoms. The photon energy distribution is thus monitored via the position and the width of the corresponding photoemission peak. The centre and the width of a single-pulse photon spectrum are the main output parameters that can be used for processing and normalizing user experiment data (Figure 7.5).

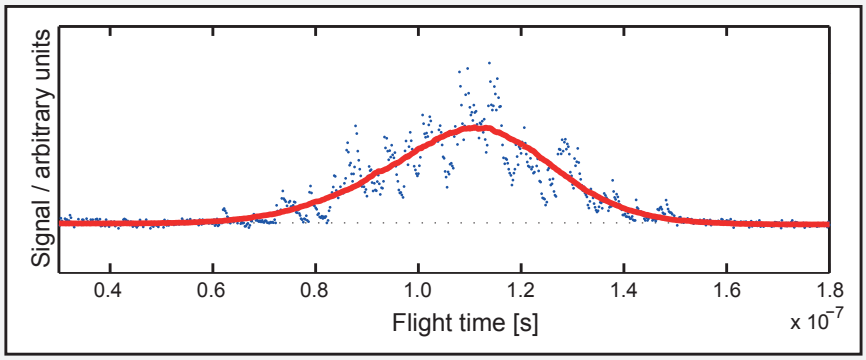

Figure 7.5: Approximation of central energy and width of SASE spectra (red curve) after real-time data processing.

For monitoring the photon beam polarization, the angular distribution of the photoelectrons will be measured and analysed. An array of 16 TOF photoemission spectrometers (Figure 7.4 on the preceding page) will be used for this purpose to observe the photoemission intensity distribution in the plane perpendicular to the X-ray photon beam. The direction and degree of the photon beam polarization can be determined from these measurements by comparing the measured photoelectron angular distribution and the theoretically known atomic photoionization angular distribution of the emitted electrons that is imposed by the linearly polarized X-ray beam.

The stable operation of the photon energy and polarization monitor requires the detection of at least 100 counts per X-ray pulse in the TOF spectrometers. Figure 7.6 on the next page represents the estimated counts for pulse durations of 2 fs (10^{11}–10^{12} photons per pulse) and 100 fs (10^{13}–10^{14} photons per pulse) versus the partial gas pressure. Overall, the curves look promising in the lower range of the SCS instrument photon energies, while count rates in short-pulse operation and/or at higher photon energies may be increased by employing pulsed gas injection and thereby enhancing the operation gas pressure. Figure 7.7 on page 110 shows the expected accuracy in the determination of the degree and direction of the linear polarization of X-ray pulses for pulse durations of 2 fs (10^{11}–10^{12} photons per pulse) and 100 fs (10^{13}–10^{14} photons per pulse). The sensitivity of measuring the centre and the width of the X-ray pulse spectra is shown in Figure 7.8 on page 111.

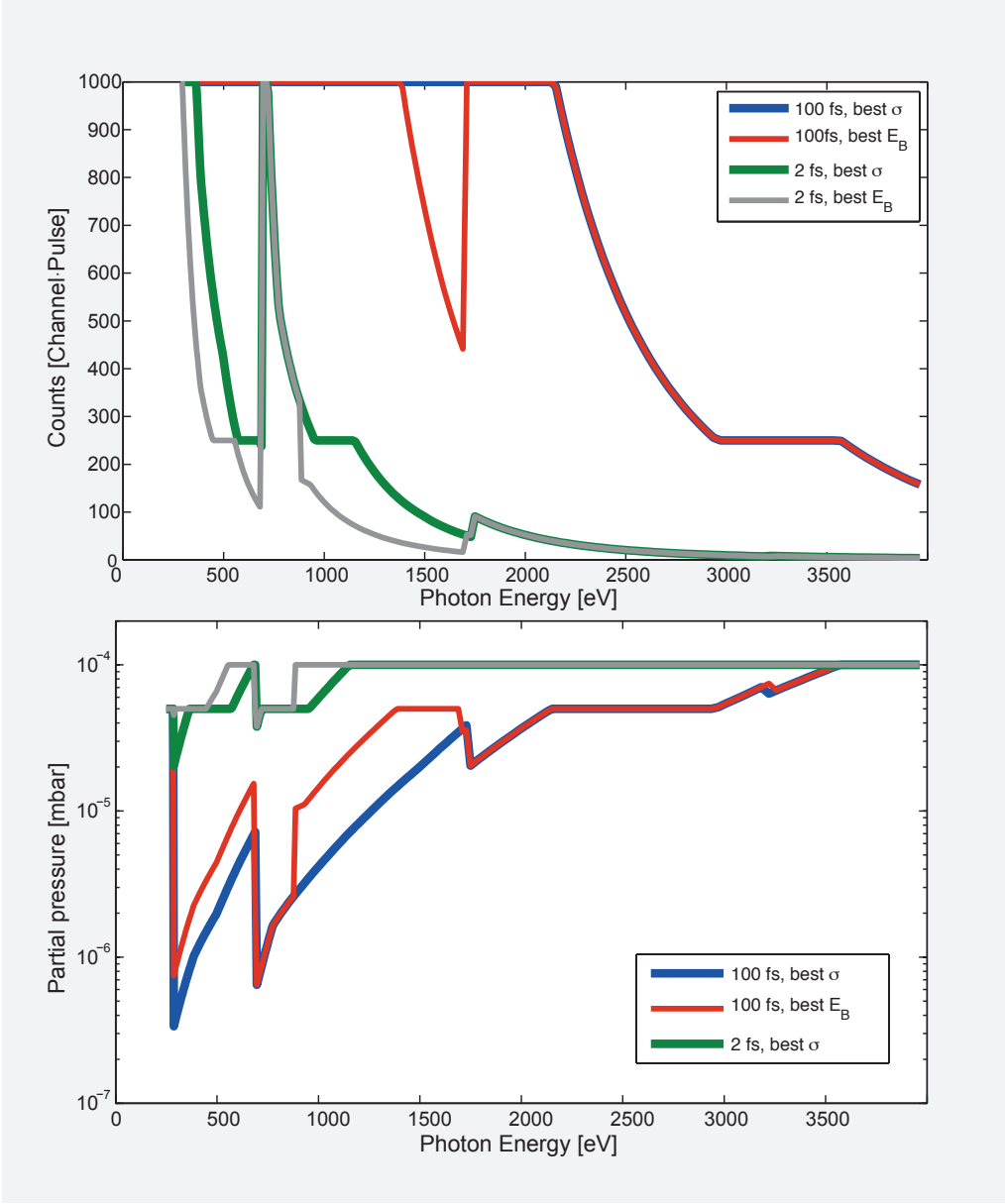

Figure 7.6: TOF detector counts vs. partial pressure for pulse durations of 2 fs (10^{11}–10^{12} photons per pulse) and 100 fs (10^{13}–10^{14} photons per pulse). At least 100 counts per pulse are necessary for stable working of the detector.

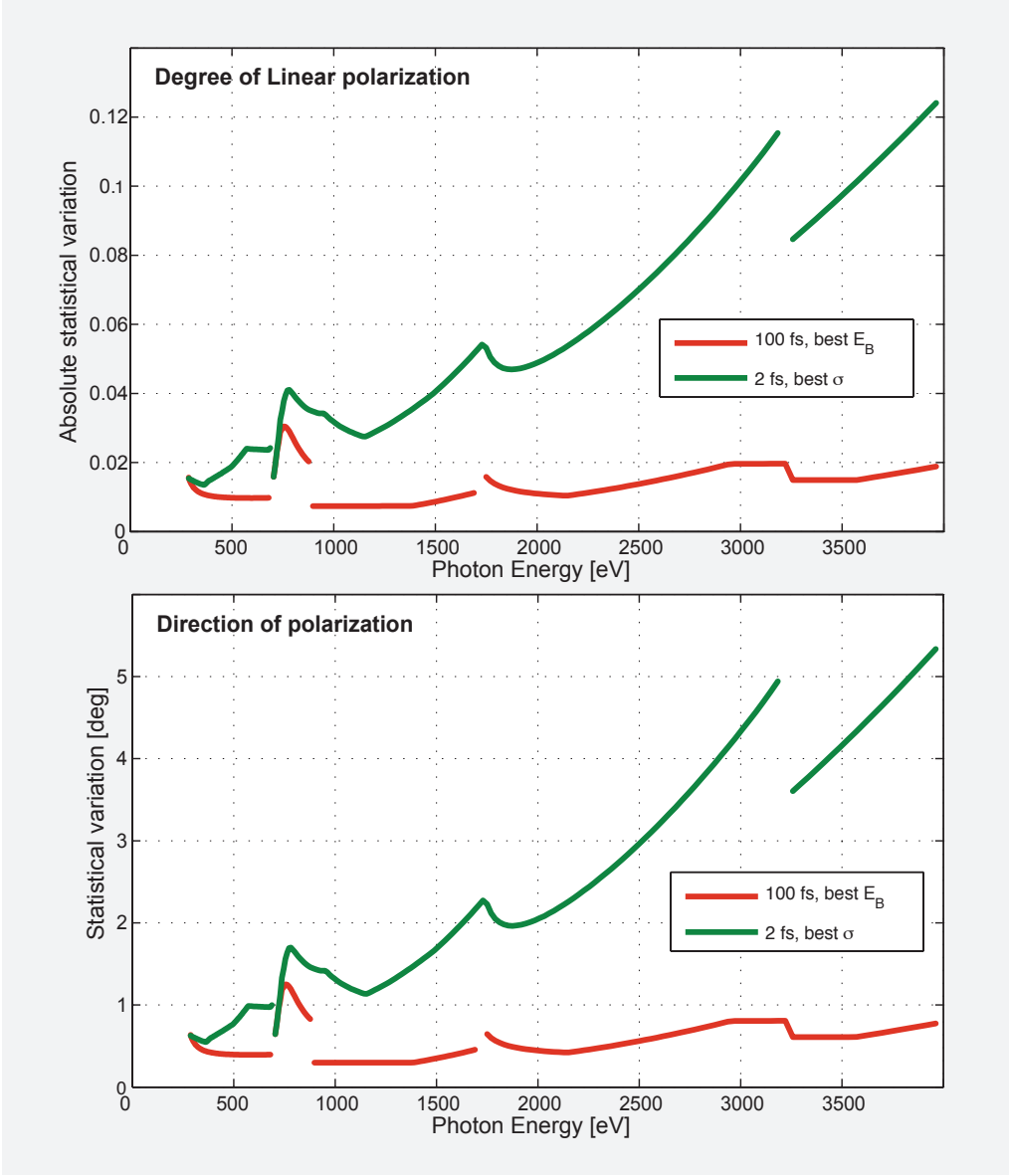

Figure 7.7: Accuracy of determination of degree and direction of linear polarization for pulse durations of 2 fs (10^{11}–10^{12} photons per pulse) and 100 fs (10^{13}–10^{14} photons per pulse). At least 100 counts per pulse are necessary for stable working of the detector.

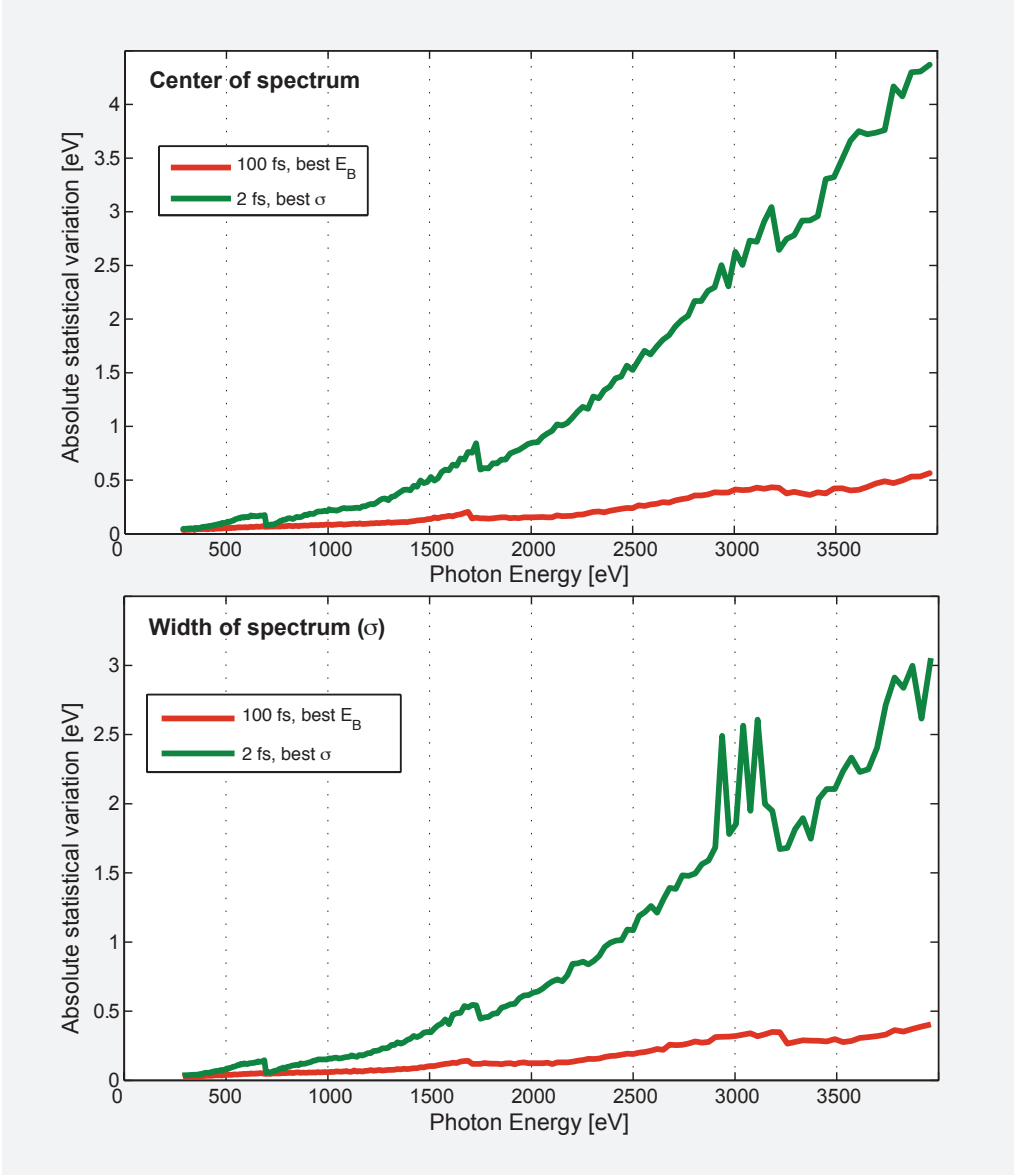

Figure 7.8: Precision of determination of centre and width of the X-ray pulse spectrum for pulse durations of 2 fs (10^{11}–10^{12} photons per pulse) and 100 fs (10^{13}–10^{14} photons per pulse). At least 100 counts per pulse are necessary for stable working of the detector.

The diagnostics of short X-ray pulses of SASE3 in terms of their spectral content may be an important feature that would allow for pulse-to-pulse binning of the experimental data according to the spike structure. This possibility will be explored in more detail in the SCS TDR.

Specifications of the energy and polarization monitor

- Operating pressure (noble gases: Xe, Ne, Kr, Ar): 10^{-6} mbar to 10^{-4} mbar
- Gases: Xe, Kr

7.4 X-ray–optical pulse timing diagnostics

For time-resolved pump–probe experiments at the SCS instrument, temporal synchronization of the X-ray pulses and the optical laser pulses is necessary. Methods for a coarse and fine timing diagnostics have already been developed and tested at FLASH in the UV range and at LCLS in the soft X-ray range [14],[25].

The coarse synchronization on the time scale of a few picoseconds will be performed by monitoring separate optical and X-ray time traces of the pulse-induced electrical current of an antenna cable on a GHz oscilloscope, where the tip of an SMA cable is hit by the optical or the X-ray pulses, respectively (Figure 7.9 on the facing page). The measurements can be performed either by placing the antenna into the interaction point (optical/X-ray focus) of the experiment chamber or by placing the tip somewhere between the laser in-coupling chamber and the experiment chamber. The synchronization in the interaction point is mandatory for non-collinear beam configurations. An oscilloscope with an input bandwidth of ~ 13 GHz is required to observe the electrical pulses, which have a typical rising edge of the order of a few tens of picoseconds. The accurate overlapping of the rising-edge positions allows for a reliable synchronization of the optical laser and X-ray pulses down to a few picoseconds. The optical-induced electrical pulse is generated via a multiphoton photoemission process or sometimes, may result as a direct response of the antenna to the electromagnetic field of the laser pulses (e.g. strong THz excitation). Radio frequency cables with a bandwidth of 15–25 GHz are typically used as antennas. The pulse arrival time of the optical laser pulses with respect to the XFEL pulses for longer delays will be adjusted by electronically shifting the phase of the Ti:sapphire oscillator with respect to the triggering signal of the XFEL timing system.

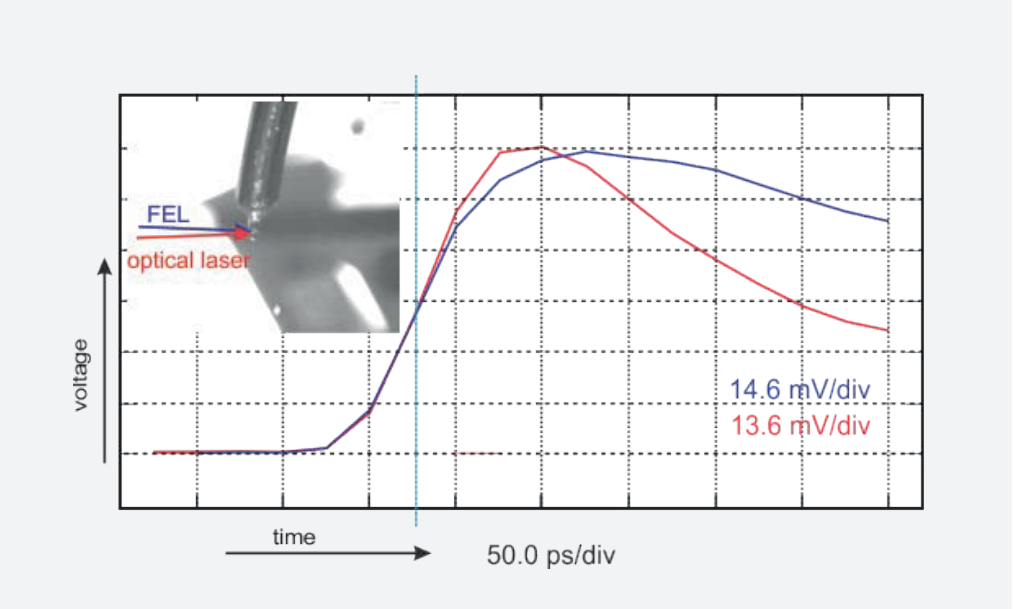

Figure 7.9: Electrical pulses observed on an oscilloscope upon exposure of the radio frequency cable tip to the optical and X-ray beams. Inset: Tip of the cable.

For synchronizing the optical and X-ray pulses on sub-picosecond time scales, the X-ray-induced ultrafast transient change of optical reflectivity of a semiconductor surface can be used. This X-ray-induced transient optical reflectivity of a semiconductor is related to the imposed large density variations of the low-energy charge carriers in the valence and conductance bands. The charge carrier density variation is initially created by the absorption of the X-ray photons that is followed by Auger decay and further auto-ionization processes, which results in an avalanched generation of electron–hole pairs near the band gap.

Finding the temporal overlap in the femtosecond range is typically performed by measuring the transient optical reflectivity from the semiconductor surface exposed to the XFEL pulses. The experiment geometry is schematically shown in Figure 7.10 on the next page and discussed in the following sections.

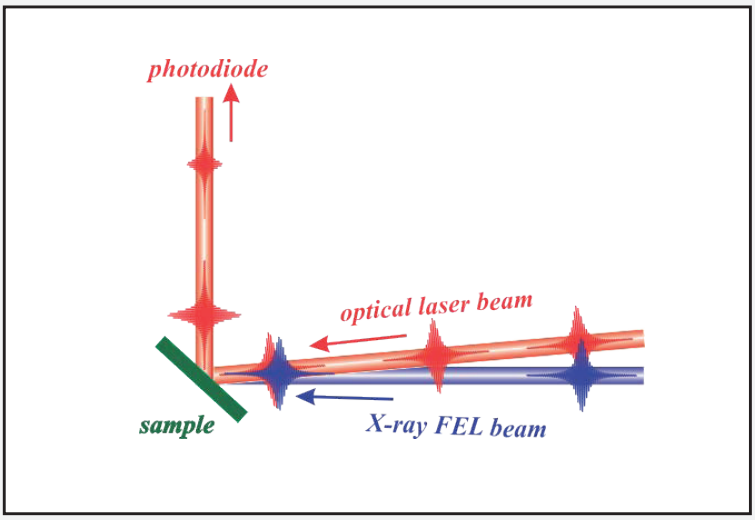

Figure 7.10: Experimental geometry for probing the X-ray-induced transient change of optical reflectivity

7.4.1 Shot-by-shot timing diagnostics

In time-resolved optical/X-ray pump–probe experiments, the relative arrival times between the XFEL pulses and the optical laser pulses have to be recorded on a shot-by-shot basis when the temporal resolution in the experiments has to be much better than the average arrival-time jitter as the limiting factor. The arrival-time jitter is typically around 200–250 fs at LCLS and is expected to be $\leq$ 50 fs at the European XFEL.

Shot-by-shot timing diagnostics was successfully developed at LCLS. The maximum 120 Hz repetition rate of LCLS is, however, considerably lower than the effective 27 kHz at the European XFEL. The European XFEL instrument timing diagnostics for these types of measurements is still in the research and development phase. It is essentially the high repetition rate of the European XFEL burst mode that makes their realization more challenging on a shot-by-shot basis. The X-Ray Photon Diagnostics group (WP74) has the lead on the timing diagnostics development, and the SCS group is actively collaborating with them on this project.

Currently, two main experimental approaches are promising for the realization of the timing diagnostics:

- Measuring the X-ray-induced transient change of optical reflectivity of a semiconducting surface (spatial or spectral encoding techniques)
- Light-field streaking technique

At the time of this SCS CDR, it is left open which technique will be installed at the SCS instrument.

7.4.2 Transient reflectivity method

Exploiting the X-ray-induced transient change of optical reflectivity, two techniques have been proposed and demonstrated: spatial and spectral encoding [3; 4]. The spatial encoding method uses a non-collinear beam geometry, while the spectral encoding technique has a co-propagating geometry of the X-ray and optical laser beams. This makes the spectral encoding technique not prone to vibrations of the reflecting surface. In addition, the experiment setup for spectral encoding measurements appears more convenient, as it requires much less precision in positioning and orientation of the thin-film surface in space and may be realized in a compact and robust “black box” device.

In the case of the spectral encoding technique, the temporal delay information is encoded in the chirped optical pulse spectrum by spectral modulation [4]. The method is illustrated in Figure 7.11 on the following page. Here, optical pulses are generated with a Ti:sapphire laser oscillator emitting broadband pulses in the range of 750–850 nm with 20 fs duration. An optical pulse stretcher is used to lengthen the pulse duration to the picosecond range (up to hundreds of picoseconds). The duration of the stretched pulse can be adjusted by moving diffractive optical elements into the optical stretcher. These chirped optical pulses usually have a positive group velocity dispersion where the red side of the spectrum travels faster than the blue one. The part of the chirped optical laser spectrum that is coincident in time with the X-ray pulse on a thin Si_3N_4 film will experience a spectral modulation caused by the ultrafast transient change of absorption and reflectivity. Then the optical beam is reflected into an optical spectrometer using a thin aluminium film of sub-micrometre thickness while the X-ray beam is deliver to the interaction point of the actual experiment without significant attenuation. The position of the modulated part of the optical spectrum allows for a direct and shot-by-shot diagnostics of the relative arrival times of the optical and X-ray pulses.

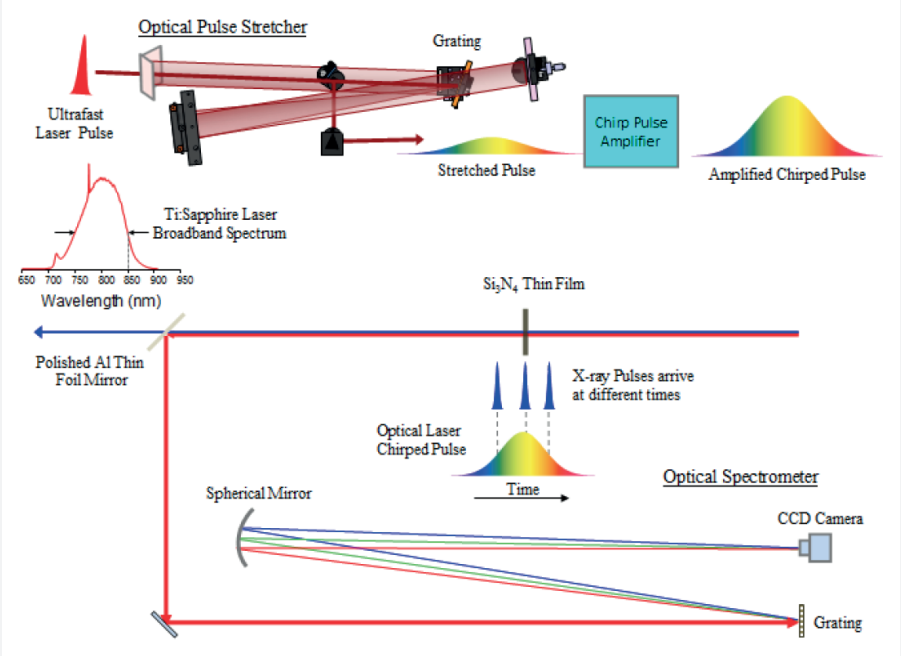

Figure 7.11: Chirped pulses of a Ti:sapphire laser overlap with the XFEL pulses within a Si_3N_4 thin film. The X-ray pulse–induced transient change of the optical reflectivity is encoded in the chirped pulse laser spectrum, reflecting the various X-ray pulse arrival times relative to the optical laser pulses. Reproduced from [27].

This method could offer a temporal resolution of 15 fs for the following, typical experiment parameters: optical spectral range of 750–850 nm, pulse duration of about 5 ps, optical chirp of 50 fs/nm, and 50 µm spatial resolution of an optical camera system in an optical spectrometer. The experiments that have been performed on the soft X-ray-induced transient change of optical reflectivity at the Soft X-ray Materials Science (SXR) instrument of LCLS have shown that X-ray fluences of 10–50 mJ/cm^2 are required to induce enough charge carriers in the semiconductor to confidently produce a detectable transient signal in the optical reflectivity. For operating the timing tool at high-repetition rates, it becomes mandatory to limit the X-ray-pumped area to tens of micrometres in diameter and to operate near the signal threshold reducing the average power deposited in the semiconductor. Here, an X-ray zone plate that transmits the zeroth order X-ray beam downstream to the user experiment may be used to generate a sufficient first-order focused X-ray beam at the timing tool.

7.4.3 Light-field streaking method

The light-field streaking technique relies on measuring, in the presence of the streaking field of an optical laser pulse, the kinetic energy of photoelectrons that are excited by an X-ray pulse in a gas target (Figure 7.12). The optical pulses used for the streaking should satisfy the following conditions: 1) they should have a long oscillation period compared to the X-ray pulse length, 2) they should have a high field strength and be synchronized with the X-ray pulses, and 3) they should have a well-reproducible and stable carrier envelope phase. The photoemission process in the presence of a streaking field results in a modulation of the photoelectron kinetic energy. For ultrashort X-ray pulse diagnosis based on streak cameras, the required streaking-field periods range in the THz or far-infrared regime (ten to hundreds micrometres). In the light-field streaking technique, the X-ray and optical beams are collinear. Both beams are focused onto a nozzle-injected gas jet (Xe or Kr). The excitation of electrons from low-lying 4p and 5p states of the gas leads to large initial kinetic energies and to strong streaking of the photoelectrons. The analysis of the kinetic-energy distribution can be performed e.g. with a TOF electron spectrometer. The phase of the streaking field at the moment of the photoexcitation process can be obtained from the kinetic energy distribution and, consequently, the timing of the X-ray pulses with respect to the streaking laser pulse can be obtained. Recent experiments (Figure 7.12) demonstrated a timing precision of 6 fs (rms) or 14 fs (FWHM).

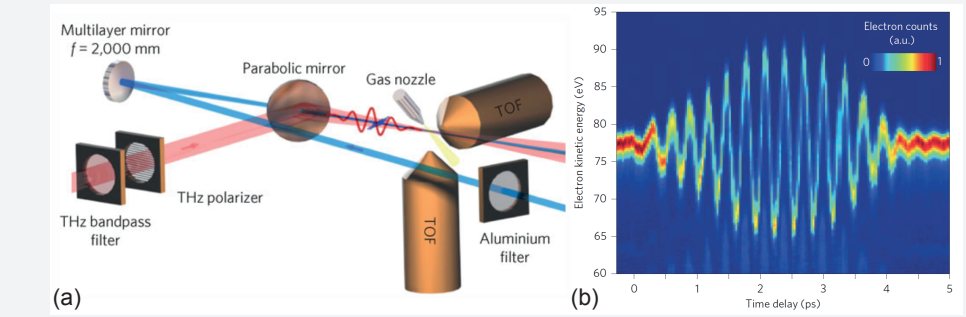

Figure 7.12: (a) Schematic of the experiment setup for the X-ray ionization response in the presence of a THz streaking field. (b) Representative electron energy streaking signals for various time delays of the X-ray/THz pulses. From reference [13].

7.5 Thin-film X-ray attenuator chamber

A chamber with solid X-ray attenuators is foreseen to adjust X-ray pulse intensities at the sample interaction point in the SCS instrument without compromising the required X-ray intensity or fluence levels for the timing diagnostics that have been described in the previous section. The thin-film X-ray attenuator chamber is therefore located downstream of the timing diagnostics but upstream of the laser in-coupling for the optical laser delivery to the sample. The thin films deposited on Si_3N_4 membranes can provide additional attenuation levels of up to a factor of 100 using suitable elements and different thicknesses. The attenuation length can be fine-adjusted by rotating the solid attenuators in the X-ray beam. It has to be explored in the technical design how the thin-film solid attenuators will withstand the high repetition rate operation modes of the European XFEL.

7.6 X-ray optics alignment laser and screens

The position and the alignment of the X-ray beam will be monitored at several positions along the optical axis in the SCS experiment hutch. Here, pop-in monitors and camera systems will visualize the beam profile on apertures and insertable YAG crystals.

8 Optical laser delivery

For performing optical excitations in the pump–probe experiments, an optical laser system capable of generating ultrafast laser pulses in a wide range of optical wavelengths will be installed at the SCS instrument. A conventional femtosecond laser will be used for performing the optical excitations with 800 nm wavelength. Up-conversion with a second-harmonic generation (SHG) box will be used to reach 400 and 266 nm excitation wavelengths. However, in condensed-matter systems, such as high-temperature superconductors, highly correlated systems, etc., phenomena of interests are coupled to low-energy quasiparticle excitations (phonons, magnons, spin density waves, etc.) lying on the energy scale of tens to hundreds of millielectronvolts. The distribution of the low-energy excitation modes in condensed-matter systems over the optical spectral range is illustrated in Figure 8.1.

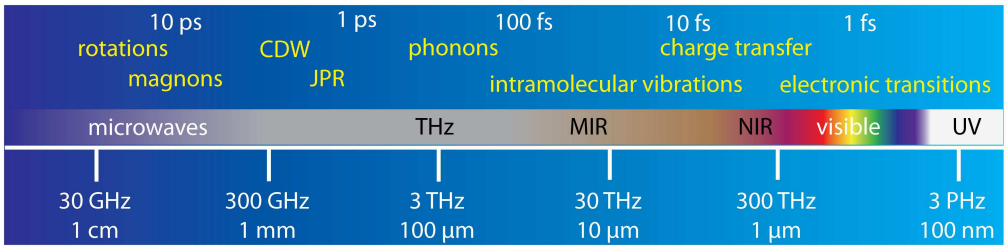

Figure 8.1: Excitations: Distribution of low-energy quasiparticles in condensed-matter systems over the optical spectral range. Reproduced from [20].

For targeted resonant excitations of these collective long-wavelength modes in the mid-infrared (MIR) and THz ranges, optical parametric amplification (OPA) systems and THz systems will be used. In addition to resonant energy transfer to the low-energy degrees of freedom, the electromagnetic field of the pump pulse can be used to directly drive ferroelectric polarization or magnetism in complex materials. In order to perform such types of pump–probe time-resolved experiments, optical pulses—with a field varying on a time scale longer than the duration of the probe pulse and with the field phase-locked with respect to the pulse envelope—will be generated using the same OPA and THz optical systems.

8.1 Overview

The Optical Lasers group (WP78) is currently developing a general pump–probe laser that will be available to all instrument groups [26]. Different pulse specifications and intrinsic burst repetition rates (8.2) are foreseen according to the European XFEL pulse structure.

Operation modes of the SASE3 central optical laser system

High repetition rate operation (PP mode)

- 10 Hz burst, 0.6% duty cycle
- 1–4.5 MHz intra-burst, “pulse on demand"
- 15, 30, 50, 100 fs
- 0.2–1 mJ per pulse, ca. 800 nm

Low repetition rate operation (MAL mode)

- 10 Hz burst, 0.6% duty cycle
- 200 kHz intra-burst, “pulse on demand"
- sub-20 fs at 800 nm, or 0.8 ps and 0.5 ns at 1030 nm
- > 3 mJ per pulse at 800 nm, or 100 mJ per pulse at 1030 nm

The optical laser system will be located inside of the SASE3 optical laser hutch. The optical laser beam will then be routed via evacuated beam transport tubes to the various instruments by broadband dielectric mirrors. The baseline operation modes will be extended in the SCS laser hutch where up- and down-frequency conversion systems will be assembled on optical tables before delivering the beam to the SCS experiment hutch. The SCS THz generation setup will be located near the experiment chamber or sample interaction point because of the large beam divergence and beam focusing requirements.

Up- and down-frequency conversion components in the SCS laser hutch

- 800 nm optical laser
- Second- and third-harmonic generation (SHG and THG) based on optical crystals (beta barium borate, BBO) will be used to obtain 400 nm and 266 nm wavelengths
- Optical parametric amplifier (OPA) will be used to generate tunable-wavelength optical pulses in the range of 400 nm – 3 µm and 4–20 µm
- THz generation setup will be realized using appropriate optical elements and crystals

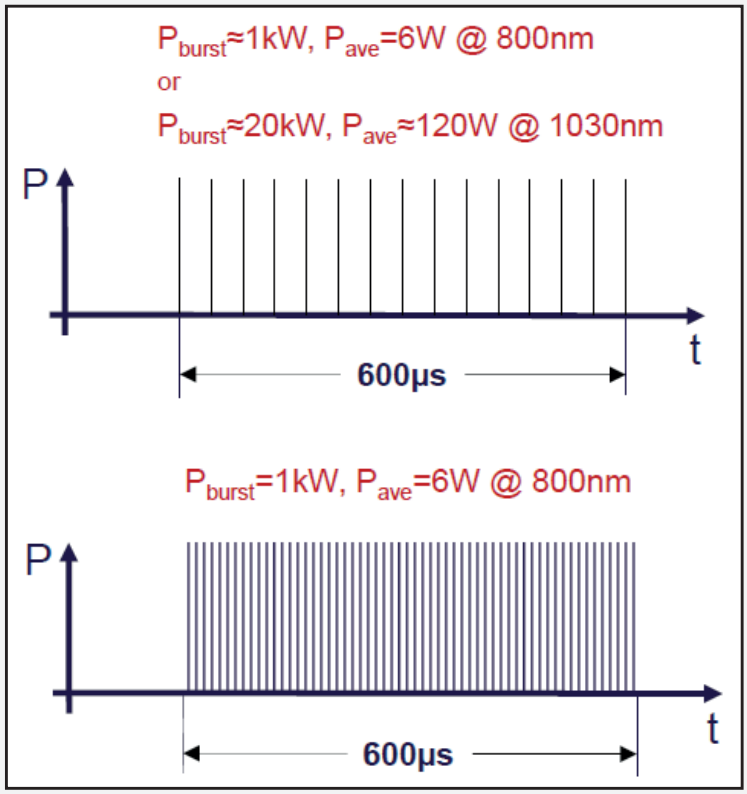

Figure 8.2: MAL mode of the SASE3 laser system: Low repetition rate pulse train at 800 nm or 1030 nm wavelength.

8.2 Central SASE3 optical laser system

The pump–probe laser system is based on a high-energy non-collinear optical parametric amplifier (NOPA, [6]). An ultrastable fibre seed laser is synchronized by the general European XFEL synchronization system and drives the amplification process. Its pulses are launched through a long delay stage that compensates jitter and drifts in the laser system and permits temporal overlap between X-rays and optical laser. A fibre-based pre-amplifier modifies and splits this signal to enable white-light generation in one arm and high-energy chirped-pulse amplification in a second arm. The high-energy pulses of the amplifier chain can either be directly sent to the experiment or utilized to drive the parametric process. For this, the fundamental wavelength has to be converted to double frequency (SHG). On the other hand, the white-light signal should be pre-chirped by dispersive mirrors and spatially and temporally overlapped in non-linear crystals. Depending on the demanded energy and repetition rate, four NOPA stages can be employed.

The pump–probe laser will be synchronized to the European XFEL synchronization network (Figure 8.3). To this end, a synchronization fibre link will be installed in the SASE3 optical laser hutch (SASE3.LAS). Depending on the connection stability (i.e. temperature drifting), it might need to be actively stabilized by a feedback method. The stable optical signal will then be optically cross-correlated with the seed laser oscillator of the pump–probe laser to align its clocking with the synchronization system and the other European XFEL units. The Optical Lasers group (WP78) aims for a final jitter between pump–probe and synchronization link below 20 fs. To fulfil specific user requirements, the SCS group will need to change the pulse properties of the optical laser in some cases. In collaboration with WP78, a general layout has been conceived that will give great flexibility with respect to these demands.

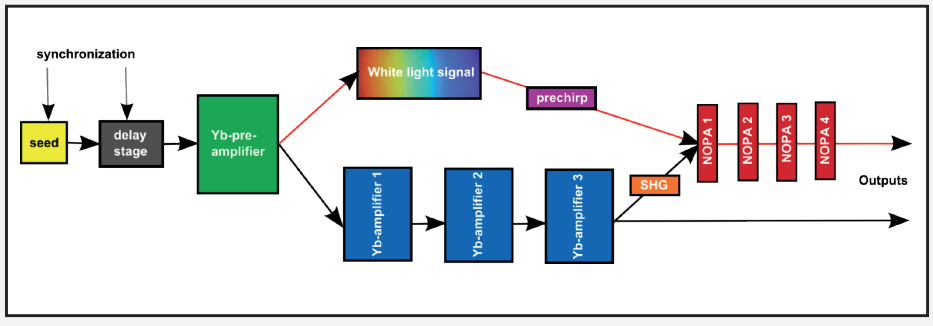

Figure 8.3: Optical pump–probe laser synchronization

The typical laser requirements can be divided into a default case and an optional case.

8.2.1 Case I: Short pulses (default)

In the default case, the SASE3 optical laser system will generate very short pulses (in steps: 15 fs, 30 fs, 50 fs, 100 fs) at 800 nm with the option to generate second-harmonic (SHG: 400 nm) and third-harmonic (THG: 266 nm) radiation to allow for a shorter wavelength range. Apart from that, a commercial broadband device (TOPAS by Light Conversion Ltd.) will provide access to a very broadly tunable spectrum with wavelengths ranging from ca. 400 nm to several micrometres. Jitter and coincidence management will be mandatory to achieve adequate time resolution for the experiments. This requires a thorough treatment of dispersion and non-linearity to provide the shortest pulse duration on the sample inside the chamber.

8.2.2 Case II: Long pulses (optional)

Long pulses in the range of either 800 fs (compressed) or 500 ps (uncompressed) with highest possible pulse energies up to 100 mJ (200 kHz) will be available on request. Additional SHG and THG units could complement this setup.

8.3 SCS laser hutch conceptional layout and frequency conversion

This section introduces the current optical layout. Distinct parts and components are currently undergoing evaluation in close collaboration with the Optical Lasers group (WP78) and may be subject to changes. Figure 8.4 on the next page illustrates the most recent layout.

For repetition rates below 1 MHz, pulses will be delivered via a six-inch vacuum pipe (vacuum 10^{-10} mbar). The beam diameter at the exit window will be around 30 mm. For higher repetition rates, pulses will be send through a two-inch pipe (red beam in Figure 8.4 on the facing page) with a 10 mm beam diameter at the same vacuum pressure. At the exit of the delivery beam pipe, a remotely controllable attenuator might be used to tweak the input power and energy. This attenuator would consist of a half-wave plate in combination with a thin-film polarizer (TFP) pair.

However, in the case of 15 fs pulse duration, the coating on the TFP demands for a very advanced dispersion design. Yet, it is not clear whether the manufacturers can provide such a design. Alternatively, exchangeable reflective optics (i.e. output coupler) could permit a gradual attenuation, or splitters could be used.

In Case I, the beam will be picked up by a displaceable mirror from either entrance beamline. After relay imaging, it will be divided into a coincidence arm and a pump–probe arm. The attenuator/splitter ($\lambda/2$ wave plate and TFPs) would permit a continuously tunable energy splitting.

As previously mentioned, this concept is currently subject to evaluation as TFPs might introduce too much chirp (pulse broadening). Delay Line III is responsible for pump–probe scanning, whereas Delay Line I and the optional Delay Line II are quasi-fixed translation configurations to compensate any coarse path differences between pump–probe and temporal overlap arm. Such path differences might occur when changing the instrument setup between experiments. To ensure that pump–probe and coincidence beam can be individually selected, they are sent into separate delivery pipes at the entrance to the instrument hutch.

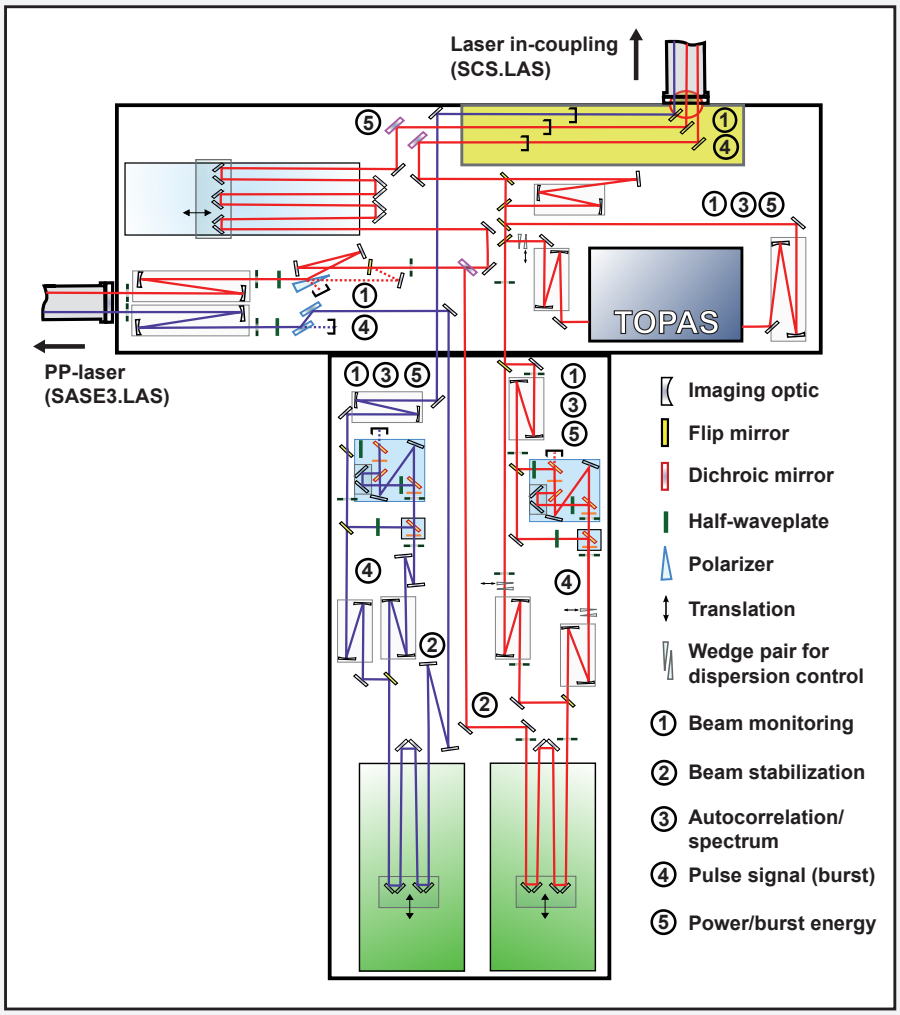

Figure 8.4: Principle and schematic drawing of optical setup in the SCS laser hutch. (Blue optical path) Long pulse delivery with high pulse energies at 1030 nm. (Red optical path) Short pulse delivery at 800 nm.

Displaceable SHG and THG units offer frequency conversion and wave plates ($\lambda/2$, $\lambda/4$) serve as polarization control for the actual experiment, but also for THG (i.e. type I-critical phase matching in BBO). For slightly longer pulses between 20 fs and 30 fs, commercial broadband devices, such as TOPAS (Light Conversion Ltd), might be utilized to significantly increase the wavelength range.

All reflective mirrors must be equipped with zero-dispersion coatings for the respective wavelength operation regime. In the current design, the 15 fs long pulse will enter the SCS laser hutch negatively chirped to 300 fs pulse duration. Its dispersion is

conjugated to fused silica. By propagating through fused silica components with predetermined length, the pulse will be compressed to the 15 fs bandwidth limit (reached inside the chamber after entrance window). The amount of fused silica required will be on the order of 30–40 mm thickness. A pair of fused silica wedges will make fine-tuning possible in each arm. The drawing actually does not include any additional fused-silica imaging optics between the setup and the instrument vacuum chamber (i.e. for focusing).

For SHG, THG, and TOPAS operation, the turning mirrors will need to be changed to optimize the dispersion and reflection efficiency. The actual arrangement of components is not predetermined and might be changed at a later stage.

In Case II, the setup poses much lower constraints on dispersion. On the other hand, mirrors need to have sufficient damage thresholds. In Figure 8.4 on the previous page, the purple dotted line represents the optical path of the long pulses at 1030 nm. Optional SHG, THG, and polarization control units may be inserted for completion.

The numbers in Figure 8.4 on the preceding page indicate monitoring and control locations where pulse properties should be analysed and corrected if appropriate. Some of these observation points are locally flexible, whereas others might have to be fixed (i.e. beam stabilization in red beamline after delay lines).

The whole assembly will be mounted on an optical table that is mechanically damped and possibly passively stabilized against thermal drifting. A sealed box will protect the setup against any potential external disturbances. The beam delivery pipes will not contain any mirror mounts (purely transmitting) and will be decoupled from the optical configuration to ensure maximum stability. The design is considered as initial, and further extensions may be added at a later stage. Possible changes could include simultaneous operation of different pulses (length, wavelength, spectra, beam size, etc.).

The X-ray beam and the optical laser beam will be brought into the experiment chamber through the laser in-coupling chamber to realize a collinear geometry of the X-ray and optical beams in the pump–probe experiments and minimize time averaging over the beam's spots on the sample. The laser in-coupling mirror chamber will have movable mirror mounts that will allow for mounting several mirrors at 45 degrees with respect to the X-ray beam to cover the wavelength range of the optical laser system. Easy access to the mirror mounts to exchange mirrors is vital as well. Each mirror will have a hole in its center tilted at 45° for transporting the X-rays.

8.4 Laser in-coupling with differential pumping section

The optical laser beam is finally delivered to the SCS experiment hutch. The laser in-coupling section of the SCS instrument is located downstream of the solid attenuator and the differential pumping section to the KB optics tank and upstream of the last beamline valve before the SCS instrument. A manipulator stage will be equipped with a set of optical mirrors covering the wide range of optical wavelength and placed in a vacuum chamber at 45° of the mirror surface to the X-ray propagation direction. For the collinear alignment of the X-ray and optical beams, the X-ray beam passes through a machined hole in the centre of the optical mirror. The laser in-coupling chamber is mounted on a optical breadboard, which picks up the optical beam from the SCS laser hutch and brings the optical beam to the height of the SCS beamline. The optical breadboard will host various optical diagnostics to characterize the pulse length, intensity, and beam size parasitically prior to delivery of the optical beam to the sample interaction point in the SCS instrument. A long-distance microscope will be used to monitor the beam's spot sizes and spatial overlap of the beams on the sample in the experiment chamber.

9 DAQ and control systems

The data acquisition (DAQ) and control systems will be used to configure, control, and monitor the SCS instrument as well as to control the data acquisition of the detectors. It is foreseen that common interfaces will be realized for all beamline devices and detectors. The DAQ and control systems of the SCS instrument will use a common European XFEL instrument architecture. The implementation is currently under development by the DAQ and Control Systems group (WP76).

The DAQ, data management, and scientific computing systems will have a layered architecture with well-defined interfaces to increase flexibility in implementing devices, upgrades, and further developments. Furthermore, the architecture anticipates partitioning of the layers into slices associated with groups of detectors.

Control and DAQ architecture consisting of six layers is foreseen

- **Front-end electronics (FEE)**
  Will record and control data from the detectors.

- **Front-end interface (FEI)**
  Will provide interface between the detector FEE and timing, control, readout systems, etc. Will also provide the interface for the beamline control system.

- **PC layer**
  Will receive data from the detector FEI and perform processing and formatting.

- **Online storage layer**
  Will be used for temporal storing of the data and to provide them for preliminary analysis before storing the good-quality data in the offline storage.

- **Offline storage**
  Will be used for secure long-term storage of the users' data.

- **Offline analysis clusters (OACs)**
  Will be used for offline analysis of the users' data.

The SCS control hutch will be equipped with European XFEL status screens to monitor the machine and X-ray beam parameters, as well as status screens for beamline valves and vacuums, beamline X-ray optics parameters, optical laser systems, etc.

The main types of data that will be recorded during the experiments are:

- **Scalars**
  Values recorded from point detectors (e.g. diodes)

- **Vectors**
  High-speed digitizers will be used to record the time traces from the point detectors

- **2D arrays**
  Images of 2D detectors (e.g. CCD cameras)

Detectors, motors, pumps, gauges, sensors, and actuators will be chosen such as to ensure a maximum device standardization at European XFEL.

Beckhoff hardware, programmable logic controllers (PLCs), and terminals will be used for the beamline controls. A firmware will be developed to control the SCS instrument detectors and controls: stepping motors, pump controllers, gauges, etc. The Karabo framework will be used to interface with Beckhoff hardware systems. Graphical user interface (GUI) and Python scripting will be developed on top of the Karabo framework.

The main features of the Karabo framework are:

- Centric framework based on devices linked via message broker (see Figure 9.1 on the next page)

- Various physical objects, control, and analysis tasks are defined as devices

- Control system of Karabo can be realized with XST/XML

The HDF5 file format and the Linux operating system are foreseen as data container and main platform, respectively. The high volume of data recorded in user experiments will be stored locally on the European XFEL site and processed by users remotely.

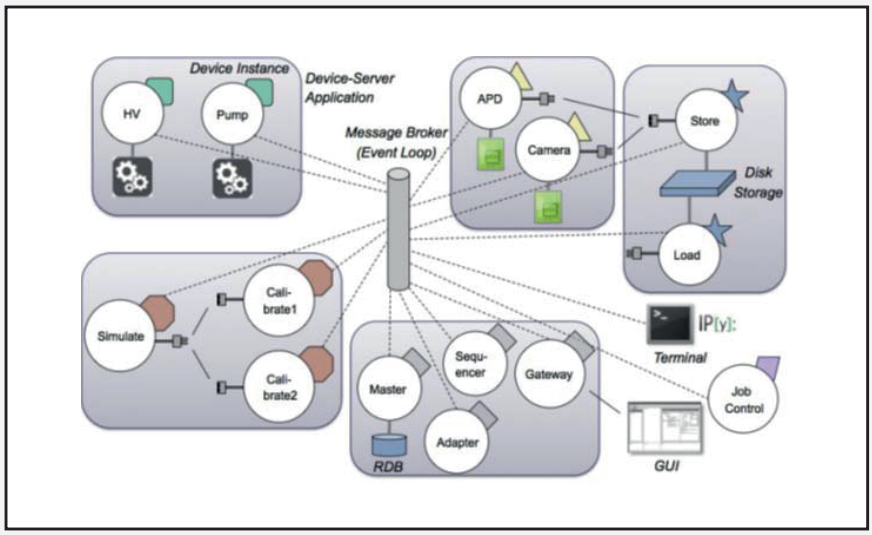

Figure 9.1: Schematic representation of the Karabo framework.

10 Summary and timeline

In summary, the overall requirements of the SCS instrument have been addressed and are largely satisfied in this conceptual design. The X-ray beam transport system has been reviewed, and concepts for short-pulse preservation in monochromatic mode have been discussed and presented. The requirements for the figure quality of the KB refocusing optics with bent mechanism have been detailed. A technical realization and the choice of bent mechanism will be subject to the technical design and consultations of potential vendors in 2013 in order to prepare for tender (long lead time item).

An X-ray beam split and delay line concept has been presented. The project is still in an early stage and needs further refinement. The main issues are beam pointing stability and reproducibility of time delays by mirror translations over more than 1 m. Those issues will be addressed in the TDR in 2014.

The requirements of the detectors and their respective sample–detector distances are satisfied by the presented instrument conceptual design and the overall dimension of the SCS hutch for typical sample sizes that are investigated by CXDI and time-resolved X-ray diffraction. A detailed investigation of the CXDI performance with given detectors will be part of the forthcoming SCS TDR.

The space requirements for the hRIXS spectrometer of the user consortium are fulfilled. The final specifications of attainable energy resolutions of hRIXS in connection with the soft X-ray monochromator will be concluded in a timely fashion. The floor requirements in terms of slope errors and surface finish remain to be solved. In particular, the access to the sample interaction point across the delicate floor areas has to be settled.

The space constraints in the SCS experiment hutch make it difficult to host the two large-scale instrumentations—the baseline SCS instrumentation and the hRIXS spectrometer—near the sample interaction point. For this reason, both instrumentations need to be retractable from this area as needed. The SCS experiment hutch currently provides enough space for both instrumentations but very limited space for add-on instrumentations.

The timeline is detailed in Figure 10.1 on the following page. The day-one operation of the baseline instrumentation will facilitate soft X-ray imaging (CXDI) of fixed-target

nanostructures at 10 Hz using the FastCCD detector and time-resolved spectroscopy and coherent scattering employing a quarter of the DSSC detector.

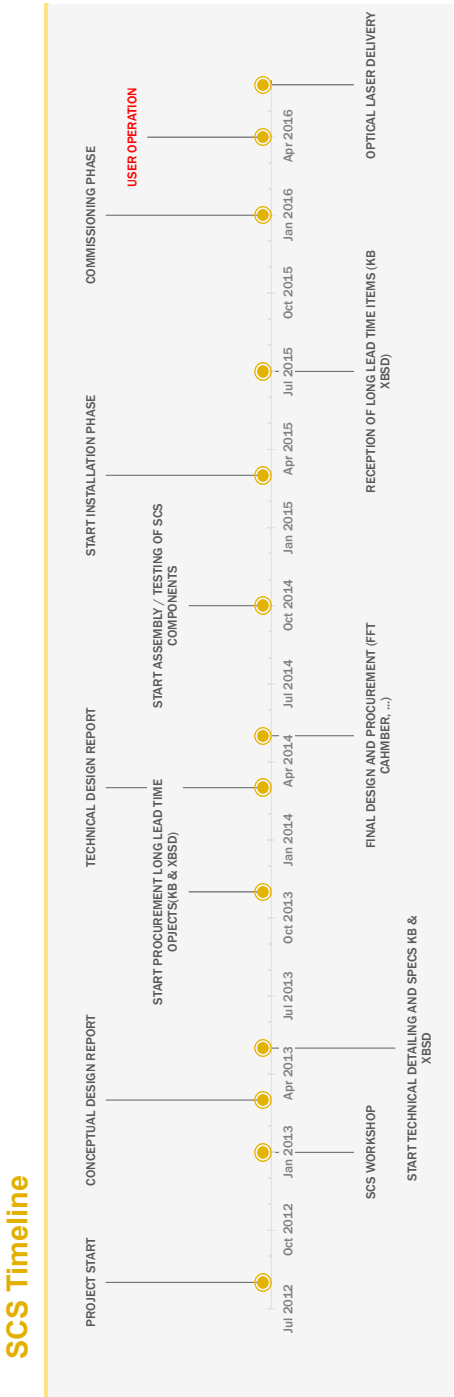

Figure 10.1: Current SCS timeline for design, assembly, installation, and commissioning until user operation

A SASE3 source parameterization

Table A.1 lists the coefficients of the source parameterization given in Section 2.1, "SASE3".

Table A.1: SASE3 source parameterization coefficients

Operation mode	10.5 GeV	14 GeV	17.5 GeV
s_{10}	4.5	3.8	3.5
s_{11}	3.5	3.4	2.9
s_{20}	2.77×10^4	4.562×10^4	6.151×10^4
s_{21}	-1.60	-2.09	-1.90
e_{10}	-0.09	0.00	-0.01
e_{11}	2.6	2.5	3.0
e_{20}	22.14	34.84	54.60
e_{21}	-0.80	-1.31	-1.54
w_1	0.11	0.09	0.09
w_{20}	42.4	65.1	68.0
w_{21}	-0.69	-0.542	-0.36
θ_0	-2.6	-2.1	-1.3
θ_{10}	14.7	15.0	14.6
θ_{11}	-4.11	-4.42	-4.36

B Grating performance under pulsed and shaped sources

This appendix derives the energy resolutions of the grating for different pulsed illuminations and considers the respective pulse stretching. The minimum bandwidth–duration product is given at the end.

B.1 General grating-induced pulse stretching of a δ-like pulse

The optical geometry and definitions for the derivation are shown in Figure B.1.

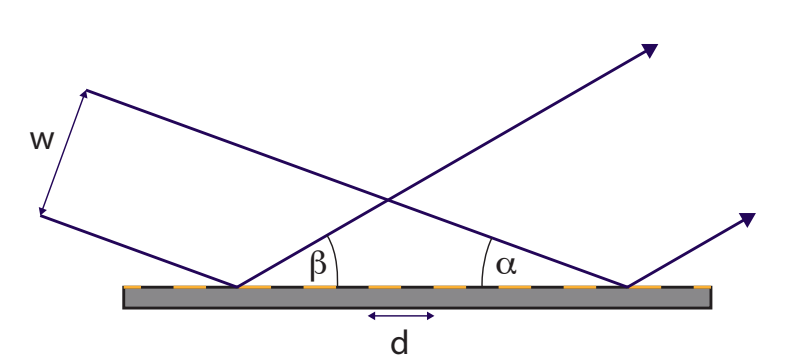

Figure B.1: Optical geometry and definitions used for the derivation of the grating properties

The incident wavefront of width w illuminates the grating with periodicity $d_0 = 1/(d \sin\alpha)$. Here, the incident angle is α, and the outgoing angle is β. The path length difference of diffracted waves between two lines separated by distance d is a multiple of the wavelength λ for constructive interference, which leads to the grating equation:

$$m\lambda = d(\cos\alpha - \cos\beta) \ . \tag{B.1}$$

where m is the diffraction order.

The maximum delay length or corresponding delay time occurs over the width of the incident wavefront. This condition gives, for the first order diffraction of the grating, $m = 1$,

$$\Delta l = c\Delta\tau \equiv w(\cos\alpha - \cos\beta)/\sin\alpha = w\lambda d_0 \tag{B.2}$$

where c is the speed of light. In fact, the overall pulse stretching is given by the variance of time delays $\Delta\tau_{\mathrm{rms}}$ occurring between all illuminated grating lines according to

$$\Delta\tau_{\mathrm{rms}} = \sqrt{\int \left(\xi - \langle\xi\rangle\right)^2 t(\xi)\mathrm{d}\xi} = \frac{1}{c} w_{\mathrm{rms}} d_0 \lambda \tag{B.3}$$

The variance of the beam profile will be determined for the two cases that are discussed in the following sections.

B.2 Top-hat illumination of a grating

The absolute efficiency of the grating is not of interest here, and the calculation is done for first order only (sinusoidal grating). In Fourier optics, the transmissivity of arbitrary amplitude may then take the form

$$t = \cos(2\pi d_0 \xi)\mathrm{rect}(\xi/w) \tag{B.4}$$

where a top-hat illumination envelope, $I = I_0\mathrm{rect}(\xi/w)$, is assumed. This condition is given when the monochromator is operated with a narrow entrance slit. The intensity distribution in the image plane (i.e. exit slit of the monochromator) is

$$\begin{aligned} I_{\mathrm{exit}} &\propto |F[t]|^2 = |F[\cos(2\pi d_0\xi)] \otimes F[\mathrm{rect}(\xi/w)]|^2 \\ &= \left|\left\{\tfrac{1}{2}[\delta(d_x - d_0)] + \delta(d_x + d_0)\right\} \otimes \{w\mathrm{sinc}(wd_x)\}\right|^2 \\ &= \left|w\left\{\mathrm{sinc}[wd_x] + \tfrac{1}{2}\mathrm{sinc}[w(d_x - d_0)] + \tfrac{1}{2}\mathrm{sinc}[w(d_x + d_0)]\right\}\right|^2 \end{aligned} \tag{B.5}$$

showing the zeroth-order and first-order diffraction peaks of the grating. In the image plane, the sampling is $d_x = \frac{y}{\lambda z}$ where $z = y/\sin\beta$ is the distance of the grating to the image plane. The overlap between the orders is negligible when a sufficient number of lines are illuminated. In this case, the first-order peak takes the form

$$I_{\mathrm{exit}}^{1\mathrm{st}} \propto \tfrac{1}{4}\mathrm{sinc}^2[w(d_x - d_0)] = \tfrac{1}{4}\mathrm{sinc}^2[w(\tfrac{\sin\beta}{\lambda} - d_0)] \tag{B.6}$$

The position of the first-order peak can be found at sinc[0] and the dispersion of the grating at given angle α follows as

$$\sin\beta/\lambda - d_0 = 0 \quad \Rightarrow \quad \left.\frac{\partial\lambda}{\partial\beta}\right|_{\alpha} = \frac{\cos\beta}{d_0} \tag{B.7}$$

Using the small-angle approximation, the FWHM of the central peak of the sinc function is

$$\frac{w\Delta\beta}{\lambda} \simeq 4\ln 2/\pi = 2c_B \tag{B.8}$$

with $c_B = \frac{2\ln 2}{\pi} = 0.441$. From this, the resolving power that is given by the line spread function of the grating follows by using the dispersion relation Equation B.7:

$$\frac{E}{\Delta E} = \underline{\frac{\lambda}{\Delta\lambda} = \frac{wd_0}{2c_B}} = \frac{1}{2c_B}N \simeq 1.13 \times N\,. \tag{B.9}$$

The variance of the incident wavefront for a top-hat illumination (cf. Equation B.3 on the preceding page) on an equally spaced line grating can be derived by running over all possible imposed delays

$$w_{\text{rms}}^2 = \frac{1}{N^2}\sum_{i=1}^{N}\sum_{j=1}^{N}\frac{1}{2}(\xi_i - \xi_j)^2 = \frac{\Delta\xi^2}{N^2}\sum_{k=1}^{N}\frac{k(k-1)(2k-1)}{6} \tag{B.10}$$

where $\Delta\xi = \xi_n - \xi_{n-1}$ is the line spacing in the incident propagation direction, and $w = N\Delta\xi$ is the full beam size. For illumination of a sufficient number of lines $N > 15$, this sum can be approximated by

$$\underline{w_{\text{rms}}^2 \simeq \frac{N}{4}\frac{\Delta\xi^2}{N^2}\frac{N(N-1)(2N-1)}{6} = \Delta\xi^2\left(\frac{1}{12}N^2 - \frac{1}{8}N + \frac{1}{24}\right) \approx \frac{w^2}{12}} \tag{B.11}$$

The minimum bandwidth–duration product can now be derived by multiplying (B.9) by λ and by using the expression for the pulse stretching Equation B.3 on the previous page:

$$\frac{E\lambda}{\Delta E} = \frac{\lambda wd_0}{2c_B} = \frac{\sqrt{12}\lambda w_{\text{rms}}d_0}{2c_B} \quad \Leftrightarrow \quad \frac{hc}{\Delta E} = \frac{\sqrt{12}c\Delta\tau_{\text{FWHM}}}{4c_B\sqrt{2\ln 2}} \tag{B.12}$$

This results in a minimum bandwidth–duration product of

$$\underline{\Delta E\Delta\tau = 2\sqrt{\frac{2\ln 2}{3}}hc_B = 1.36hc_B} \tag{B.13}$$

B.3 Gaussian illumination of a grating

The calculation follows the same steps as above. The incident beam profile is now given by

$$I = I_0 \exp(-\tfrac{\xi^2}{2w_{\mathrm{rms}}^2}) = I_0 \exp\left(-\pi \frac{\xi^2}{w_{\mathrm{FWHM}}^2/2c_B}\right), \tag{B.14}$$

and the transmissivity may be expressed as

$$t = \cos(2\pi d_0 \xi) \exp\left(-\pi \frac{\xi^2}{w_{\mathrm{FWHM}}^2/c_B}\right) \tag{B.15}$$

where $F\left\{\exp[-\pi\frac{\xi^2}{\sigma^2}]\right\} = \sigma \exp[-\pi d_x^2 \sigma^2]$. The intensity distribution of the first-order peak in the image plane is readily given by

$$\begin{aligned} I_{\mathrm{exit}}^{1\mathrm{st}} \propto |F[t]|^2 &= \frac{w_{\mathrm{FWHM}}^2}{c_B} \exp\left[-2\pi \frac{(d_x - d_0)^2}{c_B/w_{\mathrm{FWHM}}^2}\right] \\ &= \frac{w_{\mathrm{FWHM}}^2}{c_B} \exp\left[-\pi \frac{(\sin\beta - \frac{d_0}{\lambda})^2}{\frac{1}{2}\lambda^2 c_B/w_{\mathrm{FWHM}}^2}\right] \end{aligned} \tag{B.16}$$

from where the width of the first-order peak (FWHM)

$$\Delta\beta_{\mathrm{FWHM}}^2/2c_B = \tfrac{1}{2}\lambda^2 c_B/w_{\mathrm{FWHM}}^2 \quad \Rightarrow \quad \Delta\beta = c_B \frac{\lambda}{w_{\mathrm{FWHM}}} \tag{B.17}$$

is obtained. Using the dispersion relation, Equation B.7 on the facing page, the resolving power represented by the line spread function of the grating follows as

$$\underline{\frac{\lambda}{\Delta\lambda_{\mathrm{FWHM}}} = \frac{w_{\mathrm{FWHM}} d_0}{c_B}} \simeq 2.27 N_{\mathrm{FWHM}} = 5.34 N_{\mathrm{rms}} \tag{B.18}$$

and the minimum bandwidth–duration product for $\Delta\tau_{\mathrm{FWHM}} = \frac{1}{c} N_{\mathrm{FWHM}} \lambda$ can be expressed as

$$\underline{\Delta E \Delta\tau = h c_B} \tag{B.19}$$

C Physical quantities, symbols, and conversion factors

It is convenient to express the physical quantities in typical dimensions of the wavelength λ [nm], pulse durations τ [fs], and photon energies E [eV].

Table C.1: Physical quantities and symbols in convenient units

Symbol	Physical quantity	Equivalent	Numerical value
h	Planck's constant		4.136 eV · fs
c	Speed of light	$1/\sqrt{\epsilon_0 \mu_0}$	299.8 nm/fs
ε_0	Dielectric constant		5.527×10^{-2} e / (V · nm)
m_e	Electron mass		5.686 eV · fs^2/nm^2
$E_{\mathrm{ph}} \cdot \lambda$	Relation between wavelength and photon energy	$h \cdot c$	1239.97 nm · eV
c_{B}	Constant	$2 \ln 2/\pi$	0.441

D Abbreviations

ARPES	angle-resolved photoelectron spectroscopy
ARTOF	angle-resolved time-of-flight spectrometer
B_4C	boron carbide, extremely hard ceramic material
BBO	beta barium borate, nonlinear optical material
CCD	charge-coupled device, 2D array detector
CDR	conceptual design report
CXDI	coherent X-ray diffraction imaging
DAQ	data acquisition system
DEPFET	Depleted P-Channel Field Effect Transistor
DESY	Deutsches Elektronen-Synchrotron in Hamburg and Zeuthen, Germany
DSSC	DEPFET Sensor with Signal Compression Detector
FFT	forward-scattering fixed-target chamber of the SCS instrument
FLASH	Free-Electron Laser in Hamburg, XUV-XFEL facility at DESY, Germany
FTH	Fourier transform holography
FWHM	full width at half maximum
HAMP	huge-aperture open multiplier
HDF5	Hierarchical Data Format Version 5
IF	intermediate focus (new source point)
hr-	high energy resolution technique
hRIXS	Heisenberg Resonant Inelastic X-Ray Scattering instrument
IR	infrared radiation
KB	Kirkpatrick-Baez X-ray focusing design of reflecting mirrors
LCLS	Linac Coherent Light Source, XFEL facility at SLAC in Menlo Park, California
LSF	line spread function
MIR	mid-infrared radiation
NLXS	nonlinear X-ray spectroscopy
NOPA	noncollinear optical parametric amplifier

OPA	optical parametric amplifier
PES	photoelectron spectroscopy
pink (beam)	full bandwidth of X-ray laser radiation
PLC	programmable logic controller
PSD	power spectral density
REXS	resonant elastic X-ray scattering
RIXS	resonant inelastic X-ray scattering
RMS	root mean square
RP	resolving power
SASE	self-amplified spontaneous emission (generation of X-ray laser radiation)
SASE3.LAS	central optical laser system for the SASE3 instruments
SCS	Spectroscopy and Coherent Scattering instrument at European XFEL
SCS.CTR	control room of the SCS instrument
SCS.EXP	experiment hutch of the SCS instrument
SCS.LAS	optical laser hutch of the SCS instrument
SCS.RCK	rack room/gallery of the SCS instrument
SHG	second-harmonic generation
SLAC	SLAC National Accelerator Laboratory in Menlo Park, California
SMA	Subminiature Version A coaxial cable connector
SQS	Small Quantum Systems instrument at European XFEL
SPB	Single Particles, clusters, and Biomolecules instrument at European XFEL
SXR	Soft X-Ray Materials Science instrument at LCLS
TDR	technical design report
TFP	thin-film polarizer
THG	third-harmonic generation
THz	terahertz radiation
TOF	time-of-flight spectrometer
TOPAS	tunable optical parametric amplifier system
tr-	time-resolved technique
UC	user consortium at European XFEL
UHV	ultrahigh vacuum

UV	ultraviolet radiation
VLS	variable line spacing grating
WP	work package at European XFEL
XBPM	X-ray beam position monitor, beam position diagnostics
XBSD	X-ray beam split and delay line
XGMD	X-ray gas monitor detector, beam intensity diagnostics
XFEL	X-ray free-electron laser
XPCS	X-ray photon correlation spectroscopy
XUV	extreme ultraviolet radiation
YAG	yttrium aluminium garnet, (cerium-doped) scintillator

E Acknowledgements

This report was written by Andreas Scherz and Oleg Krupin with contributions from Natalia Gerasimova (soft X-ray monochromator), Liubov Samoylova (wavefront propagation simulations), Jens Buck (photon energy and polarisation monitor), Guido Palmer (optical laser delivery), and Nigel Poolton (Pulsed magnets).

We would like to thank the members of the SCS Advisory and Review Team for their assessment of the SCS conceptual design and constructive suggestions to the open issues:

- Jan Lüning (chair)
- Stefan Eisebitt (SAC member)
- William F. Schlotter
- Gerhard Grübel
- Wilfried Wurth
- Giacomo Ghiringhelli
- Nina Rohringer

Their effort will contribute to the next stage, the technical design of the SCS instrument.

Last but not least, we would like to thank Serguei Molodtsov, Harald Sinn, Daniele La Civita, Monica Turcato, Markus Kuster, Jan Grünert, Kai Tiedtke, Michael Meyer, Adrian Mancuso, Andrew Aquila, Klaus Giewekemeyer, Gianluca Geloni, and all colleagues at European XFEL for their endurance in invaluable and numerous discussions that contributed to and shed light on various aspects of the SCS conceptual design.

Bibliography

[1] M. Altarelli, R. Brinkmann, C. M., et al. (eds.): “Technical Design Report: The European X-Ray Free-Electron Laser”, DESY Report 2006-097 (2006) doi:10.3204/DESY_06-097

[2] L. J. P. Ament, M. van Veenendaal, T. P. Devereaux, et al.: “Resonant inelastic x-ray scattering studies of elementary excitations”, Reviews of Modern Physics **83**, 705 (2011) doi:10.1103/RevModPhys.83.705

[3] M. Beye, O. Krupin, G. Hays, et al.: “X-ray pulse preserving single-shot optical cross-correlation method for improved experimental temporal resolution”, Applied Physics Letters **100**, 121108–4 (2012) doi:10.1063/1.3695164

[4] M. R. Bionta, H. T. Lemke, J. P. Cryan, et al.: “Spectral encoding of x-ray/optical relative delay”, Optics Express **19**, 21855–21865 (2011) doi:10.1364/OE.19.021855

[5] J. Buck, et al.: “Time-of-flight photoemission spectroscopy from rare gases for non-invasive, pulse-to-pulse X-ray photon diagnostics at the European XFEL”, X-Ray Free-Electron Lasers: Beam Diagnostics, Beamline Instrumentation, and Applications, San Diego, California, August 12, 2012, Proc. of SPIE 8504, 85040U (2012) doi:10.1117/12.929805

[6] G. Cerullo, S. D. Silvestria: “Ultrafast optical parametric amplifiers”, Rev. Sci. Instrum. **74**, 1 (2003) doi:10.1063/1.1523642

[7] H. N. Chapman, A. Barty, M. J. Bogan, et al.: “Femtosecond diffractive imaging with a soft-X-ray free-electron laser”, Nat Phys **2**, 839–843 (2006) doi:10.1038/nphys461

[8] E. Church, P. Takacs: “Specification of glancing- and normal-incidence x-ray mirrors”, Opt. Engineering **34**, 353 (1995) doi:10.1117/12.196057

[9] L. Condat, D. Van De Ville, B. Forster-Heinlein: “Reversible, Fast, and High-Quality Grid Conversions”, Image Processing, IEEE Transactions on **17**, 679–693 (May 2008) doi:10.1109/TIP.2008.919361

[10] W. Decking, T. Limberg: “European XFEL Post-TDR Description”, XFEL.EU TN-2013-004-01, https://bib-pubdb1.desy.de/record/153594 (2013)

[11] D. Doering, Y. D. Chuang, N. Andresen, et al.: “Development of a compact fast CCD camera and resonant soft x-ray scattering endstation for time-resolved pump-probe experiments”, Review of Scientific Instruments **82**, 073303–8 (2011) doi:10.1063/1.3609862

[12] S. Eisebitt, J. Luning, W. F. Schlotter, et al.: “Lensless imaging of magnetic nanostructures by X-ray spectro-holography”, Nature **432**, 885–888 (2004) doi:10.1038/nature03139

[13] U. Fruhling, M. Wieland, M. Gensch, et al.: “Single-shot terahertz-field-driven X-ray streak camera”, Nat Photon **3**, 523–528 (2009) doi:10.1038/nphoton.2009.160

[14] C. Gahl, A. Azima, M. Beye, et al.: “A femtosecond X-ray//optical cross-correlator”, Nat Photon **2**, 165–169 (2008) doi:10.1038/nphoton.2007.298

[15] G. Geloni, V. Kocharyan, E. Saldin: “Circular Polarization Control for the European XFEL in the Soft X-Ray Regime”, DESY 11-096, https://bib-pubdb1.desy.de/record/89177 (2011)

[16] G. Geloni, V. Kocharyan, E. Saldin: “Self-seeding scheme for the soft X-ray line at the European XFEL”, DESY 12-034, https://bib-pubdb1.desy.de/record/95530 (2012)

[17] C. E. Graves, A. H. Reid, T. Wang, et al.: “Nanoscale spin reversal by non-local angular momentum transfer following ultrafast laser excitation in ferrimagnetic GdFeCo”, Nat. Mater. **12**, 293 (2013) doi:10.1038/nmat3597

[18] C. M. Günther, B. Pfau, R. Mitzner, et al.: “Sequential femtosecond X-ray imaging”, Nat. Photonics **5**, 99 (2002) doi:10.1038/nphoton.2010.287

[19] S. Hellmann, C. Sohrt, M. Beye, et al.: “Time-resolved x-ray photoelectron spectroscopy at FLASH”, New Journal of Physics **14**, 013062 (2012) doi:10.1088/1367-2630/14/1/013062

[20] M. C. Hoffmann, LCLS, SLAC National Laboratory, 2013

[21] R. Howells, D. Cambie, R. Duarte, et al.: “Theory and practice of elliptically bent x-ray mirrors”, Opt. Engineering **39**, 2000 (1995) doi:10.1117/1.1289879

[22] S. de Jong, R. Kukreja, C. Trabant, et al.: “‘Speed limit of the insulator–metal transition in magnetite”, Nat. Mater. (2013) doi:10.1038/nmat3718

[23] E. P. Kanter, B. Krässig, Y. Li, et al.: “Unveiling and Driving Hidden Resonances with High-Fluence, High-Intensity X-Ray Pulses”, Phys. Rev. Lett. **107**, 233001 (2011) doi:10.1103/PhysRevLett.107.233001

[24] A. Koch, M. Kuster, J. Sztuk-Dambietz, et al.: “Detector Development for the European XFEL: Requirements and Status”, Journal of Physics: Conference Series **425**, 062013 (2013) doi:10.1088/1742-6596/425/6/062013

[25] O. Krupin: “Temporal cross-correlation of x-ray free electron and optical lasers using soft x-ray pulse induced transient reflectivity”, Optics Express **20**, 11396–11406 (2012) doi:10.1364/OE.20.011396

[26] M. Lederer, M. Pergament, M. Kellert, et al.: “Pump-probe laser development for the European X-Ray Free-Electron Laser Facility”, X-Ray Free-Electron Lasers: Beam Diagnostics, Beamline Instrumentation, and Applications, San Diego, California, August 12, 2012, Proc. SPIE 8504, 85040L (2012) doi:10.1117/12.928961

[27] B. Li: “X-Ray Photon Temporal Diagnostics for the European XFEL”, XFEL.EU TN-2012-002-01, https://bib-pubdb1.desy.de/record/139588 (2012)

[28] J. Lüning, G. Grübel: *Report of Working Group III: Spin, charge and orbital dynamics in complex materials by resonant elastic scattering at the European XFEL*, 2009, http://www.xfel.eu/sites/site_xfel-gmbh/content/e63594/e63599/e81232/e65122/e76473/scs-wg-iii-report_eng.pdf

[29] A. Mancuso, A. Aquila, G. Borchers, et al.: "Technical Design Report: Scientific Instrument Single Particles, Clusters and Biomolecules (SPB)", XFEL.EU TR-2012-004 (2013) doi:10.3204/XFEL.EU/TR-2013-004

[30] S. Marchesini, S. Boutet, A. E. Sakdinawat, et al.: "Massively parallel X-ray holography", Nat Photon **2**, 560–563 (2008) doi:10.1038/nphoton.2008.154

[31] R. Mitzner, B. Siemer, M. Neeb, et al.: "Spatio-temporal coherence of free electron laser pulses in the soft x-ray regime", Opt. Express **16**, 19909 (2008) doi:10.1364/OE.16.019909

[32] B. F. Murphy, J Bozek, J. C. Castagna, et al.: "Split and Delay System for Soft X-ray Pump/Soft X-ray Probe Experiments at the LCLS Free Electron Laser", Journal of Physics: Conference Series **388**, 142003 (2012) doi:10.1088/1742-6596/388/14/142003

[33] B. Nagler, U. Zastraum, R. R. Fäustlin, et al.: "Turning solid aluminium transparent by intense soft X-ray photoionization", Nat. Phys. **183**, 693 (2009) doi:10.1038/nphys1341

[34] G. Ohrwall, P. Karlsson, M. Wirde, et al.: "A new energy and angle resolving electron spectrometer – First results", J. Electron Spectroscopy and Related Phenomena **183**, 125 (2011) doi:10.1016/j.elspec.2010.09.009

[35] B. D. Patterson: "Resource Letter on Stimulated Inelastic X-ray Scattering at an XFEL", SLAC-TN-10-02, http://slac.stanford.edu/pubs/slactns/tn04/slac-tn-10-026.pdf (2010)

[36] M. Porro, L. Andricek, S. Aschauer, et al.: "Development of the DEPFET Sensor With Signal Compression: A Large Format X-Ray Imager With Mega-Frame Readout Capability for the European XFEL", Nuclear Science, IEEE Transactions on **59**, 3339–3351 (Dec. 2012) doi:10.1109/TNS.2012.2217755

[37] N. Rohringer, D. Ryan, R. A. London, et al.: "Atomic inner-shell X-ray laser at 1.46 nanometres pumped by an X-ray free-electron laser", Nature **481**, 7382 (2012) doi:10.1038/nature10721

[38] A. Scherz, D. Zhu, R. Rick, et al.: "Nanoscale Imaging with Resonant Coherent X Rays: Extension of Multiple-Wavelength Anomalous Diffraction to Nonperiodic Structures", Physical Review Letters **101** (2008) doi:10.1103/PhysRevLett.101.076101

[39] A. O. Scherz: "Handbook of Nanophysics: Principles and Methods", in: K. D. Sattler (ed.), vol. 1, Handbook of Nanophysics (CRC Press 2010)

[40] W. F. Schlotter, R. Rick, K. Chen, et al.: "Multiple reference Fourier transform holography with soft x rays", Applied Physics Letters **89**, 163112 (2006) doi:10.1063/1.2364259

[41] E. Schneidmiller, M. Yurkov: “Photon Beam Properties at the European XFEL”, DESY Report 11-152, XFEL.EU TR-2011-006 (2010) doi:10.3204/DESY11-152

[42] M. M. Seibert, T. Ekeberg, F. R. N. C. Maia, et al.: “Single mimivirus particles intercepted and imaged with an X-ray laser”, Nature **470**, 78 (2011) doi:10.1038/nature09748

[43] S. Serkez, V. Kocharyan, E. Saldin, et al.: “Grating Monochromator for Soft X-ray Self-Seeding the European XFEL”, DESY 13-040, https://bib-pubdb1.desy.de/record/154225 (2013)

[44] F. Siewert, J. Buchheim, S. Boutet, et al.: “Ultra-precise characterization of LCLS hard X-ray focusing mirrors by high resolution slope measuring deflectometry”, Opt. Express, 4525–4536 (2012) doi:10.1364/OE.20.004525

[45] H. Sinn, M. Dommach, X. Dong, et al.: “Technical Design Report: X-Ray Optics and Beam Transport”, XFEL.EU TR-2012-006 (2012) doi:10.3204/XFEL.EU/TR-2012-006

[46] H. Sinn, J. Gaudin, L. Samoylova, et al.: “Conceptual Design Report: X-Ray Optics and Beam Transport”, XFEL.EU TR-2011-002 (2011) doi:10.3204/XFEL.EU/TR-2011-002

[47] F. Sorgenfrei, W. F. Schlotter, T. Beeck, et al.: “The extreme ultraviolet split and femtosecond delay unit at the plane grating monochromator beamline PG2 at FLASH”, Rev. Sci. Instrum. **81**, 043107 (2010) doi:10.1063/1.3374166

[48] J. Stöhr, H. C. Siegmann: *Magnetism: From Fundamentals to Nanoscale Dynamics* (Springer, Berlin / Heidelberg, 1st edition 2006)

[49] L. Strüder, S. Epp, D. Rolles, et al.: “Large-format, high-speed, X-ray pnCCDs combined with electron and ion imaging spectrometers in a multipurpose chamber for experiments at 4th generation light sources”, Nuclear Instruments and Methods in Physics Research Section A: Accelerators, Spectrometers, Detectors and Associated Equipment **614**, 483–496 (2010) doi:10.1016/j.nima.2009.12.053

[50] S. Tanaka, S. Mukamel: “Coherent X-Ray Raman Spectroscopy: A Nonlinear Local Probe for Electronic Excitations”, Phys. Rev. Lett. **89**, 043001 (2002) doi:10.1103/PhysRevLett.89.043001

[51] K. Tiedtke, J. Feldhaus, U. Hahn, et al.: “Gas detectors for x-ray lasers”, Journal of Applied Physics **103**, – (2008) doi:10.1063/1.2913328

[52] F. van der Veen, F. Pfeiffer: “Coherent x-ray scattering”, Journal of Physics: Condensed Matter **16**, 5003 (2004) doi:10.1088/0953-8984/16/28/020

[53] T. Wang, D. Zhu, B. Wu, et al.: “Femtosecond Single-Shot Imaging of Nanoscale Ferromagnetic Order in Co/Pd Multilayers Using Resonant X-Ray Holography”, Phys. Rev. Lett. **108**, 2012 (2011) doi:10.1103/PhysRevLett.108.267403

[54] W. Wurth, Z. Hussain: *Report of Working Group I: Photon-in/Photon-out & Electron-out Spectroscopic Experiments*, 2009, http://www.xfel.eu/s

ites/site_xfel-gmbh/content/e63594/e63599/e81232/e65122/e76472/scs-wg-i-report_eng.pdf

[55] L. Young, E. P. Kanter, B. Krässig, et al.: “Femtosecond electronic response of atoms to ultra-intense X-rays”, Nature **56**, 466 (2010) doi:10.1038/nature09177

[56] D. Zhu, M. Guizar-Sicairos, B. Wu, et al.: “High-Resolution X-Ray Lensless Imaging by Differential Holographic Encoding”, Physical Review Letters **105** (2010) doi:10.1103/PhysRevLett.105.043901